Zentime

PROGRESS IN MEDICAL DEVICES

Editor-in-Chief: Haipo Cui

Volume 1, Number 3; Dec. 31, 2023

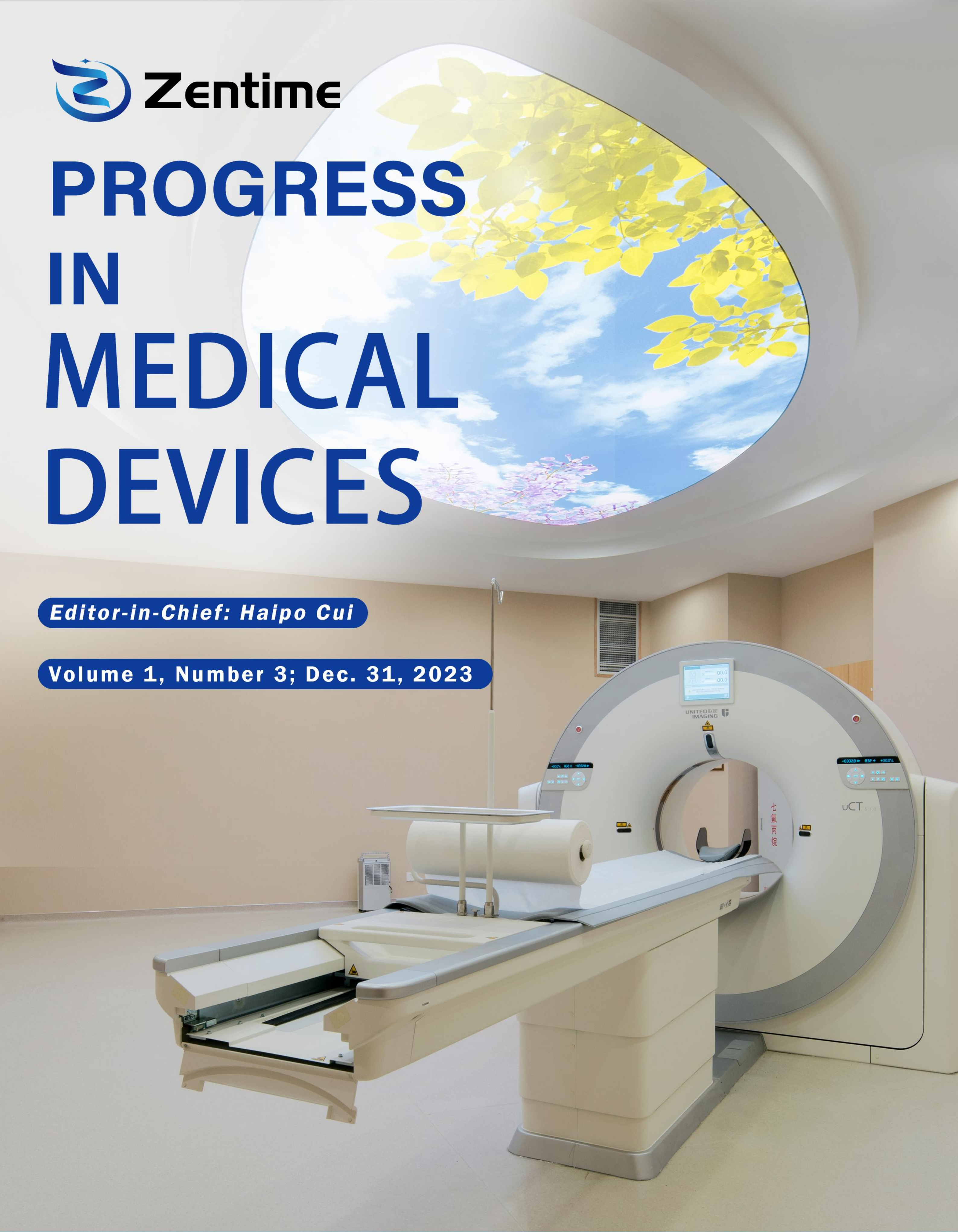

ISSN: 2957-5478

Published by ZENTIME PUBLISHING CORPORATION

Progress in Medical Devices
eISSN: 2957-5478

Review Article https://doi.org/10.61189/323428onxlas

A review of medical image-based diagnosis of COVID-19

Jie Yu, Shiju Yan, Chengli Song, Haipo Cui

School of Health Science and Engineering, University of Shanghai for Science and Technology, Shanghai 200093, China.

Corresponding author: Shiju Yan.

Declaration of conflict of interest: None.

Received March 11, 2023; Accepted November 17, 2023; Published December 31, 2023

Highlights

- Current research on COVID-19 utilizing medical images is categorized into image preprocessing, segmentation, and classification.
- This study provides an in-depth analysis of these categories, as well as provides an outlook on the application and possible future development directions of medical image processing in COVID-19 management.
- Our paper also presents a review of various publicly accessible datasets of COVID-19.

Abstract

The pandemic virus COVID-19 has caused hundreds of millions of infections and deaths, resulting in enormous social and economic losses worldwide. As the virus strains continue to evolve, their ability to spread increases. The detection by reverse transcription polymerase chain reaction is time-consuming and less sensitive. As a result, X-ray images and computed tomography images started to be used in the diagnosis of COVID-19. Since the global outbreak, medical image processing researchers have proposed several automated diagnostic models in the hope of helping radiologists and improving diagnostic accuracy. This paper provides a systematic review of these diagnostic models from three aspects: image preprocessing, image segmentation, and classification, including the common problems and feasible solutions that encountered in each category. Furthermore, commonly used public COVID-19 datasets are reviewed. Finally, future research directions for medical image processing in managing COVID-19 are proposed.

Keywords: Medical image processing, medical image segmentation, diagnosis, preprocessing, COVID-19 dataset

Introduction

COVID-19 is highly contagious and had been a serious threat to human health [1]. Early clinical manifestations are fever and malaise, sometimes with dry cough and dyspnea. However, with the continuous mutation of virus strains, the virulence of the virus decreases, and widespread vaccination leads to the formation of an immune barrier, contributing to an increased proportion of asymptomatic infections. Early recognition of asymptomatic infections is difficult because of their highly insidious nature [2]. To date, a positive result from RT-PCR test remains the primary criterion for diagnosing COVID-19. However, it is worth noting that this method has a high rate of false positives. So, some researchers have started studying the use of medical imaging for diagnosis [3]. It is difficult for inexperienced medical staff to identify potentially infected patients in a timely manner during the outbreak of COVID-19. Therefore, the diagnosis of COVID-19 requires the aid of medical imaging. Among them, CT and X-ray images are the two most common used modalities. Medical image processing has played an active role in combating COVID-19 [4].

This paper aims to extensively discuss the application of medical imaging in the diagnosis of COVID-19 to facilitate future studies. In this review, we present a summary of three key categories involved in the medical image processing-based identification of COVID-19: preprocessing, segmentation, and classification. Then, we provide an overview of several publicly available datasets. Lastly, we propose several directions for future research. This review is

Address correspondence to: Shiju Yan, School of Health Science and Engineering, University of Shanghai for Science and Technology, No.516 Jungong Road, Yangpu District, Shanghai 200093, China. Tel: 18217617984. E-mail: yanshiju@usst.edu.cn.

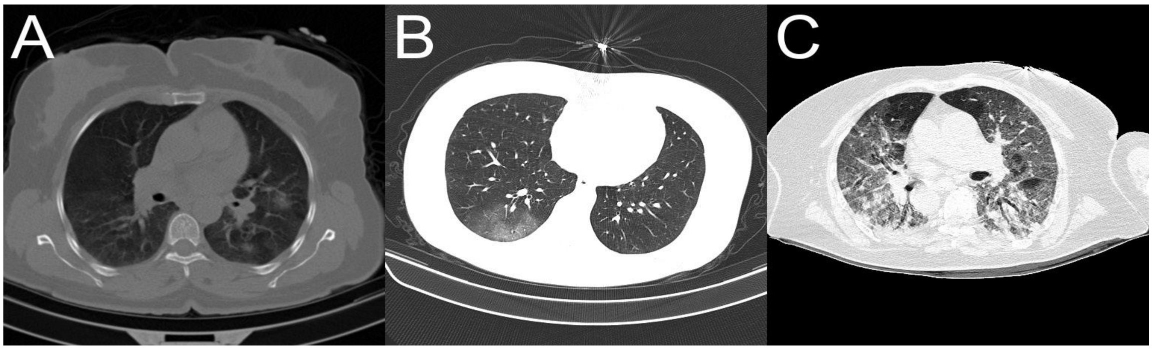

Figure 1. Significant variation among CT images produced by different scanners. (A) Somatom scope; (B) GE Optima CT540; (C) GE Revolution CT. All images were sourced from Shanghai Chest Hospital and have obtained informed consent from the participants.

anticipated to offer valuable insights and guidance for both researchers and radiologists.

Methods

This study examined six databases and other relevant websites, such as National Knowledge Infrastructure, PubMed, IEEE Xplore Library, Science Direct, SpringerLink, and Google Scholar. Diagnostic studies of COVID-19 based on medical images (CT and X-ray images) conducted between 2020 and 2022 were primarily considered. Repetitive studies were excluded, and only representative ones were retained. The search terms encompassed various keywords, including but not limited to "machine learning," "deep learning," "COVID-19," and "SARS-CoV-2." Ultimately, 78 eligible studies were included, covering topics such as segmentation, preprocessing, diagnosis, and datasets of COVID-19.

Preprocessing

Image preprocessing generally encompasses data enhancement and generation. This step serves to reduce image noise, improve the model's generalization performance, mitigate model overfitting, and enhance the detectability of useful information, thereby improving the reliability of the results of subsequent tasks such as feature extraction, image segmentation, and classification.

Data Augmentation

Data augmentation is a widely used technique to address imbalances in dataset distribution and mitigate overfitting of the model, and the its common methods include flipping, rotating, cropping, filling, scaling, panning, as well as contrast and brightness adjustment, which have yield favorable outcomes [5, 6]. In a comparative study conducted by Nishio et al. and aimed at differentiating X-ray images of COVID-19 patients, patients with common pneumonia, and healthy individuals, the accuracy of the model was improved by 4% through using conventional data augmentation techniques [7]. However, the benefits of these data augmentation techniques are limited. Also, different scanners can cause large image variations. As shown in **Figure 1**, images from different CT scanners vary greatly. So, researchers need to design more suitable data augmentation methods according to their datasets. In addition to the problems of image noise and unbalanced distribution, the quality of images produced by different imaging devices often varies widely. Therefore, pre-processing is necessary when multiple datasets are used. In image processing, histogram equalization is often used to increase the local contrast, but it tents to introduces new noise to the image while reducing useful information [8, 9]. This phenomenon arises when specific grayscale levels, which contain valuable information, undergo compression or stretching, resulting in the loss of details or an excessive emphasis on details. Some researchers use a Perona-Malik filter to eliminate the noise introduced by histogram equalization, while more researchers use the method of contrast limited adaptive histogram equalization (CLAHE) [8, 10]. Adaptive histogram equalization (AHE) can amplify the local contrast of an image to obtain more details; however, it also amplifies the noise. CLAHE, on the other hand, reduces the noise by limiting the amplified contrast. Researchers put the images pre-processed by CLAHE into the classification model of COVID-19 images and obtained an excellent accuracy of 94.56%, which significantly improved the classification performance of the network [10]. Lung images processed with the modified clip limit-based contrast limited adaptive histograms equalization (MC-CLAHE) and singular value decomposition-contrast limited adaptive histogram equalization (SVD-CLAHE) approaches both obtained good classification accuracies [11, 12].

Data Generation

It is difficult to obtain a large number of CT images or X-ray image datasets of COVID-19 in a short time due to the specificity of medical datasets and the large amount of manpower required. However, machine learning, especially deep learning, is primarily dependent on a large number of images. Therefore, many researchers used weakly supervised learning methods for COVID-19 detection and diagnosis tasks [13, 14]. Weakly supervised learning is intermediate between supervised and unsupervised learning, and it can obtain favorable results based on a small amount of data.

Generative Adversarial Network

Generative adversarial network (GAN) was used for image denoising and produced high-quality images [15]. The gradient loss function was introduced into unsupervised learning-based non-rigid 3D medical image alignment and exerted favorable results in processing data with noise and blur [16]. The weakly supervised learning method can not only remove noise from the original image to obtain a high-quality image, but also generate new images to expand the dataset. Loey et al. used GAN to expand the original dataset by a factor of 30 and obtained favorable results in diagnosing COVID-19 based on X-ray images [17]. However, the expansion was based on the original small dataset, and the model's generalization performance was not tested. Therefore, the quality of the generated images could not be guaranteed. In a study conducted by Albahli et al., the synthetic chest X-ray images were checked by five radiologists and then mixed with the original images for the diagnosis of COVID-19, and the classification accuracy based on the deep learning network Resnet achieved 89% [18]. However, the original images were all from the frontal angle, and the accuracy may be higher if X-ray images from other angles could be combined. In addition to generating images from the same image pattern, weakly supervised learning enables image style migration and cross-modal data enhancement. Some researchers used GAN to transform contrast-enhanced CT images into non-enhanced CT images and compared the segmentation performance of U-Net trained on the original dataset with that of U-Net trained on the combined dataset of original data and generated images, with the latter accuracy being 4% higher than the former [19]. In the study of Zhang et al., they used 3D Cycle-GAN with a shape consistency loss function to combine two modality datasets with labels and achieved mutual image transformation and data enhancement between cardiac magnetic resonance images (MRI) and cardiac CT images [20]. Still, it requires labels in both datasets, which limits the application scenarios of this approach. Some researchers proposed an end-to-end synthetic segmentation network for training segmentation networks across modalities. With SynSeg-Net, they transformed the labels in MR and CT into each other and achieved better results in segmenting brain CT images and abdominal enlarged spleen [21].

Domain Adaptation

Besides GAN, transfer learning based on domain adaptation is also a kind of weakly supervised learning method for solving the problem of lack of labels. Applying an algorithm or model trained in one or more domains to other domains is called domain adaptation, and the source and target domains need to have the same feature space. Some researchers solved the problem of unlabeled datasets by domain adaptation in COVID-19 diagnosis and obtained favorable outcomes [22, 23]. Jin et al. proposed a self-correcting learning scheme with domain adaptation driven by prior knowledge and dual-domain enhancement and applied it for self-correcting segmentation of infected regions in lung CT images [24]. The model, so called DASC-Net, adaptively aggregates the learned model and the corresponding generated pseudo-labels so that the features of the source and target domains are aligned. This method reduces the generated noise caused by the pseudo-labels. Later, the proposed model was applied on three publicly available COVID-19 CT datasets to test its generalization performance, and the results showed that DASC-Net obtained more advanced segmentation accuracy than others. Sun et al. proposed a novel orthogonal decomposition adversarial domain adaptation (ODADA) architecture for replacing the traditional adversarial domain adaptation module, tested it on three publicly available datasets, and received favorable outcomes [25].

Brief Summary

In this section, the importance of pre-processing is first described, and some common methods are enumerated. Subsequently, a number of countermeasures are presented, along with the corresponding limitations in data augmentation and data generation encountered during medical image processing when dealing with difficult-to-collect datasets and variations in dataset quality during the COVID-19 epidemic. Almost every medical image processing requires preprocessing to achieve higher accuracy. Therefore, we hope that this section can assist relevant researchers in choosing the appropriate preprocessing method according to their datasets, so as to accomplish subsequent tasks more effectively.

Segmentation

Medical image segmentation is to identify regions of interest from medical images (including MRI, CT images, ultrasound images, etc.) and segment them from the background, which is an essential yet challenging step in image processing and analysis for evaluating and quantifying COVID-19 [26-28]. According to the tools used, medical image segmentation can be further divided into traditional and semantic segmentation based on deep learning. In traditional methods, researchers manually extract low-level semantic features such as color values, grayscale values, and geometry of the image and then segment the image into multiple regions without intersection with similar features shared in the same region. Finally, the segmented image is obtained by annotating these regions. The commonly used traditional methods are segmentation algorithms based on thresholding, region, edge detection, configuration, clustering, deformable model, and graph theory. Segmentation based on deep learning extracts the medium- and high-level semantic features from the images. Due to the excellent feature extraction and representation capabilities in image segmentation, as well as the avoidance of manual feature extraction, convolutional neural networks (CNN) have been used to segment medical images in recent years. CNN has made great contributions, especially in segmenting COVID-19 images [28]. But few researchers have conducted research in this direction because there are few COVID-19 X-ray datasets with mask images [29]. The primary focus of this section is to provide a comprehensive summary of the application of deep learning in medical image segmentation, specifically on CT images of COVID-19. Within the existing literature, two distinct segmentation tasks have been identified for the segmentation of COVID-19 images: lung field segmentation and lung-lesion segmentation.

Lung Field Segmentation

Lung field segmentation is to segment the lung from the image as a preprocessing step for subsequent tasks such as classifying and fine segmenting the infected region. Several studies have demonstrated that lung field segmentation helps to improve diagnostic accuracy and reduce the difficulty of the subsequent tasks [10, 29, 30]. In the study of Aswathy et al., cascaded U-Net was employed for segmentation of COVID-19 images [31]. They first removed the part of the background that resembled the lung by preprocessing. After this, they used two 3D U-Net, of which the first network separated the lung from the background, and the second network segmented the lung lesion region, and finally obtained a favorable dice score of 82%. Wang et al. constructed a segmentation-classification dual task model in which the entire parenchymal lung region was firstly segmented, and the lung lesion region was segmented afterward [32]. They tested several combined models of segmentation and classification networks and validated them on multiple datasets by five experts. The result showed that the "3D Unet++-ResNet-50" combined model achieved the best AUC of 0.991, and the system was deployed in at least sixteen hospitals.

Lung-Lesion Segmentation

Lesion region segmentation is to segment regions of interest from lung images, such as regions indicating consolidation, ground glass opacity (GGO), pulmonary fibrosis, interstitial thickening, and pleural effusion. However, lesion regions in CT images of COVID-19 patients at early stage are small and have their own shapes and textures, which are challenging for lesion segmentation. Most segmentation models are variations of U-Net and V-Net. We present a typical segmentation-based COVID-19 diagnosis model in **Figure 2** [33]. U-Net is a fully convolutional network with U-shaped symmetric encoding and decoding paths, and the same layers in both paths are connected to learn contextual features better. Several studies demonstrated the applicability of U-Net to the segmentation of medical images [33, 34]. V-Net is a variant of U-Net applied to 3D data. Zhang et al. proposed a new segmentation method that combined residual and dense blocks and used them in U-Net to form a new concatenation, namely QC-HC U-Net [34]. They tested it on two publicly available datasets and got dice scores of 82% and 81%, respectively. Chen et al. used aggregated residual transformations to learn features with robustness and expressiveness [35]. They applied attention mechanisms to improve the model's ability to distinguish various symptoms of COVID-19, achieving a dice score as high as 94% [35]. Despite the favorable outcomes achieved by countless researchers

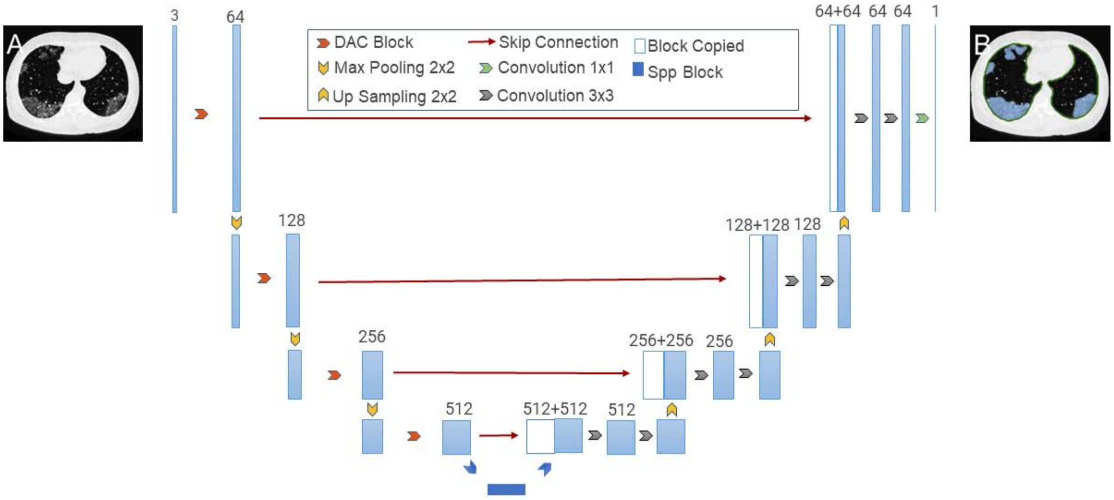

Figure 2. A typical UNet-segmentation-based pixel-level model. (A) original image obtained using the Revolution CT scanner; (B) segmented image obtained using the Revolution CT scanner. This image is from Shanghai Chest Hospital and has obtained informed consent from the participant.

in segmenting medical images using U-Net and its variants, one of the remaining problems of deep learning is the lack of interpretability. Hence, Wu et al. developed a joint classification and segmentation for COVID-19 diagnosis [36]. To increase the interpretability of the model, they introduced class activation mapping (CAM), a tool for visualizing convolutional neural networks (CNNs). Using CAM, they could clearly observe the areas that the model focused on and then make targeted adjustments. Besides, Wu et al. systematically constructed a large COVID-19 classification and segmentation dataset named COVID-CS and tested their proposed system in this dataset segmentation [36]. The dice score of their segmentation task was 78.5%. The lack of labels of datasets is one of the most common problems in medical image segmentation, so some researchers suggested using weakly supervised methods to generate segmentation mask images. In a study conducted by Fan et al., they proposed a COVID-19 lung lesion segmentation network called Inf-Net, which utilized a reverse attention module and an edge attention module to improve the identification of infected regions [37]. In addition, to address the lack of labeling of datasets, they also proposed a semi-supervised segmentation network named Semi-Inf-Net. Wang et al. introduced the self-attentive mechanism and spatial convolution module into the segmentation model (SSA-Net) to automatically identify infected regions from chest CT images [38]. The self-attentive mechanism could extract useful contextual information from deeper levels to enhance feature learning without additional training time. Spatial convolution is a method that processes only the adjacent image elements around each pixel, which can be used to strengthen the network and accelerate the training convergence.

Brief Summary

This subsection provides an overview of medical image segmentation, including its meaning and classification. Additionally, common challenges associated with segmenting COVID-19 images are outlined, and a range of potential solutions are presented. The goal of this subsection is to assist researchers in selecting the most suitable network architecture for their specific segmentation problems and to help them anticipate possible challenges while providing corresponding solutions.

Classification

Rapid identification and appropriate treatment of patients with suspected COVID-19 in the epicenter of outbreak is of great importance. Due to the fast imaging, X-ray and CT scans are widely used to diagnose COVID-19 [39]. However, the large number of medical images adds to the burden of specialists, and COVID-19 shares the same imaging features with common lung diseases such as pneumonia. Inexperienced doctors may need help in distinguishing them. Therefore, it is necessary to use machine learning to assist in classification. In the existing studies, COVID-19 classification based on medical images and artificial intelligence could be broadly classified into three categories: classification based on traditional machine learning, CNN-based classification, and combining of traditional machine learning and CNN.

Classification Based on Traditional Machine

Learning

The common algorithms for the classification task of the COVID-19 dataset mainly include Naive Bayes (NB), support vector machine (SVM), decision tree (DT), random forest (RF), adaptive boosting (AdaBoost), K-nearest neighbor (KNN), gradient boosting decision tree (GBDT), logistic regression (LR), artificial neural network (ANN), extremely trees (ET), light gradient boosting machine, multilayer perceptron (MLP), etc. In a study by Absar et al., the texture, color, and shape features were extracted from 7,180 X-ray images after preprocessing [39]. Then, these images were classified by an SVM classifier with five-fold cross validation, which obtained an accuracy of 98.83%. Wu et al. used a combination of gray level co-occurrence matrix (GLCM) and nonsubsampled dual-tree complex contourlet transform (NSDTCT) to extract texture features of images, and used an RF classifier to predict the result [40]. At last, they achieved an AUC of 0.957 in distinguishing COVID-19 from other pneumonia. Some researchers used a single model, while others selected the optimal model from multiple models or used a combination of models to construct their classification models. Tamal et al. manually segmented lung parenchyma in X-ray images, after which the radiomic features of each lung were extracted separately using a tool called Pyradiomics, and achieved an AUC of 0.9226 in classification task with multiple machine learning algorithms [41]. Shahin et al. developed a computer-aided diagnosis (CAD) program [42]. After being segmented by k-mean clustering, the images were predicted by SVM and radial basis functions (RBF). This program performed well in predicting whether a patient was infected with COVID-19 and staging the patient's condition, and it could be used to reduce the workload of clinicians.

CNN-based classification

The performance of the traditional machine learning approaches is limited, while CNNs can perform better. Diagnosing COVID-19 by transfer learning is one of the most common approaches. It is more challenging to obtain COVID-19 medical image datasets compared to common pneumonia and normal subjects, so if the data used to train the CNN model are unbalanced, especially when there are fewer COVID-19 images compared to other classes, although good results can be obtained in the overall classification task, the performance would be poor in detecting COVID-19 alone. Such classification networks do not have reliability. Data augmentation is the most common solution to the imbalance in data distribution. Saha et al. applied a deep convolutional neural network called decomposition, transfer, and combination (DeTraC) to detect COVID-19 in X-ray images [43]. To improve the efficiency of the model, principal component analysis (PCA) was applied to project the high-dimensional features extracted through the CNN to lower dimensions for feature dimensionality reduction. Finally, their method was tested on two datasets, and obtained an accuracy of 93.1%. The number of common pneumonia images they used was significantly less than that of COVID-19. Although the data augmentation was used to slightly moderate the error caused by an imbalance in the number, they did not take into account the error caused by different image sources. A transfer learning method based on domain adaptation solved this problem well. Zhang et al. used a domain adaptation method called COVID-DA to accurately identify COVID-19 with a small number of labels [30]. Using a single CNN model to detect COVID-19 without model improvement might make it difficult to achieve high-accuracy classification on X-ray images or CT images [44]. Some researchers started to explore the use of multiple deep learning models and combine them in a task, and this learning method is called integrated learning. Rahimzadeh et al. used features extracted through two CNN models (ResNet50V2 and Xception) in tandem for a triple classification task on X-ray images based on two publicly available datasets, and the average accuracy reached 91.4% [45]. Hall et al. applied ResNet50, VGG16, and their own small CNN to the classification task of COVID-19 and selected problematic CT images using a voting system, with a final accuracy of 91.24% [46]. The integrated model using multiple algorithms could improve the accuracy of diagnosis to some extent compared to each individual algorithm, but the integrated model is computationally expensive because it must train millions of parameters, which makes it challenging for researchers to tune the hyperparameters.

Classification Based on a Combination of Traditional Machine Learning and CNN

Some features extracted by CNN may negatively affect the classification task, and we can remove these irrelevant features by combining traditional machine learning algorithms to obtain higher classification accuracy. Many researchers combined traditional machine learning and CNN and obtained favorable outcomes [47]. Sahlol et al. proposed an improved COVID-19 image hybrid classification method using CNN to extract features. They used the

Table 1. Summary of COVID-19 image datasets

Dataset	Modality	Covid-19	Total	Format	Segmentation	Diagnosis
COVID-QU-Ex	X-ray	11,965	33,920	2D	√	√
COVIDGR Dataset	X-ray	426	852	2D		√
COVIDx Dataset	X-ray	16,490	30,882	2D		√
Covid-Chestxray-Dataset	X-ray+CT	563	930	2D		√
BIMCV COVID-19+	X-ray+CT	--	23,527	3D	√	
COVID-19 CT Lung and Infection Segmentation Dataset.	CT	20	20	3D	√	
SARS-CoV-2 CT	CT	1,252	2,482	2D		√
COVID-19 CT Segmentation Dataset	CT	110	110	3D	√	
MOSMEDDATA	CT	--	1,110	3D	√	
COVID-CT Dataset	CT	15,589	63,849	2D		√
CT Scans for COVID-19 Classification	CT	4,001	39,370	2D		√
COVIDx CT	CT	--	431,205	2D	√	√
Large COVID-19 CT Scan Slice Dataset	CT	7,593	17,104	2D	√	√

marine predator algorithm (MPA) to select the most relevant features [48]. Finally, fractional-order calculus (FOC) was used to enhance features. Then, they applied this method to several datasets, and the classification accuracies were all above 98%. Their approach achieved high performance in classification while reducing the computational complexity. Kassania et al. used an advanced CNN model to extract features from X-ray images and trained machine learning algorithms to classify COVID-19 [49]. They used 10-fold cross-validation to evaluate the average generalization performance of the classifier in each trial. Finally, the combination of DenseNet-121 and Bagging Tree achieved an optimal accuracy of 99.00%, which is also the highest accuracy on this dataset. However, their dataset is small, and further validation on a larger dataset is needed. In the study of Jin et al., the pre-trained AlexNet model was used for deep feature extraction and filtered features [50]. Finally, SVM classifiers with various kernel functions (linear, quadratic, cubic, and Gaussian) were used for COVID-19 classification, achieving an accuracy of 98.64%, which was higher than that of the pre-trained CNN classification alone.

Brief Summary

This section provides a detailed introduction to the role of medical image-based classification methods in COVID-19 from three aspects: classification based on traditional machine learning, CNN-based classification, and combining traditional machine learning with CNN. Traditional machine learning technology is comparatively mature but exhibits limited performance, whereas CNNs often yield favorable results but require additional resources. The combination of traditional machine learning and CNN can achieve high classification accuracy.

Dataset

Having sufficient high-quality training datasets is vital for designing, implementing, and evaluating COVID-19 medical image-based diagnostic models. In this section, the focus is on introducing the datasets available for COVID-19 images. **Table 1** provides a summary of 13 datasets used for classification and segmentation purposes. The table includes information such as the imaging modality, the number of COVID-19 samples, the total number of samples, the dimensionality of the data, and suitability for segmentation or classification tasks.

• COVID-QU-Ex dataset [51-55]. This dataset was created by multinational researchers including Qatar University in Doha, Qatar. It contains chest X-ray image data of positive COVID-19 cases as well as normal and viral pneumonia images. The dataset consists of 33,920 chest X-ray images and corresponding masked images, including: 11,956 COVID-19 images, 11,263 viral or bacterial pneumonia images, and 10,701 normal chest images.

• COVID-19 CT lung and infection segmentation dataset [56]. This dataset contains 20 labeled COVID-19 CT scan images. The left lung, right lung and infected areas are segmented by two radiologists and validated by experienced radiologists.

• SARS-CoV-2 CT dataset [57]. The data were collected from patients at the São Paulo Hospital in Brazil, containing 1,252 COVID-19 CT images and 1,230 CT images of healthy subjects.

• Covid-Chest x-ray dataset [58]. The dataset contains 930 images, including 45 lung CT images (including 42 positive images) and 885 x-ray images. The limited sample images dictates that it needs to be used in conjunction with other datasets.

• COVID-19 CT segmentation dataset [59]. The dataset contains 110 CT scan images, 100 of which are annotated by radiologists and labeled with three types, including GGO, consolidation, and pleural effusion. In addition, it contains more than 700 lung parenchymal mask images that can be used to train the whole lung segmentation network.

• MOSMEDDATA [58]. The dataset was provided by the Municipal Hospital in Moscow, Russia, with a total of 1,110 CT scan images, 50 of which have masked images, and the GGO and lung nodules were annotated by doctors.

• COVIDGR dataset [60]. This dataset was collected by the Granada Hospital and contains a total of 852 X-ray images. It is noteworthy that it is a well-balanced dataset, containing X-ray images of both COVID-19 positive and healthy individuals, and covering a wide range of illnesses and various stages of each one.

• BIMCV COVID-19+ [61]. Data were collected from some public datasets, including COVID-CT-Dataset, COVID-19 dataset, COVID-19 radiography database, and some private datasets. It includes a total of 23,527 X-ray and CT images, 23 of which are GGO and solid lung lesions that annotated by radiologists. It is noteworthy that the size of this dataset is 389.27 GB, which can satisfy most of the deep learning dataset requirements.

• COVID-CTset [62]. It was collected from a radiology department located in Sari, Iran, from March 5 to April 23, 2020. The dataset contains complete raw CT scans of 377 individuals, including 15,589 CT images from 95 COVID-19 patients and 48,260 images from 282 healthy individuals.

• CT Scans for COVID-19 Classification [63]. The data were collected from Union Hospital (HUST-UH) and Liyuan Hospital (HUST-LH), containing a total of 39,370 CT images. The researchers manually labeled a subset of 4,001 images with imaging features associated with COVID-19, 9,979 images of both lungs with imaging features unrelated to COVID-19 and excluded 5,705 images that do not contain any lung information. Notably, this dataset also contains some clinical features of the patients that can be used in other studies.

• COVIDx dataset [64]. This is a combined dataset of COVID-19 X-ray images from COVID-19 Image Data Collection, COVID-19 Chest X-ray Dataset Initiative, ActualMed COVID-19 Chest X-ray Dataset Initiative, RSNA Pneumonia Detection Challenge dataset, and COVID-19 radiography database. A total of 30,000 images are included, including 16,490 positive cases.

• COVIDx CT [65]. This is a combined dataset of COVID-19 CT images collected from a number of publicly available datasets, including COVID-19 CT Lung and Infection Segmentation Dataset, MosMed Data [58], COVID-CT Set and so on. A total of 431,205 CT images from 6,068 patients are included.

• Large COVID-19 CT Scan Slice Dataset [66]. This dataset is collected from seven public datasets, including a total of 17,104 images, of which 60 CT scan images have masked images.

Prospect

The medical image-based approach has made an important contribution not only to the diagnosis of COVID-19, but also beyond.

Prognosis

Estimating disease progression or outcome over time based on patients' pre-treatment medical images and guiding decision-making of physicians in further treatment is another area of research in medical imaging. The so-called medical state or outcome can be a specific medical event, such as death complications, or a quantitative measure, such as disease progression, pain and quality of life. In prognostic studies based on medical images, the most common are overall survival (OS) analysis of patients and prediction of disease progression. These prognostic models can provide information for physicians to develop patients' treatment plans. Huang et al. extracted the radiomics features of CT images to predict disease-free survival in patients with the initial stage of non-small cell lung cancer [67]. Ultimately, they found that first-order statistical features were significantly associated with tumor heterogeneity and 3-year disease-free survival, and their method outperformed conventional staging systems and clinicopathologic nomograms. The most common prognostic determination based on medical image of brain is the study of Alzheimer's disease (AD). AD is a progressive neurodegenerative disorder, and interventions in the early stages, known as mild cognitive impairment (MCI) and preclinical stages can obtain more favorable outcome. Accurate prediction of clinical changes in MCI patients, including qualitative changes (when to convert to AD) and quantitative changes at future time points, is therefore important for early diagnosis of AD and monitoring disease progression. Zhang et al. used multiple imaging modalities at multiple time points to predict the conversion of MCI [68]. They applied an MKL classifier consisting of time-varying longitudinal imaging features and patient cognitive test scores at each time point in 88 MCI subjects, 35 of whom converted to AD within one year. After using 10-fold cross-validation, their method achieved an accuracy of 78.4%, outperforming those methods using only single modality images. In addition to AD, some researchers directed their attention to spontaneous intracerebral hemorrhage (SICH). Zhou et al. collected radiomic features from CT images and some clinical information of 326 patients with SICH and developed radiomic-clinical (R-C) nomogram drawings for the short-term prognosis of patients, and finally selected nine features for prognosis prediction [69]. Their method obtained an AUC of 0.80 on the test sets, which helped clinicians assess the risk of patients. In addition to lung and brain, the approach based on medical images performed well in the prognosis prediction of disease in other sites, such as breast, prostate, and liver. Keyl et al. developed a survival prediction model for advanced pancreatic cancer based on machine learning and multimodal data [70]. They extracted clinical data and radiomic features from 203 patients with advanced pancreatic cancer and performed feature selection, resulting in a C-index of 0.71.

Since the outbreak of COVID-19, there has been a shortage of medical resources in many places of the world. If emergency resources are deployed properly, the epidemic can be effectively controlled; otherwise, it will inevitably cause great losses. Therefore, during an epidemic, it is particularly important to manage patients in a hierarchical manner and to plan the use of medical resources such as the ICU. Zhang et al. proposed an AL-based radiomic nomogram, and they used CT images and clinical information to prognosticate the subsequent condition of COVID-19 patients [71]. They finally selected 21 radiological features and two clinical features that were significantly associated with COVID-19 prognosis, and validated these features on an external dataset with favorable outcome (an AUC of 0.84). In addition to CT images, several studies have shown the statistical relevance of chest X-ray images for predicting the subsequent progression of COVID-19 for the hierarchical management of patients. Younus et al. proposed a novel high-resolution CT (HRCT) scoring system for predicting the progression of COVID-19 patients [72]. They divided the two lungs in CT images into 20 regions, scored each region, and graded COVID-19 patients according to the scores and clinical parameters for the hierarchical management. Their method, to some extent, reduced the burden on medical institutions during an epidemic. However, due to the scarcity of relevant datasets and patient privacy, prognostic studies based on medical images of COVID-19 patients are rare. Most of the studies do not have generalization performance and are all short-term research. Studies have shown that some COVID-19 patients develop a variety of medium- and long-term sequelae after initial recovery from COVID-19, which may affect the respiratory, cardiovascular, neurological, musculoskeletal, dermatologic, and renal systems [73]. For this reason, the World Health Organization has emphasized the importance of the medium- and long-term prognosis management for patients with COVID-19. A prognostic approach based on medical images may help physicians predict patients who are prone to develop COVID-19 sequelae early, so as to make treatment plans in advance.

Efficacy Assessment

Clinical efficacy assessment aims to examine the safety and efficacy of a drug or a treatment method in patients. Evaluation of effectiveness by comparing the differences in images before and after treatment is a typical approach. The WHO criteria and the Response Evaluation Criteria in Solid Tumors (RECIST) are the golden criteria for assessing the effectiveness of radiation therapy in eliminating tumors, and tumor size is one of the most important factors in these two criteria. Mena et al. used PET-CT to monitor the condition of NSCLC patients treated with radiation therapy [74]. They evaluated the efficacy according to the size of the tumor before and after treatment and made targeted adjustments to the subsequent treatment plan. The results showed that PET-CT images could be evaluated systemically, and they played an important role in all stages of treatment (diagnosis, initial staging, treatment response assessment, and recurrence monitoring) in patients with NSCLC. Hadi et al. predicted the outcomes of breast cancer patients after neoadjuvant chemotherapy (NCA) with breast ultrasound images and the KNN classifier [75]. They extracted textural features from ultrasound images of 100 patients before, one week after, and four weeks after treatment, and combined clinical, pathological, and 5-year relapse-free survival (RFS) information to develop an efficacy assessment model for evaluating the outcome of patients after receiving NCA. Ultimately, their model obtained an accuracy of 96%. Medical image-based efficacy assessment can help healthcare professionals evaluate the effects of therapeutic modalities such as radiation therapy, targeted therapy, and immunotherapy, as well as certain drugs. Mejia et al. evaluated the efficacy of drugs on patients with heart muscle disease by echocardiographic monitoring [76]. A comparison of parameters such as ventricular geometry, left ventricular end-diastolic dimension, and ventricular function in patients with dilated cardiomyopathy at pre-treatment, six months post-treatment, and 18 months post-treatment revealed that cardiac reverse remodeling drugs were highly effective in treating dilated cardiomyopathy, while Beta-blocking drugs reduced the patient's heart rate and increased diastolic filling time for cardiac hypertrophy, decreasing left ventricular outflow tract flow.

According to relevant studies, the mortality of COVID-19 patients in severe or critical conditions could be as high as 49%, and respiratory support and dexamethasone use remain the mainstay of treatments [77]. Therefore, scientists are investigating the development of other drugs and treatment modalities to reduce the rate of severe illness and mortality in patients with COVID-19. In the process of developing new drugs or treatment modalities, it is particularly important to select appropriate efficacy assessment metrics. To evaluate the effectiveness of antiviral therapy in patients with COVID-19, Liao et al. designed a simulation trial to assess the efficacy of Remdesivir in patients with COVID-19, and the results demonstrated that Remdesivir helped to reduce mortality and improve the chances of recovery [78]. However, their trial included only statistical data, such as the length of hospitalization and mortality of patients, but ignored clinical and physiological data during treatment. Tobback et al. designed a randomized controlled trial to assess Camostat's efficacy in COVID-19 patients in severe or critical conditions [79]. They divided 90 patients into two groups. The experimental group was treated by using Camostat, and the control group was injected with a placebo. They used clinical parameters, clinical-improvement time, and nasopharyngeal viral load as indicators for evaluation. Although the final result showed that Camostat was not found to be effective in the treatment of COVID-19 patients, their method still made sense. For the therapeutic drugs or treatment modalities of COVID-19, most of the existing efficacy assessment trials used outcome, clinical, and pathological data as evaluation indicators. However, some studies showed that medical images could also be used for efficacy assessment. In order to evaluate the therapeutic effect of Chinese medicine on patients with COVID-19, Wang et al. selected 55 critically ill patients as experimental subjects [80]. They compared the differences in CT images of patients before and after treatment and established a scoring system for the patients' CT images, which was based on the percentage of lesion area and the type of imaging signs. Higher score indicates more severe disease. Patients' images showed a significant reduction in lung consolidation after Chinese medicine treatment, indicating that Chinese medicine has an important role in promoting lung lesion absorption. It's challenging to collect sufficient high-quality medical image datasets, so many medical image researchers could only obtain data from retrospective trials. However, for efficacy assessment, we have to use different images in each trial due to individual differences, lack of normative indicators, and differences in treatment modalities and drugs, which poses an even greater challenge for research.

Brief Summary

In this subsection, we focus on discussing the potential application prospects of medical images technology regarding both prognosis and efficacy assessment of COVID-19. Additionally, some challenges encountered in existing studies are outlined. However, with the continuous expand of datasets and constant improvement in related standards, medical image-based prognosis, and efficacy assessment will play an increasingly significant role. These methods will aid in predicting subsequent disease progression of COVID-19 patients, assisting medical staff in efficiently allocating medical resources, and evaluating the effectiveness of new drugs.

Conclusion

In this review, recent research on COVID-19 diagnosis based on medical images is summarized in terms of three categories: image preprocessing, image segmentation, and classification. Firstly, the meaning and classification of the three tasks are described, followed by an enumeration of common issues in diagnosing COVID-19 and a presentation of potential solutions. Subsequently, various public datasets for COVID-19 classification and segmentation are introduced. Finally, future research directions for utilizing medical images in combating COVID-19 are proposed.

High-quality medical datasets with sufficient samples are becoming increasingly crucial. In addition to the need for legal and regulatory support, the datasets used by researchers should include different phases and multimodal images, such as ultrasound, X-ray, CT scans, and MRI, whenever possible, due to the fact that such multimodal systems can take full advantage of the important features of each imaging technique, thus improving the reliability of the diagnosis of COVID-19. There are many indications that medical image processing will play an increasingly important role in the future fight against COVID-19.

References

[1] Canale MP, Menghini R, Martelli E, et al. COVID-19–Associated Endothelial Dysfunction and Microvascular Injury: From Pathophysiology to Clinical Manifestations. Cardiac Electrophysiology Clinics 2022;14:21-28.

[2] Huang L, Zhang X, Zhang X, et al. Rapid asymptomatic transmission of COVID-19 during the incubation period demonstrating strong infectivity in a cluster of youngsters aged 16-23 years outside Wuhan and characteristics of young patients with COVID-19: A prospective contact-tracing study. J Infect 2020;80:e1-e13.

[3] Fang Y, Zhang H, Xie J, et al. Sensitivity of Chest CT for COVID-19: Comparison to RT-PCR. Radiology 2020;296:E115-e117.

[4] Aylett-Bullock J, Luccioni AS, Pham KH, et al. Mapping the Landscape of Artificial Intelligence Applications against COVID-19. ArXiv 2020;abs/2003.11336.

[5] Minaee S, Kafieh R, Sonka M, et al. Deep-COVID: Predicting COVID-19 from chest X-ray images using deep transfer learning. Medical Image Analysis 2020;65:101794.

[6] Yamaç M, Ahishali M, Degerli A, et al. Convolutional Sparse Support Estimator-Based COVID-19 Recognition From X-Ray Images. IEEE Trans Neural Netw Learn Syst 2021;32:1810-1820.

[7] Nishio M, Noguchi S, Matsuo H, et al. Automatic classification between COVID-19 pneumonia, non-COVID-19 pneumonia, and the healthy on chest X-ray image: combination of data augmentation methods. Sci Rep 2020;10:17532.

[8] Karim M, Döhmen T, Rebholz-Schuhmann D, et al. DeepCOVIDExplainer: Explainable COVID-19 diagnosis based on chest X-ray images (Preprint). ArXiv 2004.04582 2020.

[9] Syarif A, Azman N, Ronal Repi VV, et al. UNAS-Net: A deep convolutional neural network for predicting Covid-19 severity. Inform Med Unlocked 2022;28:100842.

[10] Liu F, Chen D, Zhou X, et al. Let AI Perform Better Next Time—A Systematic Review of Medical Imaging-Based Automated Diagnosis of COVID-19: 2020–2022. Appl Sci 2022;12.

[11] Roy S, Tyagi M, Bansal V, et al. SVD-CLAHE boosting and balanced loss function for Covid-19 detection from an imbalanced Chest X-ray dataset. Comput Biol Med 2022;106092.

[12] Tiwari L, Raja R, Awasthi V, et al. Detection of lung nodule and cancer using novel Mask-3 FCM and TWEDLNN algorithms. Measurement 2021;172.

[13] Zhu Q, Ye H, Sun L, et al. GACDN: generative adversarial feature completion and diagnosis network for COVID-19. BMC Med Imaging 2021;21:154.

[14] Zhang J, Yu L, Chen D, et al. Dense GAN and multi-layer attention based lesion segmentation method for COVID-19 CT images. Biomed Signal Process Control 2021;69:102901.

[15] Zhang S, Wang L, Chang C, et al. An Image Denoising Method Based on BM4D and GAN in 3D Shearlet Domain. Math Probl Eng 2020;2020:1-11.

[16] Zhang X, Jian W, Chen Y, et al. Deform-GAN: An Unsupervised Learning Model for Deformable Registration. ArXiv 2020;abs/2002.11430.

[17] Loey M, Smarandache F, M. Khalifa NE. Within the Lack of Chest COVID-19 X-ray Dataset: A Novel Detection Model Based on GAN and Deep Transfer Learning. Symmetry 2020;12:651.

[18] Albahli S. Efficient GAN-based Chest Radiographs (CXR) augmentation to diagnose coronavirus disease pneumonia. Int J Med Sci 2020;17:1439-1448.

[19] Sandfort V, Yan K, Pickhardt PJ, et al. Data augmentation using generative adversarial networks (CycleGAN) to improve generalizability in CT segmentation tasks. Sci Rep 2019;9:16884.

[20] Zhang Z, Yang L, Zheng Y. Translating and Segmenting Multimodal Medical Volumes with Cycle- and Shape-Consistency Generative Adversarial Network. 2018 IEEE/CVF Conference on Computer Vision and Pattern Recognition 2018;9242-9251.

[21] Huo Y, Xu Z, Moon H, et al. SynSeg-Net: Synthetic Segmentation Without Target Modality Ground Truth. IEEE Trans Med Imaging 2019;38:1016-1025.

[22] Heidari A, Jafari Navimipour N, Unal M, et al. The COVID-19 epidemic analysis and diagnosis using deep learning: A systematic

literature review and future directions. Comput Biol Med 2022;141:105141.
[23] Li X, Shen L, Lai Z, et al. A self-supervised feature-standardization-block for cross-domain lung disease classification. Methods 2022;202:70-77.
[24] Jin Q, Cui H, Sun C, et al. Domain adaptation based self-correction model for COVID-19 infection segmentation in CT images. Expert Syst Appl 2021;176:114848.
[25] Sun Y, Dai D, Xu S. Rethinking adversarial domain adaptation: Orthogonal decomposition for unsupervised domain adaptation in medical image segmentation. Med Image Anal 2022;82:102623.
[26] Aljabri M, AlGhamdi M. A review on the use of deep learning for medical images segmentation. Neurocomputing 2022;506:311-335.
[27] Hesamian MH, Jia W, He X, et al. Deep Learning Techniques for Medical Image Segmentation: Achievements and Challenges. J Digit Imaging 2019;32:582-596.
[28] Ebrahimkhani S, Jaward MH, Cicuttini FM, et al. A review on segmentation of knee articular cartilage: from conventional methods towards deep learning. Artif Intell Med 2020;106:101851.
[29] Shi F, Wang J, Shi J, et al. Review of Artificial Intelligence Techniques in Imaging Data Acquisition, Segmentation, and Diagnosis for COVID-19. IEEE Rev Biomed Eng 2021;14:4-15.
[30] Zhang Y, Niu S, Qiu Z, et al. COVID-DA: Deep domain adaptation from typical pneumonia to COVID-19 (Preprint). ArXiv 2005.01577 2020.
[31] L AAS VCS. Cascaded 3D UNet architecture for segmenting the COVID-19 infection from lung CT volume. Sci Rep 2022;12:3090.
[32] Wang B, Jin S, Yan Q, et al. AI-assisted CT imaging analysis for COVID-19 screening: Building and deploying a medical AI system. Appl Soft Comput 2021;98:106897.
[33] Ronneberger O, Fischer P, Brox T. U-Net: Convolutional Networks for Biomedical Image Segmentation. Medical Image Computing and Computer-Assisted Intervention – MICCAI 2015 2015;234-241.
[34] Zhang Q, Ren X, Wei B. Segmentation of infected region in CT images of COVID-19 patients based on QC-HC U-net. Sci Rep 2021;11:22854.
[35] Chen X, Yao L, Zhang Y. Residual attention u-net for automated multi-class segmentation of covid-19 chest ct images (Preprint). ArXiv 2004.05645 2020.
[36] Wu YH, Gao SH, Mei J, et al. JCS: An Explainable COVID-19 Diagnosis System by Joint Classification and Segmentation. IEEE Trans Image Process 2021;30:3113-3126.
[37] Fan DP, Zhou T, Ji GP, et al. Inf-Net: Automatic COVID-19 Lung Infection Segmentation From CT Images. IEEE Trans Med Imaging 2020;39:2626-2637.
[38] Wang X, Yuan Y, Guo D, et al. SSA-Net: Spatial self-attention network for COVID-19 pneumonia infection segmentation with semi-supervised few-shot learning. Med Image Anal 2022;79:102459.
[39] Absar N, Mamur B, Mahmud A, et al. Development of a computer-aided tool for detection of COVID-19 pneumonia from CXR images using machine learning algorithm. J Radiat Res Appl Sci 2022;15:32-43.
[40] Wu Z, Li L, Jin R, et al. Texture feature-based machine learning classifier could assist in the diagnosis of COVID-19. Eur J Radiol 2021;137:109602.
[41] Tamal M, Alshammari M, Alabdullah M, et al. An integrated framework with machine learning and radiomics for accurate and rapid early diagnosis of COVID-19 from Chest X-ray. Expert Syst Appl 2021;180:115152.
[42] Shahin OR, Alshammari HH, Taloba AI, et al. Machine Learning Approach for Autonomous Detection and Classification of COVID-19 Virus. Comput Electr Eng 2022;101:108055.
[43] Saha P, Sadi MS, Islam MM. EMCNet: Automated COVID-19 diagnosis from X-ray images using convolutional neural network and ensemble of machine learning classifiers. Inform Med Unlocked 2021;22:100505.
[44] Hariri W, Narin A. Deep neural networks for COVID-19 detection and diagnosis using images and acoustic-based techniques: a recent review. Soft comput 2021;25:15345-15362.
[45] Rahimzadeh M, Attar A. A modified deep convolutional neural network for detecting COVID-19 and pneumonia from chest X-ray images based on the concatenation of Xception and ResNet50V2. Inform Med Unlocked 2020;19:100360.
[46] Hall LO, Paul R, Goldgof DB, et al. Finding covid-19 from chest x-rays using deep learning on a small dataset (Preprint). ArXiv 2004.02060 2020.
[47] da Silva SF, Ribeiro MX, Batista Neto JdES, et al. Improving the ranking quality of medical image retrieval using a genetic feature selection method. Decis Support Sys 2011;51:810-820.
[48] Sahlol AT, Yousri D, Ewees AA, et al. COVID-19 image classification using deep features and fractional-order marine predators algorithm. Sci Rep 2020;10:15364.
[49] Kassania SH, Kassanib PH, Wesolowskic MJ, et al. Automatic Detection of Coronavirus Disease (COVID-19) in X-ray and CT Images: A Machine Learning Based Approach. Biocybern

Biomed Eng 2021;41:867-879.
[50] Jin W, Dong S, Dong C, et al. Hybrid ensemble model for differential diagnosis between COVID-19 and common viral pneumonia by chest X-ray radiograph. Comput Biol Med 2021;131:104252.
[51] Rahman T, Khandakar A, Qiblawey Y, et al. Exploring the effect of image enhancement techniques on COVID-19 detection using chest X-ray images. Comput Biol Med 2021;132:104319.
[52] Tahir AM, Chowdhury MEH, Khandakar A, et al. COVID-19 infection localization and severity grading from chest X-ray images. Comput Biol Med 2021;139:105002.
[53] Degerli A, Ahishali M, Yamac M, et al. COVID-19 infection map generation and detection from chest X-ray images. Health Inf Sci Syst 2021;9:15.
[54] Chowdhury MEH, Rahman T, Khandakar A, et al. Can AI Help in Screening Viral and COVID-19 Pneumonia? IEEE Access 2020;8:132665-132676.
[55] Tahir AM, Chowdhury MEH, Qiblawey Y, et al. Available at: https://doi.org/10.34740/kaggle/dsv/3122958
[56] Ma J, Ge C, Wang YX, et al. Available at: https://doi.org/10.5281/zenodo.3757476
[57] Soares E, Angelov P, Biaso S, et al. SARS-CoV-2 CT-scan dataset: A large dataset of real patients CT scans for SARS-CoV-2 identification. MedRxiv 2020.
[58] Morozov SP, Andreychenko A, Pavlov N, et al. Mosmeddata: Chest ct scans with covid-19 related findings dataset (Preprint). ArXiv 2005.06465 2020.
[59] COVID-19 CT segmentation dataset. Available at: http://medicalsegmentation.com/covid19/
[60] Tabik S, Gomez-Rios A, Martin-Rodriguez JL, et al. COVIDGR Dataset and COVID-SDNet Methodology for Predicting COVID-19 Based on Chest X-Ray Images. IEEE J Biomed Health Inform 2020;24:3595-3605.
[61] Vayá MDLI, Saborit JM, Montell JA, et al. Bimcv covid-19+: a large annotated dataset of rx and ct images from covid-19 patients (Preprint). ArXiv 2006.01174 2020.
[62] Rahimzadeh M, Attar A, Sakhaei SM. A fully automated deep learning-based network for detecting covid-19 from a new and large lung ct scan dataset. Biomed Signal Process Control 2021;68:102588.
[63] Ning W, Lei S, Yang J, et al. iCTCF: an integrative resource of chest computed tomography images and clinical features of patients with COVID-19 pneumonia (Preprint). Res Sq 2020.
[64] Wang L, Lin ZQ, Wong A. COVID-Net: a tailored deep convolutional neural network design for detection of COVID-19 cases from chest X-ray images (Preprint). Sci Rep 2020;10:19549.
[65] Gunraj H, Sabri A, Koff D, et al. COVID-Net CT-2: Enhanced Deep Neural Networks for Detection of COVID-19 From Chest CT Images Through Bigger, More Diverse Learning. Front Med (Lausanne) 2021;8:729287.
[66] Maftouni M, Law ACC, Shen B, et al. A Robust Ensemble-Deep Learning Model for COVID-19 Diagnosis based on an Integrated CT Scan Images Database. Proceedings of the 2021 IISE Annual Conference. IISE 2021;632-637.
[67] Huang Y, Liu Z, He L, et al. Radiomics Signature: A Potential Biomarker for the Prediction of Disease-Free Survival in Early-Stage (I or II) Non-Small Cell Lung Cancer. Radiology 2016;281:947-957.
[68] Zhang D, Shen D. Predicting future clinical changes of MCI patients using longitudinal and multimodal biomarkers. PLoS One 2012;7:e33182.
[69] Zhou Z, Song Z, Chen Y, et al. A Novel CT-based Radiomics-Clinical Nomogram for the Prediction of Short-Term Prognosis in Deep Intracerebral Hemorrhage. World Neurosurg 2022;157:e461-e472.
[70] Keyl J, Kasper S, Wiesweg M, et al. Multimodal survival prediction in advanced pancreatic cancer using machine learning. ESMO Open 2022;7:100555.
[71] Zhang M, Zeng X, Huang C, et al. An AI-based radiomics nomogram for disease prognosis in patients with COVID-19 pneumonia using initial CT images and clinical indicators. Int J Med Inf 2021;154:104545.
[72] Younus S, Maqsood H, Sattar A, et al. A novel chest CT severity score in COVID-19 and its correlation with severity and prognosis of the lung disease: A retrospective cohort study. Ann Med Surg 2022;82:104692.
[73] Khoreva MA. Postcovid Syndrome - The New Reality. Neurosci Behav Physiol 2022;1-6.
[74] Sheikhbahaei S, Mena E, Yanamadala A, et al. The Value of FDG PET/CT in Treatment Response Assessment, Follow-Up, and Surveillance of Lung Cancer. AJR. AJR Am J Roentgenol 2017;208 2:420-433.
[75] Tadayyon H, Gangeh M, Sannachi L, et al. A priori prediction of breast tumour response to chemotherapy using quantitative ultrasound imaging and artificial neural networks. Oncotarget 2019;10:3910-3923.
[76] Mejia EJ, O'Connor MJ. The role of imaging in assessing disease severity and prognosis in cardiomyopathy. Prog Pediatr Cardiol 2020;59:101316.
[77] Yao W, Dong H, Qi J, et al. Safety and efficacy of mesenchymal stem cells in severe/critical patients with COVID-19: A systematic review and meta-analysis. EClinicalMedicine

2022;51:101545.
[78] Liao SH, Hung CC, Chen CN, et al. Assessing efficacy of antiviral therapy for COVID-19 patients: A case study on remdesivir with bayesian synthesis design and multistate analysis. J Formos Med Assoc 2021;120:S77-S85.
[79] Tobback E, Degroote S, Buysse S, et al. Efficacy and safety of camostat mesylate in early COVID-19 disease in an ambulatory setting: a randomized placebo-controlled phase II trial. Int J Infect Dis 2022;122:628-635.
[80] Wang Y, Lu C, Li H, et al. Efficacy and safety assessment of severe COVID-19 patients with Chinese medicine: A retrospective case series study at early stage of the COVID-19 epidemic in Wuhan, China. J Ethnopharmacol 2021;277:113888.

Progress in Medical Devices
eISSN:2957-5478

Review Article https://doi.org/10.61189/036308mdyran

Research progress on medical ultrasound image segmentation algorithms

Tianfeng Dong[1], Shiju Yan[1], Hengyu Li[2], Sheng Yuan[1]

[1]School of Health Science and Engineering, University of Shanghai for Science and Technology, Shanghai 200093, China. [2]Department of Breast and Thyroid Surgery, Changhai Hospital, Second Military Medical University/Naval Medical University, Shanghai 200433, China.

Corresponding author: Shiju Yan.

Declaration of conflict of interest: None.

Received May 8, 2023; Accepted November 23, 2023; Published December 31, 2023

Highlights

- Medical image segmentation algorithms play a crucial role in diagnosing and screening lesions.
- Appropriate segmentation techniques are conducive to reducing the workload of doctors and hold significant im plications for clinical auxiliary treatment.

Abstract

Medical ultrasound imaging is an integral part of preoperative diagnosis, lesion screening and ultrasound-guided interventional surgeries. Image segmentation techniques can enhance the identification of lesions and separate them from complex backgrounds, aiding physicians in both quantitative and qualitative analyses. Ultrasound image segmentation algorithms are primarily categorized into two types: traditional non-semantic segmentation and deep learning-based semantic segmentation, each with distinct advantages and drawbacks. This paper delves into these segmentation principles, elucidating their relevance in the realm of ultrasound image segmentation, and offers an overview of current research trends. Our goal is to provide guidance for physicians and researchers in selecting the most suitable segmentation algorithm that tailors to their specific requirements.

Keywords: Ultrasound imaging, deep learning, semantic segmentation, developmental trends

Introduction

Ultrasound has emerged as a pivotal modality in contemporary medicine due to its efficacy in imaging soft and muscular tissues. It has the advantages of rapid imaging, cost-effectiveness, absence of radiation, and real-time visualization of soft tissue structures compared to X-ray. Previously, mammography was the most effective tool for early detection of breast cancer, but it has obvious limitations, leading to misdiagnosis and many unnecessary biopsies (65-85%), as well as missed diagnoses, where 10-30% breast cancers were not detected in time [1-3]. Therefore, ultrasound imaging has become an important alternative to mammography. Research has shown that over one fourth of studies utilized ultrasound images, with the ratio growing at an accelerated rate [4]. Evidence suggests that ultrasound images are effective in differentiating benign from malignant tumors with high accuracy [5]. Additionally, they enhance the cancer detection rate by 17% and reduce unnecessary biopsies by 40% [6, 7].

However, ultrasound image interpretation requires well-trained and experienced radiologists. Even well-trained experts may have a high inter-observer variation rate. In recent years, computer-aided diagnosis has made great strides driven by advancements in computer technology, encompassing both computer vision and artificial intelligence [8]. Through computer-aided diagnosis, it is feasible to differentiate between benign and malignant breast tumors by analyzing their boundaries and morphology [9]. Moreover, segmentation

Address correspondence to: Shiju Yan, School of Health Science and Engineering, University of Shanghai for Science and Technology, No.516 Jungong Road, Yangpu District, Shanghai 200093, China. Tel: 18217617984; E-mail: yanshiju@usst.edu.cn.

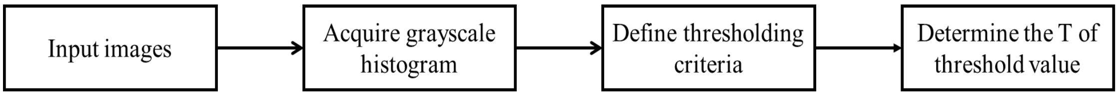

Figure 1. Basic flowchart of threshold segmentation.

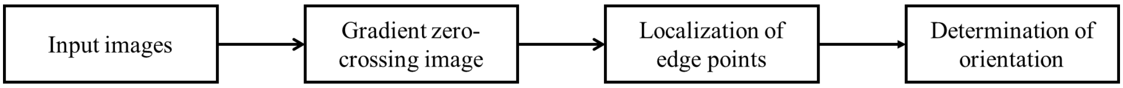

Figure 2. Basic flowchart of edge segmentation using differential operator.

algorithms play a crucial role in identifying needle tips in ultrasound images, potentially reducing and compensating for surgeon fatigue during minimally invasive procedures [10].

Despite the advantages, ultrasound imaging also comes with challenges, namely limited resolution, ambiguous lesion boundaries, and the presence of speckle noise, all of which complicate accurate lesion segmentation. Therefore, accurate segmentation of lesions within ultrasound images remains a pressing challenge. While numerous image segmentation algorithms exist, this paper delves into the diverse domains of current ultrasound image segmentation algorithms and their applications. Furthermore, a summary and future outlook are provided, aiming to serve as a reference for researchers and medical practitioners.

Methods

Non-Semantic Ultrasound Image Segmentation

Traditional image segmentation algorithms rely on fundamental features, such as color and texture, to segment desired objects or regions. Owing to their high computational efficiency and consistent performance, these techniques have emerged as predominant in image segmentation applications. Notably, techniques rooted in edge detection, regional attributes and deformation models are commonly employed.

Edge-Based Ultrasound Image Segmentation

Edge-based image segmentation algorithms identify edges by analyzing the distinctiveness of pixels across different regions, primarily using threshold segmentation and differential operators.

Threshold segmentation stands out due to its ubiquitous applicability and foundational principle: discernible grey-scale disparities exist between foreground and background regions, which allows for the determination of a suitable threshold, T, differentiating the foreground from the background, as shown in **Figure 1** [11]. The Otsu method optimizes segmentation by selecting a threshold, T, that maximizes or minimizes the interclass variance across distinct regions [12]. An enhancement to the Otsu algorithm, as detailed by Hui-Fuang Ng, ensures that the threshold, T, aligns optimally with the valley of variance [13]. In ultrasound image, lesions exhibit a notably denser grey value distribution. The maximum entropy thresholding algorithm exploits this density, calculating the information entropy of image to pinpoint the ideal threshold, T, at the position of maximum entropy [14].

Local differential operators, including the Laplacian, Sobel, and Canny operators, facilitate edge detection for image segmentation [15, 16]. As shown in **Figure 2**, these operators operate on the premise that first-order derivatives present extreme values at greyscale transitions, while second-order derivatives manifest non-zero points. However, in ultrasound image, the inherent discontinuity and high-frequency noise complicate lesion edge identification when relying solely on differential operators. To address these challenges, several enhancements have been proposed. For instance, researchers have utilized the nonlinear Laplacian operator to identify pixels associated with second-order derivative changes and augmented edge pixel definition for better segmentation [17]. Additionally, Fan et al. introduced nonlinear wavelets for segmenting the inner and outer boundaries of tubular artery ultrasound images [18].

Region-Based Ultrasound Image Segmentation

As shown in **Figure 3**, region-based algorithms offer a method for image segmentation, encompassing both the region growth and watershed algorithms. These algorithms segment images based on internal region similarity. Specifically, the region-growing algorithm identifies seed pixels through a defined growth criterion. It then amalgamates pixels sharing similar characteristics across disparate regions, forming

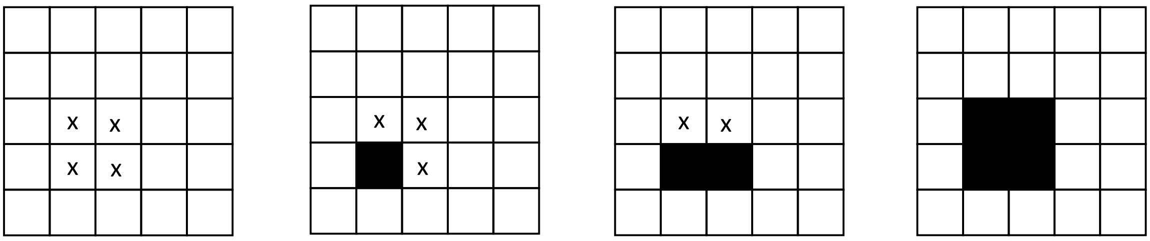

Figure 3. Region growing algorithm.

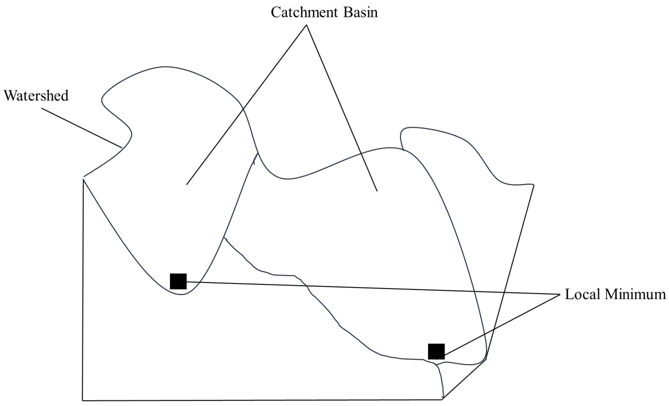

Figure 4. Watershed algorithm.

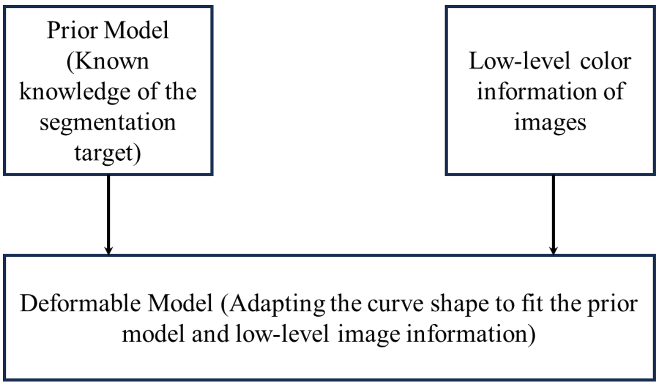

Figure 5. Basic flowchart of deformation model segmentation.

distinct regions for ultrasound image segmentation [19]. Fan et al. introduced a method that incorporates two constraints to autonomously identify seed pixels within breast tumor lesions [20]. This method innovatively merges iterative quadrinomial tree decomposition with greyscale values, thereby enhancing the segmentation of ultrasound image lesions.

As shown in **Figure 4**, the watershed algorithm, commonly referred to as watershed segmentation, interprets the grayscale of an image as analogous to the topographical features of the surface of earth, with the grayscale values representing a third-dimensional elevation perspective [21]. Though prevalently employed in pattern recognition and medical imaging, the watershed method frequently suffers from over-segmentation. To counteract this, Weickert et al. introduced a region-merging approach as an enhancement [22]. Additionally, the challenge of over-segmentation was tackled by Jung et al. through an integration of the watershed algorithm with wavelet transform [23]. Further, Gomez et al. applied the watershed algorithm to segment breast ultrasound images by using constraints on the textural features derived from the Gabor filter [24].

Deformation Model-Based Ultrasound Image Segmentation

The concept of deformation model draws inspiration from physics and geometric theories. This model assimilates relevant grayscale and texture information from image data to segment targets following predefined criteria, as shown in **Figure 5**.

The active contour model, often referred to as the snake model, provides a robust framework for delineating the contour of an image target through the minimization or maximization of an energy functional [25]. The curve evolution process of this model autonomously determinate the interior of the curve and maintains its smooth transition. An external force guides the curve towards the boundaries of the region of interest (ROI), as influenced by the image's constraints and potential energy.

The region-based active contour Chan-Vese model was proposed by Wang et al. [26]. The Chan-Vese model proposed by Hmida et al. incorporates a new segmentation algorithm to obtain a model that depicts the contour of the mass [27]. Specifically, Kuo et al. segmented breast ultrasound images using radial gradient index contour [28]. Gu et al. proposed an improved approach based on the aforementioned algorithm by providing an edge-based deformation model [29]. To accurately track the local changes in grayscale

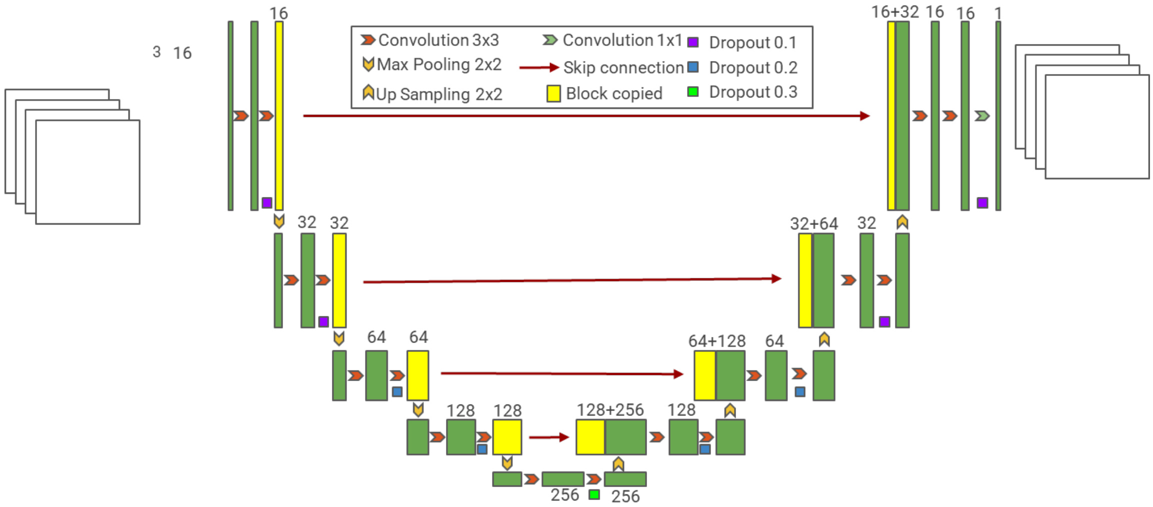

Figure 6. U-Net model.

in the ultrasound image, Li et al. utilized the local attribute of the kernel function, based on the region-scalable fitting method [30]. This algorithm is highly effective in segmenting images with uneven grayscale distributions. Moreover, an active contour model based on Bhattacharyya gradient flow was proposed to treat the target area and background area of images as different samples [31]. To achieve the goal of image segmentation without depending on the uniformity information of the super-grayscale image, the issue is transformed into a probabilistic model problem by computing the Babbitt distance between the two sample distributions. Yuan et al. proposed a model called region-scalable fitting and Bhattacharyya distance that combines the benefits of the region-scalable fitting model and the Bhattacharyya gradient flow model to solve the problem of uneven gray levels and blurring borders in ultrasound images [32].

Deep Learning-Based Ultrasound Image Segmentation

Convolutional neural networks (CNNs) are a specialized category in deep learning architectures designed to process structured grid data, such as images [33]. A typical CNN comprises convolutional layers, pooling layers, and fully connected layers. This design equips CNNs with robust feature extraction and data abstraction capabilities. Instead of relying on handcrafted features, CNNs can automatically recognize correlations between inputs and outputs through adaptive learning, making them particularly suitable for tasks such as image segmentation and classification.

U-Shaped and Its Derivative Networks

U-Net represents a pivotal advancement in medical image segmentation and continues to be a prominent semantic segmentation algorithm, as shown in **Figure 6** [34]. Within its architecture, the shallow convolutional layers predominantly capture spatial and textural nuances due to their limited receptive field and high-resolution capacity. In contrast, the deep convolutional layers can discern broader semantic features, facilitated by an expansive receptive field and lower resolution. Distinctively, U-Net exhibits a symmetrical encoder-decoder configuration, fostering an integration between shallow and deep feature representations. This architectural nuance equips U-Net with the capability to concurrently process both texture-oriented features and high-level semantic features, thereby augmenting its receptive field and enhancing segmentation precision.

Various enhancements have been proposed to bolster the original U-Net architecture. The recurrent residual U-Net addresses the degradation in segmentation results that attributed to gradient explosion or vanishing, particularly as the network deepens [35]. Furthermore, the adoption of Prelu as an activation function has been suggested to optimize the network's performance. Karthik et al. introduced a multi-level U-Net, which is capable of real-time segmentation of breast masses in ultrasound images [36]. U-Net++ innovatively incorporates a dense connection between each convolutional layer, performing upsampling and feature fusion on the encoder-generated feature map to bridge the disparity between the encoder and the decoder [37, 38]. In a different approach, residual U-Net employs the residual network as its backbone, enhancing the convolution module traditionally used in U-Net [39, 40]. Building

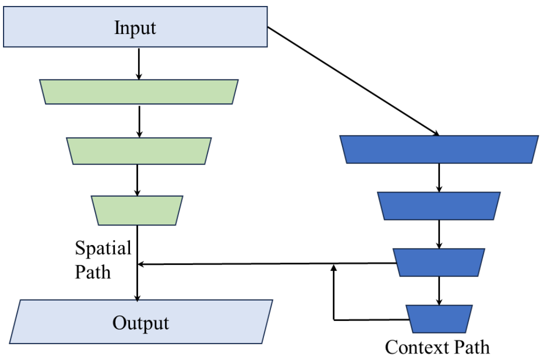

Figure 7. The spatial path and context path of BiSeNet .

upon this, ResUNet++ integrates a squeeze and extraction block to emphasize pivotal channels within the network, consequently suppressing less significant ones [41, 42]. Furthermore, the SK-U-Net approach refines the ROI of network towards the lesion using channel attention, resulting in the selective kernel module delivering superior segmentation outcomes during the segmentation of lesions in ultrasound breast images [43].

Advancements in U-Net data processing techniques are well documented, with a specific emphasis on data augmentation strategies. Zeiser et al. detailed an approach that enhances data through techniques such as contrast enhancement and flipping, while concurrently removing extraneous information from images by using U-Net [44]. In the more recent development, nnU-Net accentuates the significance of data augmentation [45]. Rather than primarily focusing on the model, nnU-Net is dedicated to understand how varying segmentation tasks influence the final resulting segmentation. Consequently, nnUnet prioritizes data pre-processing, post-processing, and tailoring hyperparameter settings to cater to specific models for different tasks. This comprehensive approach aims to elevate both the efficiency and accuracy of segmentation tasks. Presently, the segmentation outcomes from nnUnet have become a benchmark for evaluating novel segmentation models.

Lightweight Networks

Fully convolutional network (FCN) represents a paradigm shift in image segmentation, notably decreasing computational demands by substituting the fully connected layers found in traditional CNNs with convolutional layers [46]. In SegNet, the deconvolution inherent to FCN is superseded by upsampling through nonlinear interpolation, further mitigating computational demands [47]. However, the existing parameter-intensive nature of these models constrains their applicability for real-time processing in scenarios like clinical surgeries or mobile ultrasound-embedded devices.

In this context, Hu et al. reported an efficacious application of BiSeNet for segmenting pediatric ultrasound images of the left and right ventricles, demonstrating superior speed and accuracy relative to U-Net [48, 49]. BiSeNet introduces a bidirectional segmentation framework that coordinates two pathways: the spatial path and the context path as shown in **Figure 7**. The spatial path emphasizes the preservation of spatially rich feature maps, while the context path rapidly downsamples to assimilate high-level semantic information, culminating in an expansive perceptual field via global average pooling.

BiSeNet V2 refines this framework through incorporating a guided aggregation layer to bolster the synergy of spatial and semantic features [50]. Additionally, it enriches both spatial and semantic branches, interweaving an attention mechanism to amplify speed and precision. An insightful deviation is presented in “Rethinking BiseNet” where the short-term dense concatenate module is posited as the backbone network, replacing the classification-centric backbone of BiSeNet [51]. This architectural shift, enabled by the short-term dense concatenate module, markedly amplifies network performance, granting an expansive receptive field with a constrained parameter set.

Applications in Ultrasound Image Segmentation

Image Segmentation in Coronary Artery Disease

Vascular ultrasound is instrumental in the management of coronary artery disease. Its utility extends from the detailed delineation of coronary artery anatomy, providing critical guidance in the selection and evaluation of interventional strategies. The imaging modality offers an intricate view of blood vessel and tissue morphology, allowing clear visualization of structures beneath the intima and accurate measurements of vascular lumen diameters. Given its diagnostic accuracy, segmentation of vascular tissue structures is of paramount importance.

Sonka et al. employed the snake algorithm for coronary artery segmentation, incorporating prior knowledge of vessel cross-sections during model deformation [52]. This knowledge encompasses target edges, shapes, edge orientations, and vessel wall thickness, reflecting manual segmentation procedures. In the study of Bouma et al., a lumen segmentation algorithm was proposed, combining a suite of filtering techniques: Gaussian, median, and anisotropic filters [53]. Coupled with distinct segmentation methodologies, including the threshold, region expansion, and discrete active contour methods, the algorithm's performance was evaluated by experts [54]. However, its efficacy is compromised in the presence of significant image noise, resulting in suboptimal segmentation outcomes relative to expert-driven benchmarks. Pardo et al. introduced a statistical deformation model tailored for coronary artery segmentation by using a derived Gaussian filter for local edge delineation in varying directions [55]. This approach contrasts image features with established knowledge, guiding the deformation using linear discriminant analysis. This optimization streamlines the feature space and enhances the robustness of the model.

Yang et al. introduced an innovative approach dubbed "intravascular ultrasound segmentation network" for coronary artery segmentation using deep learning [56]. The network is rooted in the FCN architecture and employs an aggregated multi-branch structure, integrating features from both U-Net and SegNet in a symmetric layout. The encoding segment comprises four distinct modules, while the decoding segment consists of three. Crucially, skip connections are employed to furnish the decoder with supplementary information. Post-segmentation, an elliptical contour fitting process further refines the result. Compared to conventional methods, intravascular ultrasound segmentation network notably enhances segmentation accuracy.

Breast Ultrasound Image Segmentation

The abundant adipose tissue in breast causes over-segmentation, unclear lesion borders, low contrast, and increased shadows. As a solution to these issues, a three-step method for breast mass segmentation based on superpixel creation and curve development was proposed [57]. This method is based on the creation of superpixels and curve development, utilizing the simple linear iterative clustering method and density-based spatial clustering of applications with noise for breast mass detection and generating mammogram superpixels. Subsequently, ROI in breast masses are constructed, followed by a fitting approach based on local Gaussian distribution to capture the edge of the breast tumor through graphic block processing and spatial constraints. This method effectively eliminates the false positive region of the ROI and provides improved segmentation results by capturing the margin of the breast tumor more accurately.

Wang et al. proposed a novel solution to the complex issue of detecting malignancies in breast ultrasound images: the multi-level nested pyramid network (MNPNet) [58]. The center of MNPNet's design is an encoder module that integrates both ResNet34 and atrous spatial pyramid pooling modules. This configuration ensures efficient encoding of context features from multiple levels, capturing both low-level details and high-level semantic information. On the other hand, the decoder module uses bilinear upsampling and a feature fusion technique, enhancing the segmentation precision of tumor border regions. Collectively, the MNPNet framework outperforms other methods in breast imaging analysis and holds promise for improving diagnostic accuracy in clinical practice.

Ultrasound-Guided Interventional Surgery

Ultrasound-guided minimally invasive surgery employs specialized puncture needles to access lesions through the skin, facilitating procedures like radiofrequency thermal ablation and needle puncture biopsy [59, 60]. This technique allows for localized treatment and minimally invasive surgical intervention on tumor lesions. Notable benefits include the absence of radiation exposure, rapid recovery, and cost-effectiveness. However, inherent challenges of original ultrasound images, such as low resolution, high noise, and difficulty pinpointing lesion locations, still exist. Consequently, during surgery, physicians must continuously monitor the position of the tip of the puncture needle, which is critical to the success of the operation. Thus, compared to other surgical procedures, ultrasound-guided minimally invasive surgery tends to be more reliant on the surgeon's experience.

To accurately pinpoint the position of the puncture needle in real-time during surgery, Mwikirize et al. broke the process down into three stages [61]. First, the movement of the needle tip was identified and amplified within the ultrasound image, keeping the needle tip component in the foreground and relegating the rest to the background. Second, a regularization

Table 1. Summary of traditional non-semantic segmentation algorithms

Algorithm reference	Algorithm type	Algorithm overview
Ng HF. 2006 [13]	Threshold segmentation algorithm	Identifying an appropriate threshold value, T, where inter-class variance between regions is maximized or minimized.
Kapur et al. 1988 [15]	Threshold segmentation algorithm	Utilizing the maximum entropy threshold segmentation algorithm.
Aarnink et al. 1994 [17]	Edge detection segmentation algorithm	Segmenting edge pixels using the nonlinear Laplacian operator for second-order derivative boundaries.
Fan et al. 1996 [18]	Edge detection segmentation algorithm	Segmenting edge pixels using nonlinear wavelet detection.
Fan et al. 2019 [20]	Region segmentation algorithm	Using iterative quadrinomial tree decomposition with grayscale features to establish two constraint conditions for automatic seed pixel identification.
Gomez et al. 2010 [24]	Region segmentation algorithm	Using texture features generated by Gaussian-constrained Gabor filters combined with the Watershed algorithm for segmentation.
Kuo et al. 2013 [28]	Deformable model	Contour segmentation using the Radial Gradient Index.
Yuan J. 2012 [32]	Deformable model	Introducing the region-scalable fitting and Bhattacharyya distance model, merging region-scalable fitting and Bhattacharyya gradient flow benefits, to tackle uneven grayscale and blurriness

Table 2. Summary of deep learning semantic segmentation algorithms

Algorithm reference	Algorithm type	Algorithm overview
Ronneberger O et al. 2015 [34]	U-Net model	Using symmetrical U-shape with skip connections to merge shallow and deep features
Zhou Z et al. 2018 [37]	U-Net model	Added dense connections between convolutional layers.
Zhang Z et al. 2018 [39]	U-Net model	Replacing Backbone with Residual Network
Isensee F et al. 2021 [45]	U-Net model	Emphasizing data pre/post-processing and task-specific hyperparameter tuning
Badrinarayanan V et al. 2017 [47]	Lightweight network	Upsample with nonlinear interpolation, reducing computations.
Yu C et al. 2018 [49]	Lightweight network	Bidirectional segmentation for space info retention and wider receptive field.
Yu C et al. 2021 [50]	Lightweight network	Enhanced spatial and semantic branches with attention mechanism.

filter was deployed to further emphasize the tip and extracted its form features. Finally, the modified Yolo network architecture was utilized to localize the needle tip within the original ultrasound image [62]. On the other hand, Mwikirize recommended classifying the needle tip before any augmentation [63]. If there's spatial movement, the tip is enhanced; otherwise, it remains untouched. This selective approach avoids enhancing every frame, thereby reducing computational demands and accelerating the process.

Summary and outlook

Summary

This paper provides an overview of several ultrasound image segmentation algorithms employed in the realm of medical ultrasound, highlighting their evolution alongside advances in computer technology. Each algorithm presents its own strengths and weaknesses.

The traditional non-semantic image segmentation algorithm is both straightforward and swift. The main traditional non-semantic segmentation algorithms are shown in **Table 1**. They perform effectively on individual images where there's a pronounced contrast between the lesion and the surrounding regions. However, these traditional methods struggle to process ultrasound images with complex composition and high noise, posing challenges like unclear border segmentation.

The deformation model improves the accuracy of ultrasound image segmentation. Nevertheless, it comes with its own drawbacks, such as intricate computations, inability to achieve automatic segmentation, and imprecise boundary tracking.

Deep learning-based segmentation stands out for its superior quality and speed. The main deep learning semantic segmentation algorithms are shown in **Table 2**. By using a lightweight network, it can achieve fully automated segmentation in real-time. The main challenge here lies in the initial phase: a substantial amount of manually labeled data are essential for training the neural network.

Outlook

Effective ultrasound image segmentation aims to improve automated segmentation performance, enhance segmentation accuracy, and reduce computational demands. While critical to the creation and analysis of medical images, this process faces multiple challenges. Conventional algorithms and deformation models often fall short in delivering high-precision segmentation for ultrasound images. Furthermore, the extensive application of deep learning is hindered by the limited availability of medical image data. Additionally, it is also challenging to ideally balance the speed and accuracy for real-time segmentation, limiting its clinical application.

Looking ahead, it’s imperative to meld medical knowledge with image segmentation algorithms. Integrating traditional segmentation techniques with deep learning algorithms can be the linchpin for elevating clinical diagnosis efficacy. To counteract the data scarcity issue, datasets can be expanded using unsupervised learning. Future network designs must harmoniously balance speed and accuracy, broadening their applicability in the ultrasound imaging domain.

References

[1] Cheng HD, Shi X, Min R, et al. Approaches for automated detection and classification of masses in mammograms. Pattern Recognit 2006;39:646-668.

[2] Jesneck JL, Lo JY, Baker JA. Breast mass lesions: computer-aided diagnosis models with mammographic and sonographic descriptors. Radiology 2007;244:390-398.

[3] Giger ML. Computer-aided diagnosis in radiology. Acad Radiol 2002;9:1-3.

[4] Chang RF, Wu WJ, Moon WK, et al. Improvement in breast tumor discrimination by support vector machines and speckle-emphasis texture analysis. Ultrasound Med Biol 2003;29:679-686.

[5] Sahiner B, Chan H-P, Roubidoux MA, et al. Malignant and benign breast masses on 3D US volumetric images: effect of computer-aided diagnosis on radiologist accuracy. Radiology 2007;242:716-724.

[6] Drukker K, Giger ML, Horsch K, et al. Computerized lesion detection on breast ultrasound. Med Phys 2002;29:1438-1446.

[7] André MP, Galperin M, Olson LK, et al. Improving the accuracy of diagnostic breast ultrasound. Acoust Imaging 2002;453-460.

[8] Chen HL, Zhou JQ, Chen Q, et al. Comparison of the sensitivity of mammography, ultrasound, magnetic resonance imaging and combinations of these imaging modalities for the detection of small (≤ 2 cm) breast cancer. Medicine 2021;100.

[9] Stoeblen F, Landt S, Ishaq R, et al. High-frequency breast ultrasound for the detection of microcalcifications and associated masses in BI-RADS 4a patients. Anticancer Res 2011;31:2575-2581.

[10] Mwikirize C, Kimbowa AB, Imanirakiza S, et al. Time-aware deep neural networks for needle tip localization in 2D ultrasound. Int J Comput Assist Radiol Surg 2021;16:819-827.

[11] Cheng H-D, Jiang XH, Sun Y, et al. Color image segmentation: advances and prospects. Pattern Recognit 2001;34:2259-2281.

[12] Otsu N. A threshold selection method from gray-level histograms. IEEE Trans Syst Man Cybern 1979;9:62-66.

[13] Ng HF. Automatic thresholding for defect detection. Pattern Recognit Lett 2006;27:1644-1649.

[14] Kapur JN, Sahoo PK, Wong AK. A new method for gray-level picture thresholding using the entropy of the histogram. Comput Vis Graphics Image Process 1985;29:273-285.

[15] Kanopoulos N, Vasanthavada N, Baker RL. Design of an image edge detection filter using the Sobel operator. IEEE J Solid-State Circuits 1988;23:358-367.

[16] Ding L, Goshtasby A. On the Canny edge detector. Pattern Recognit 2001;34:721-725.

[17] Aarnink R, Giesen R, Huynen A, et al. A practical clinical method for contour determination in ultrasonographic prostate images. Ultrasound Med Biol 1994;20:705-717.

[18] Fan L, Braden GA, Herrington DM. Nonlinear wavelet filter for intracoronary ultrasound images. Comput Cardiol 1996 1996;41-44.

[19] Lázár I, Hajdu A. Segmentation of retinal

vessels by means of directional response vector similarity and region growing. Comput Biol Med 2015;66:209-221.

[20] Fan H, Meng F, Liu Y, et al. A novel breast ultrasound image automated segmentation algorithm based on seeded region growing integrating gradual equipartition threshold. Multimedia Tools Appl 2019;78:27915-27932.

[21] Ng H, Ong S, Foong K, et al. Medical image segmentation using k-means clustering and improved watershed algorithm. 2006 IEEE Southwest Symposium on ImageAnalysis and Interpretation 2006;61-65.

[22] Weickert J. Efficient image segmentation using partial differential equations and morphology. Pattern Recognit 2001;34:1813-1824.

[23] Jung CR. Combining wavelets and watersheds for robust multiscale image segmentation. Image Vis Comput 2007;25:24-33.

[24] Gomez W, Leija L, Alvarenga A, et al. Computerized lesion segmentation of breast ultrasound based on marker-controlled watershed transformation. Med Phys 2010;37:82-95.

[25] Kass M, Witkin A, Terzopoulos D. Snakes: Active contour models. Int J Comput Vis 1988;1:321-331.

[26] Wang X-F, Huang D-S, Xu H. An efficient local Chan–Vese model for image segmentation. Pattern Recognit 2010;43:603-618.

[27] Hmida M, Hamrouni K, Solaiman B, et al. Mammographic mass segmentation using fuzzy contours. Comput Methods Programs Biomed 2018;164:131-142.

[28] Kuo HC, Giger ML, Reiser I, et al. Automatic 3D lesion segmentation on breast ultrasound images. Med Imag 2013;8670:555-560.

[29] Gu P, Lee WM, Roubidoux MA, et al. Automated 3D ultrasound image segmentation to aid breast cancer image interpretation. Ultrasonics 2016;65:51-58.

[30] Li C, Kao C-Y, Gore JC, et al. Minimization of region-scalable fitting energy for image segmentation. IEEE Trans Image Process 2008;17:1940-1949.

[31] Michailovich O, Rathi Y, Tannenbaum A. Image segmentation using active contours driven by the Bhattacharyya gradient flow. IEEE Trans Image Process 2007;16:2787-2801.

[32] Yuan J. Active contour driven by region-scalable fitting and local Bhattacharyya distance energies for ultrasound image segmentation. IET Image Process 2012;6:1075-1083.

[33] Shin HC, Roth HR, Gao M, et al. Deep convolutional neural networks for computer-aided detection: CNN architectures, dataset characteristics and transfer learning. IEEE Trans Image Process 2016;35:1285-1298.

[34] Ronneberger O, Fischer P, Brox T. U-net: Convolutional networks for biomedical image segmentation. Lecture Notes in Computer Science (9351): Medical Image Computing and Computer-Assisted Intervention–MICCAI 2015. Springer, Cham 2015.

[35] Alom MZ, Hasan M, Yakopcic C, et al. Recurrent residual convolutional neural network based on u-net (r2u-net) for medical image segmentation (Preprint). ArXiv 2018.

[36] Karthik L, Kumar G, Keswani T, et al. Protease inhibitors from marine actinobacteria as a potential source for antimalarial compound. PloS one 2014;9:e90972.

[37] Zhou Z, Siddiquee MMR, Tajbakhsh N, et al. UNet++: A Nested U-Net Architecture for Medical Image Segmentation. Deep Learn Med Image Anal Multimodal Learn Clin Decis Support (2018) 2018;11045:3-11.

[38] Huang G, Liu Z, Maaten LV, et al. Densely connected convolutional networks. 2017 IEEE Conference on Computer Vision and Pattern Recognition (CVPR) 2017;2261-2269

[39] Zhang Z, Liu Q, Wang Y. Road extraction by deep residual u-net. IEEE Geosci Remote Sens 2018;15:749-753.

[40] He K, Zhang X, Ren S, et al. Deep residual learning for image recognition. 2016 IEEE Conference on Computer Vision and Pattern Recognition (CVPR) 2016;779-778

[41] Jha D, Smedsrud PH, Riegler MA, et al. Resunet++: An advanced architecture for medical image segmentation. 2019 IEEE international symposium on multimedia (ISM) 2019;225-2255.

[42] Hu J, Shen L, Sun G. Squeeze-and-excitation networks. 2018 IEEE/CVF Conference on Computer Vision and Pattern Recognition 2018;7132-7141.

[43] Byra M, Jarosik P, Szubert A, et al. Breast mass segmentation in ultrasound with selective kernel U-Net convolutional neural network. Biomed Signal Process Control 2020;61:102027.

[44] Zeiser FA, da Costa CA, Zonta T, et al. Segmentation of masses on mammograms using data augmentation and deep learning. J Digit Imaging 2020;33:858-868.

[45] Isensee F, Jaeger PF, Kohl SA, et al. nnU-Net: a self-configuring method for deep learning-based biomedical image segmentation. Nat Methods 2021;18:203-211.

[46] Long J, Shelhamer E, Darrell T. Fully convolutional networks for semantic segmentation. 2015 IEEE Conference on Computer Vision and Pattern Recognition (CVPR) 2015;3431-3440.

[47] Badrinarayanan V, Kendall A, Cipolla R. Segnet: A deep convolutional encoder-decoder

architecture for image segmentation. IEEE Trans Pattern Anal Mach Intell 2017;39:2481-2495.
[48] Hu Y, Guo L, Lei B, et al. Fully automatic pediatric echocardiography segmentation using deep convolutional networks based on BiSeNet. 2019 41st Annual International Conference of the IEEE Engineering in Medicine and Biology Society (EMBC) 2019;6561-6564.
[49] Yu C, Wang J, Peng C, et al. Bisenet: Bilateral segmentation network for real-time semantic segmentation. Lecture Notes in Computer Science (11217): Computer Vision–ECCV 2018. Springer, Cham 2018;334-349.
[50] Yu C, Gao C, Wang J, et al. Bisenet v2: Bilateral network with guided aggregation for real-time semantic segmentation. Int J Comput Vis 2021;129:3051-3068.
[51] Fan M, Lai S, Huang J, et al. Rethinking bisenet for real-time semantic segmentation. 2021 IEEE/CVF Conference on Computer Vision and Pattern Recognition (CVPR). 2021;9711-9720.
[52] Sonka M, Zhang X, Siebes M, et al. Segmentation of intravascular ultrasound images: A knowledge-based approach. IEEE Trans Image Process 1995;14:719-732.
[53] Bouma CJ, Niessen WJ, Zuiderveld KJ, et al. Automated lumen definition from 30 MHz intravascular ultrasound images. Med Image Anal 1997;1:363-377.
[54] Lobregt S, Viergever MA. A discrete dynamic contour model. IEEE Trans Image Process 1995;14:12-24.
[55] Pardo XM, Radeva P, Cabello D. Discriminant snakes for 3D reconstruction of anatomical organs. Med Image Anal 2003;7:293-310.
[56] Yang J, Tong L, Faraji M, et al. IVUS-Net: An intravascular ultrasound segmentation network. Lecture Notes in Computer Science (11010): Smart Multimedia–ICSM 2018. Springer, Cham 2018;367-377.
[57] Gu S, Chen Y, Sheng F, et al. A novel method for breast mass segmentation: from superpixel to subpixel segmentation. Mach Vis Appl 2019;30:1111-1122.
[58] Wang R, Ma Y, Sun W, et al. Multi-level nested pyramid network for mass segmentation in mammograms. Neurocomputing 2019;363:313-320.
[59] Rhim H, Dodd III GD. Radiofrequency thermal ablation of liver tumors. J Clin Ultrasound 1999;27:221-229.
[60] Martin HE, Ellis EB. Biopsy by needle puncture and aspiration. Ann Surg 1930;92:169.
[61] Mwikirize C, Nosher JL, Hacihaliloglu I. Learning needle tip localization from digital subtraction in 2D ultrasound. Int J Comput Assist Radiol Surg 2019;14:1017-1026.
[62] Redmon J, Farhadi A. YOLO9000: better, faster, stronger. 2017 IEEE Conference on Computer Vision and Pattern Recognition (CVPR). 2017;6517-6525.
[63] Mwikirize C, Nosher JL, Hacihaliloglu I. Single shot needle tip localization in 2D ultrasound. Lecture Notes in Computer Science (11768): Medical Image Computing and Computer Assisted Intervention–MICCAI 2019. Springer, Cham 2019;637-645.

Progress in Medical Devices
eISSN: 2957-5478

Research Article https://doi.org/10.61189/299269sghbqx

Design and simulation of a multi-functional radiofrequency tissue welding electrode

Wanwen Yang, Lin Mao, Yilong Chen, Chengli Song

Shanghai Institute for Minimally Invasive Therapy, School of Health Science and Engineering, University of Shanghai for Science and Technology, China, 200093

Corresponding author: Lin Mao.

Declaration of conflict of interest: None.

Received August 21, 2023; Accepted December 6, 2023; Published December 31, 2023

Highlights

- Two novel electrodes (one with circle surface and the other with square and arched surface) were designed for radiofrequency intestinal anastomosis, and their effects were compared to a control electrode (smoot surface).
- The temperature and thermal damage to tissue produced by the two designed electrodes during welding are lower than those by the control electrode.
- The electrode with square and arched surface has a smaller effective welding area and better effect on intestinal anastomosis.

Abstract

Purpose: To explore the effect of electrode structure on welding quality by modifying the structure of magnesium alloy electrode. **Methods:** Two novel electrodes were designed in this study, including one with a circle (C) surface and the other with a square and arched (SA) surface. The designed electrodes were compared to a control electrode with a smooth surface in terms of temperature distribution, thermal damage to tissue, and effective welding area. Finite element analysis was used to analyze the stress and strain of all electrodes and thermal damage to the tissue. **Results:** Pressure applied to the designed electrodes was within the elastic limit, and the deformation was less than 1%. The highest temperature of SA electrode (99.6 ℃) was similar to that of the control (100 ℃), while that of C electrode (106 ℃) was higher than the control. The mean temperature at the welding site in intestine of the control electrode was significantly higher than that of the other two electrodes. Besides, the mean temperature of C electrode was also slightly higher than that of SA electrode. The tissues welded by the control electrode, C electrode and SA electrode were completely necrotic within an axial distance of 2.546 mm, 2.079 mm, and 1.835 mm from the edge of the welding area, respectively. **Conclusion:** SA electrode has the lowest thermal damage compared with the other two electrodes due to smaller effective welding area. Therefore, SA electrode is better than the other two electrodes.

Keywords: Radiofrequency energy, electrode structure, anastomosis, thermal damage

I. Introduction

In 2020, the Global Cancer Statistics Report stated that colorectal cancer is a highly prevalent cancer, and its incidence and mortality are among the top five of all cancers [1]. Clinically, the primary treatment methods for colorectal cancer include surgery, radiation therapy, chemotherapy, and targeted therapy [2]. Surgical resection is a predominant treatment approach that widely used in all stages of colorectal cancer [3].

Surgical site infections (SSIs) are one of the most common complications after surgery, with implications for both clinical outcomes and medical costs [4, 5]. The incidence of SSIs due to large quantity and complexity of bacteria in the colorectal intestinal lumen ranges from 3% to 26%, representing a significant factor contributing to deterioration and death of patients [6-8]. Anastomotic leakage, bleeding, and disruption of incision are the independent risk factors for SSIs in colorectal cancer [9]. Therefore, a safe and reliable anastomosis method plays a significant role in surgical treatment efficacy.

Address correspondence to: Lin Mao, Shanghai Institute for Minimally Invasive Therapy, School of Health Science and Engineering, NO.516, Jungong Road, Yangpu District, Shanghai 200093, China. Tel: +86-21-55572159. E-mail: linmao@usst.edu.cn.

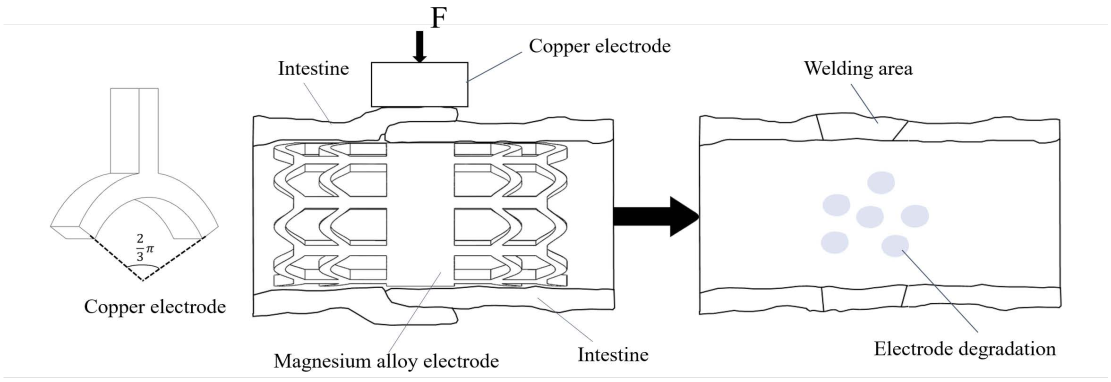

Figure 1. Working process of novel electrode.

Suturing and stapling are two conventional intestinal anastomosis techniques [10]. Both of them are discontinuous tissue matching. Consequently, complications such as anastomotic leakage and bleeding often occur [11]. With the further development of medical technology, anastomosis techniques have gradually evolved towards minimally invasive surgery. Biological adhesives, energy welding, and other technologies have been gradually applied in anastomosis [12]. However, common biological adhesives have problems such as poor adhesive elasticity, strong tissue toxicity, and rejection reaction. As a result, bio-adhesives are difficult to be used widely [13, 14]. The energy-based tissue fusion technology suggests that tissue healing can be achieved by heating the tissue with energy such as light, electricity, acoustic waves to coagulate and bind the proteins in the tissues at welding site [15-17].

With the progress of electrosurgical technology, researchers have found that while heating the tissue, the triple helical structure of type I collagen monomers uncoils and transmutes to a randomly coiled mass of peptide chains [18]. The peptide chains solidify into a fused mass while two tissue layers are compressed together [19]. In 2006, Salameh et al. used LigaSure system to suture blood vessels, which was the first application of radiofrequency (RF) energy for anastomosis [20]. In 2014, Zhou et al. explored the feasibility and effectiveness of intestinal anastomosis in an in vitro porcine model with high-frequency welding device [21]. However, this technology has been hindered due to problems such as tissue thermal damage and insufficient anastomotic strength. Henceforth, a series of studies have been conducted to continuously improve the welding quality of intestinal tissue by altering the processing parameters such as extrusion pressure, welding temperature, duration of heat, and electrode structure [22, 23]. In 2015, Zhao et al. studied the effect of electrode structure and pressure on anastomosis in isolated pigs and showed that an optimized electrode structure could contribute to the anastomosis outcome [24]. In 2019, Tu et al. changed control parameters (power, interval time, and terminal impedance) to investigate the effect on the anastomotic quality [25].

Based on previous studies, we designed two types of electrodes and analyzed the influence of the electrode structure on the anastomotic quality. To explore the effect of electrode structure on welding quality, mechanical simulation was initially used to verify the mechanical properties of all electrodes. Then, various temperatures and thermal damages were calculated through electrothermal simulation.

II. Materials and methods

Mechanical structure design

In this study, magnesium alloy was selected as the material of welding electrodes (negative electrode). Magnesium alloy has high biocompatibility and is biodegradable in vivo. Excessive magnesium produced by degradation can be eliminated through the excretion system without metal aggregation, which is conducive to the formation of an intestinal anastomosis free of foreign bodies.

The working process of the novel electrodes is displayed in **Figure 1**. Magnesium alloy electrode is placed in the intestine as a negative electrode which can degrade in the intestine. Two separate segments of intestinal tissue were overlapped in the order of "mucosa-serosa". Then, a copper electrode consisting of three identical discrete copper electrodes, each spanning at an angle of 120 degrees (**Figure 1**, left), was placed above the anastomotic area as positive electrode. RF energy was applied to

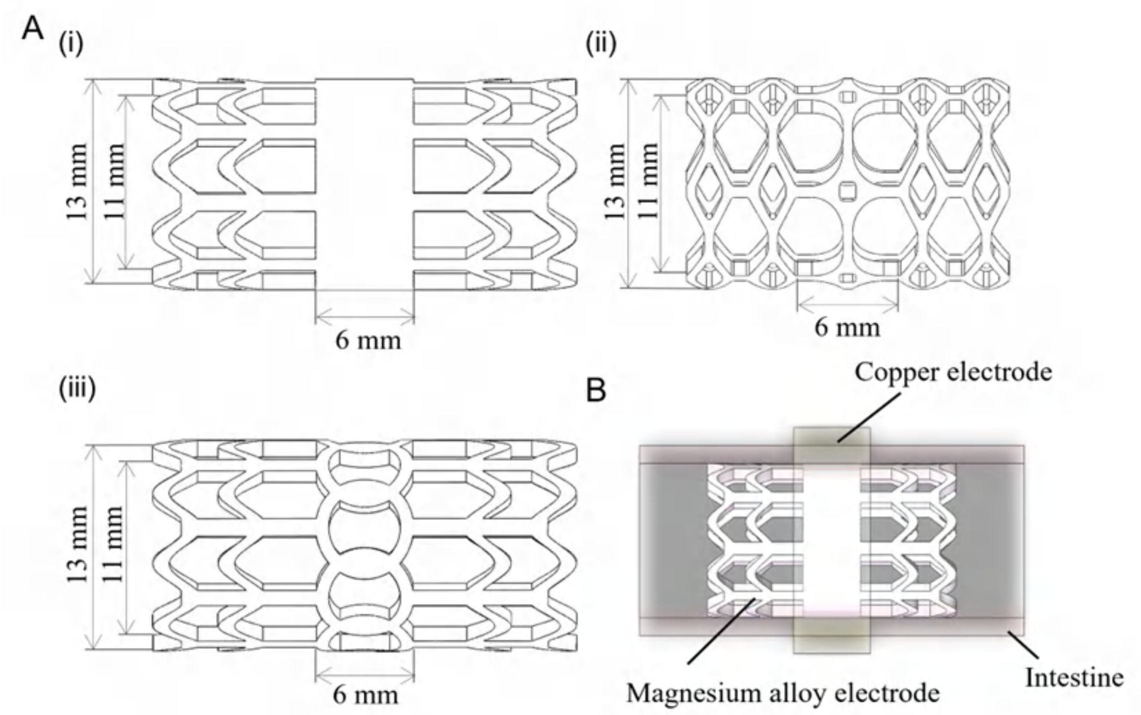

Figure 2. Designed electrode structures and simulation model of control group. (A) Structures of control electrode (i), SA electrode (ii) and C electrode (iii); (B) Simulation model of control group. SA, square and arched; C, circle.

complete the welding. The positive electrode was removed after welding, and the negative electrode could degrade in the intestine.

The welding quality can be affected by the electrode structure of the welding area. Therefore, the differences of electrodes mainly lie in the welding area. During structural design, effective welding area, the contact area between the electrode and intestine in the welding area, and continuous symmetrical structure were considered. SOLIDWORKS 2022 software was used for the design of the mechanical structure. The three designed electrodes are shown in **Figure 2A**. An electrode with a smooth surface in the welding area was used as a control electrode, with an effective welding area of 245.04 mm^2. Additionally, we designed two electrodes: one is the circle (C) electrode whose welding part is composed of successive rings; the other is the square and arched (SA) electrode whose welding part is formed of the continuous pattern with square inside and surrounded by four C arcs. The effective welding areas of these two electrodes are 136.21 mm^2 and 96.27 mm^2, respectively. Besides, for all electrodes, the inner diameter is 11 mm, and the outer diameter is 13 mm. Width of the welding area is 6 mm. The structure of both electrodes can be referred to the control electrode.

Taking the control electrode as an example, the assembly drawing is shown in **Figure 2B**, and the same structure was used for the copper electrodes in the tissue fusion with the three electrodes.

Finite element analysis

Mechanical simulation

Construction of model

Mechanical properties alter due to the difference of electrode structure. Therefore, static structural module of ANSYS Workbench software was used to analyze the stress and strain of the three electrodes under pressure. Tetrahedron mesh was applied in this simulation. Element size was set to 0.5 mm. The material parameters in the simulation are shown in **Table 1**.

Boundary conditions

Both ends of the intestine were fixed. According to our previous studies, a force of 20 N was applied through the positive electrode, which was converted to a pressure of 0.125 MPa in the simulation [26]. The contact interaction between the electrode and the intestine was seen as friction, with a friction coefficient of 0.1.

Electrothermal simulation

Table 1. Mechanical parameters

Project	Density (kg/m^3)	Young's modulus (Pa)	Poisson's ratio
Copper	8960	1.25e11	0.345
Magnesium alloy	1770	4.2e10	0.35
Intestine	1030	1.6e6	0.493

Table 2. Electrothermal parameter

Project	Density (kg/m^3)	Electrical conductivity (S/m)	Thermal conductivity (W/(m·K))	Thermal capacity (J/(kg·K))	Relative dielectric constant (1)
Magnesium alloy	1770	6.417e6	105.224	1e3	1
Copper	8960	5.998e7	400	385	1
Intestine	1030	0.07	0.493	3.595e3	8.98e3

Construction of model

The trend of temperature variation and distribution as well as the thermal damage were analyzed by alternating current/direct current (AC/DC) module and heat transfer module of COMSOL5.6. One-third of each electrode model was applied to the electrothermal simulation because of the symmetry of electrode structure. Specific thermodynamic parameters of the material in simulation are shown in **Table 2** [27-29]. Free Tetrahedral meshes were applied in the simulation. The quantity of meshes of the control electrode, C electrode and SA electrode were 38143, 46264, and 390151, respectively.

Governing equations

The viscoelastic properties of intestinal tissue were calculated by the Maxwell model expressed in equation 1,

$$\dot{\varepsilon} = \frac{\dot{\sigma}}{E} + \frac{\sigma}{\eta} \quad (1)$$

where ε is strain, σ is stress, E is elastic modulus, and η is viscosity coefficient [30].

The thermoelectric coupling problem followed the Pennes biological heat transfer equation 2,

$$\rho c \frac{\partial T}{\partial t} + \nabla \cdot (k \nabla T) + \rho_b c_b \omega (T_b - T) + Q \quad (2)$$

where ρ represents density, c represents specific heat, k represents thermal conductivity, T represents temperature, represents arterial temperature, represents blood density, represents blood specific heat, represents blood perfusion rate, and Q represents power absorption [31].

Tissue thermal damage was calculated using the Arrhenius equation expressed in equation 3,

$$\Omega(\tau) = \int_0^{\tau} A e^{-\frac{E_a}{RT}} dt \quad (3)$$

where denotes the degree of tissue injury, denotes heating time, A denotes frequency factor, and denotes activation energy [32].

Boundary conditions

RF power was converted to the corresponding root mean square value of the DC voltage to enhance the convergence of the finite element model. The energy input to the positive electrode was 110 V AC, while that to the magnesium alloy electrode was set to 0. Domain point probes were added to detect temperature changes, and boundary probes were added to observe thermal damage in the intestine. The time of simulation was 8 s. At t=0, the initial tissue temperature was set to 37 °C, and the environment temperature was set to 25 °C.

III. Results

Mechanical simulation

Nephograms of the designed electrodes are presented in **Figure 3**. The maximum stresses of the control electrode, C electrode and SA electrode were 1.22 MPa, 6.69 MPa and 3.09 MPa, respectively. The maximum stresses of all three electrodes were much less than the yield strength (175 MPa) of magnesium alloy. The maximum strain of C electrode was 0.00016, which is negligible.

Electrothermal simulation

Only part of each electrode was applied to the electrothermal simulation because of the symmetry structure of electrode. The surface diagrams of the temperature at the 8th second for each electrode model are presented in **Figure 4**. The highest temperature of control electrode, C electrode, and SA electrode were 100 ℃, 106 ℃ and 99.6 ℃, respectively.

In order to analyze the temperature variation of the welding area more specifically, the mean

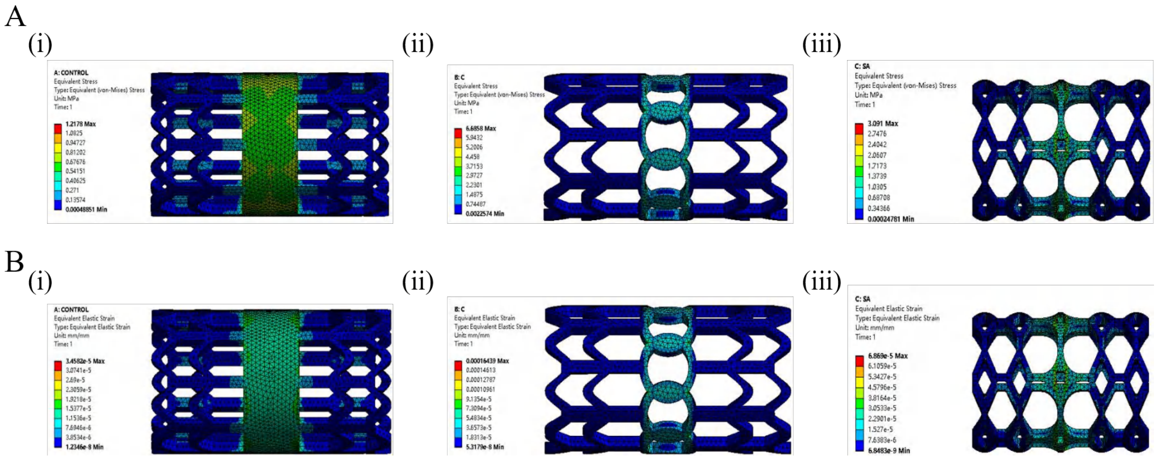

Figure 3. Nephograms of mechanical simulation of the three electrodes. (A) Stress nephogram of control electrode (i), C electrode (ii) and SA electrode (iii). (B) Strain nephogram of control electrode (i), C electrode (ii) and SA electrode (iii). C, circle; SA, square and arched.

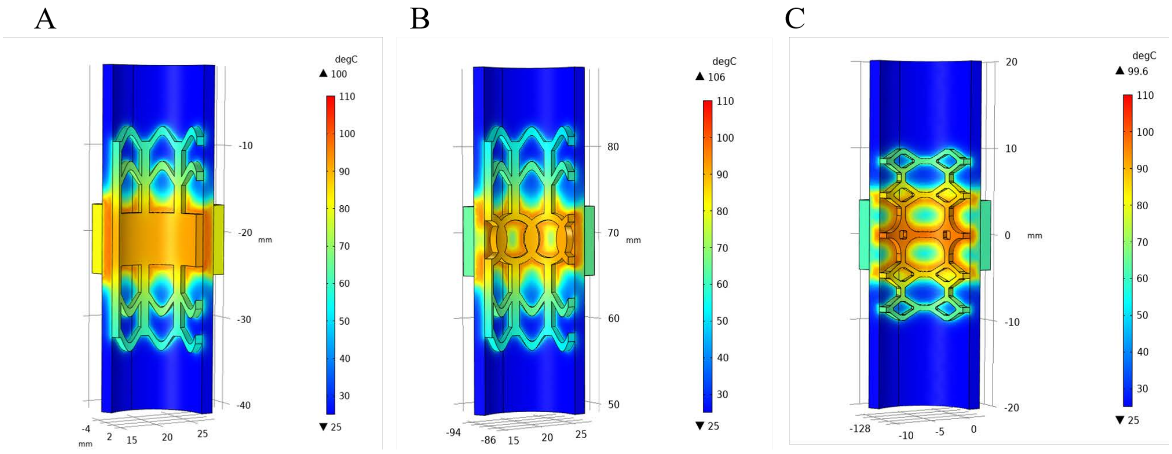

Figure 4. Temperature distributions in the three electrode models. (A) Control electrode; (B) C electrode; (C) SA electrode. C, circle; SA, square and arched.

temperature variation in the intestine for all electrode models is shown in **Figure 5B**. From the 4th second, the mean temperature growth rate at the welding site of intestine in all three electrode models increased significantly. The mean temperature of the control electrode model was the highest and that of C electrode model was the lowest.

Two points in the intestine were specifically selected to insert temperature probes to detect the temperature variation of intestine during the process of welding, which are shown in **Figure 5A**. The mean temperature variations of point a and point b in the intestine are shown in **Figure 5C**. The temperature at point a of the control electrode was the highest and that of C electrode was the lowest. Point b of the three electrode models had the same result. The temperature of point a and b was the same for control electrode, while the temperature of point b was higher than that of point a for C electrode and SA electrode.

In addition, tissue necrosis is one of the important factors to measure the anastomosis effect. As shown in **Figure 6A**, the tissues welded by the control electrode, C electrode, and SA electrode were completely necrotic within an axial distance of 2.546 mm, 2.079 mm, and 1.835 mm from the edge of the welding area, respectively. More tissue survived in the welding area of SA electrode than the other two electrodes. **Figure 6B** shows the proportion of necrotic tissue in all three electrode models. The proportion of necrotic tissue was the highest in the control electrode model and lowest in the SA electrode model. Furthermore, the proportion of necrotic tissue of all electrode models increased sharply from the 4th second.

IV. Discussion

Intestinal reconstruction is an important step in intestinal surgery, which is one of the cornerstones of visceral surgery and is not expected to be overcome or replaced by other treatments soon [33]. Traditional anastomosis includes

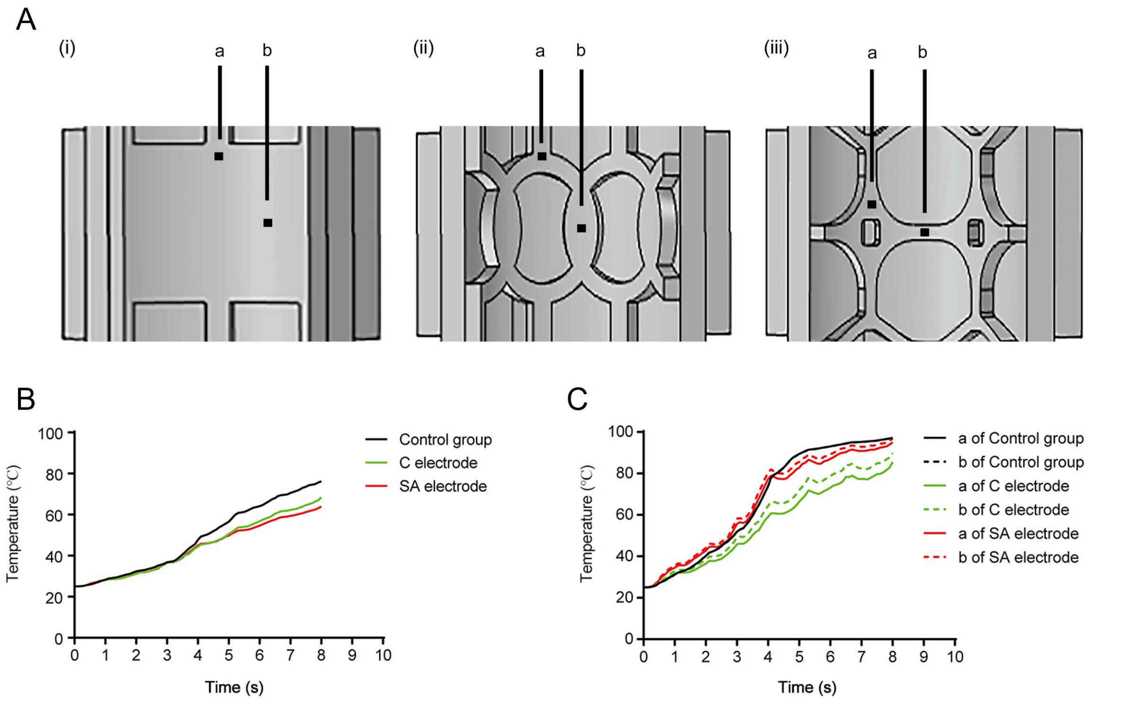

Figure 5. Mean temperature variation at welding site of intestine in all electrode models. (A) Domain point positions at intestine of the control electrode (i), C electrode (ii) and SA electrode (iii); (B) Mean temperature variation at the welding site of intestine in all three electrode models; (C) Temperature variation of probes at intestine in all three electrode models. C, circle; SA, square and arched.

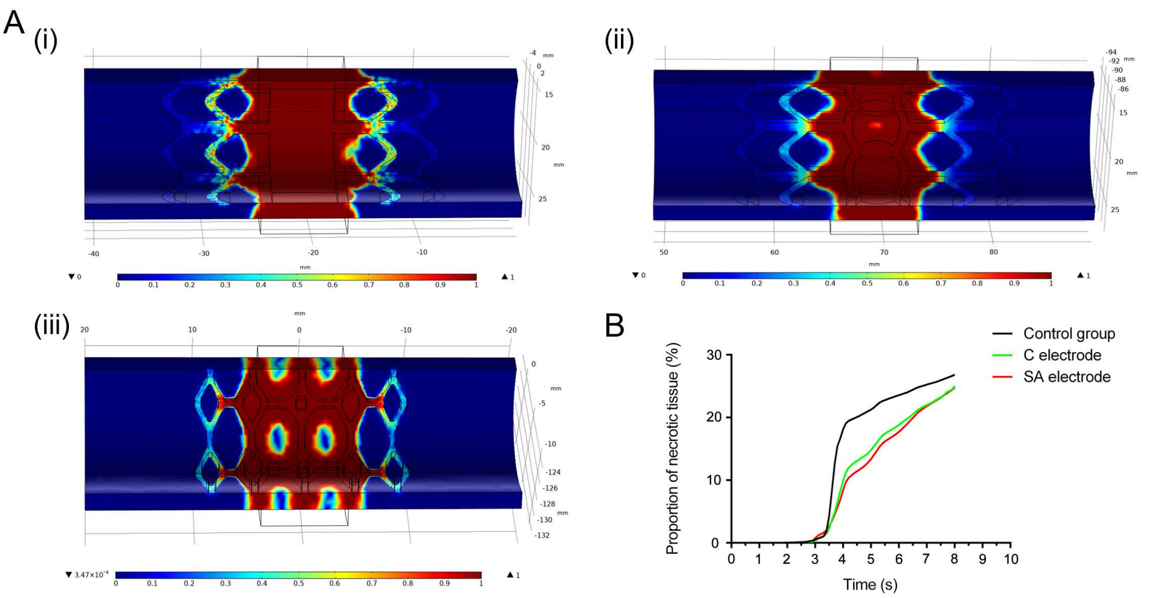

Figure 6. Tissue necrosis in the three electrode models. (A) Nephogram of proportion of necrotic tissue of Control group (i), C electrode (ii) and SA electrode (iii) at the 8th second; (B) Proportion of necrotic tissue. C, circle; SA, square and arched.

suturing and stapling. The former is not suitable for minimally invasive surgery, and the latter may cause inflammation and infection, which is not conducive to anastomosis healing. Therefore, energy tissue fusion technology has emerged for intestine anastomosis.

However, intestinal leakage has always been a challenge after thermal anastomosis. Pressure, welding time, and temperature during welding are important factors that affect the anastomosis effect. In previous studies, pressure, welding time, and other experimental parameters were explored to enhance the burst pressure and reduce thermal damage [21, 25]. Ritcher et al. studied the effects of 4 different electrodes on vascular closure with RF energy, which indicated the importance role of electrode structure in tissue welding [34]. However, there are still few reports to date on RF tissue welding technology from the perspective of electrode structure [24]. Therefore, in this study, we aimed to investigate the effect of different electrode structure on welding quality to fill in the research gap in this respect. Previous studies of our team did lots of experiments in vivo and obtained optimized parameters of pressure and welding time, which were applied into simulations in the models [26]. C electrode and SA electrode were designed to reduce the thermal damage in the welding area, enhance the thermal diffusion ability, and improve the healing ability of the intestinal tissue. In fact, changing the electrode structure of welding area to decrease effective welding area can reduce necrotic tissues and improve heat dissipation capacity.

The maximum stress (6.69 MPa) of the C electrode was the largest in all electrodes, which was much less than the yield strength (175 MPa) of magnesium alloy. Besides, the maximum strain of the C electrode, 0.00016, was much less than 1%. Therefore, the mechanical properties of the SA electrode are better than that of the C electrode, but the mechanical properties of all electrodes are acceptable. Of course, excessive pressure will affect the intestinal tissue and reduce the quality of the anastomotic stoma.

The highest temperature of the C electrode was 6 ℃, higher than that of the control electrode. This is due to the hollow structure, which reduces effective welding area, thus increases the local current density. The highest temperature of the SA electrode (99.6 ℃) was similar to that of the control electrode (100 ℃). The effective welding area (96.27 mm^2) of the SA electrode was about 39.29% of the effective welding area of the control. The effective welding area (136.21 mm^2) of the C electrode was about 55.59% of that of the control. That is to say, the hollow area is large enough, so the heat dissipation rate of the SA electrode is faster than the C electrode. These results correspond to the mean temperature variation at the intestine of the welding area in three electrode models. The mean temperature of the SA electrode was the lowest and that of control electrode was the highest due to the hollow structure.

The mean temperature was calculated to analyze the whole temperature variation of intestine in the welding area. Therefore, temperature probes were inserted into two different points of intestine in the welding area. When the input energy was constant, a larger proportion of effective area led to higher temperatures in the entry part. Point a is close to the hollow part and point b is at the connection of electrode symmetric structures in the welding area. In consequence, the temperature of point b of the two novel electrodes were higher than that of point a. Besides, as getting closer to the electrode entity, there is more necrotic tissue in the welding area. Therefore, the rate of tissue necrosis in the SA electrode model was the lowest compared with the other two electrode models.

V. Conclusion

Two novel electrodes (C and SA electrodes) were designed in this study to investigate the effects of electrode structure on RF tissue welding. Finite element analysis was used to analyze the mechanical property of designed electrodes and thermal damage to tissue, which are important indices to evaluate the welding quality. The results of simulations show that the SA electrode is better than the C electrode, and also provide a strong support for facilitating RF tissue welding technology by optimizing electrode structures. Even so, further in vitro and in vivo experiments are required to ensure the feasibility and safety of this technology.

References

[1] Hyuna S, Jacques F, L. SR, et al. Global Cancer Statistics 2020: GLOBOCAN Estimates of Incidence and Mortality Worldwide for 36 Cancers in 185 Countries. CA Cancer J Clin 2021;71:209-249.

[2] Esmeeta A, Adhikary S, Dharshnaa V, et al. Plant-derived bioactive compounds in colon cancer treatment: An updated review. Biomed Pharmacother 2022;153:113384.

[3] Grass F, Behm KT, Duchalais E, et al. Impact of delay to surgery on survival in stage I-III colon cancer. Eur J Surg Oncol 2020;46:455-461.

[4] Broex ECJ, Asselt ADIv, Bruggeman CA, et al. Surgical site infections: how high are the costs? J Clin Med 2022;11:6991.

[5] Kolasiński W. Surgical site infections–review of current knowledge, methods of prevention. Pol J Surg 2019;91:41-47.

[6] Schoetz Jr DJ, Roberts PL, Murray JJ, et al. Addition of parenteral cefoxitin to regimen of oral antibiotics for elective colorectal operations. A randomized prospective study. Ann Surg 1990;212:209-212.

[7] Biondo S, Kreisler E, Fraccalvieri D, et al. Risk factors for surgical site infection after elective resection for rectal cancer. A multivariate analysis on 2131 patients. Colorectal Dis 2012;14:e95-e102.

[8] Smith RL, Bohl JK, McElearney ST, et al. Wound infection after elective colorectal resection. Ann Surg 2004;239:599-607.

[9] Xu Z, Qu H, Kanani G, et al. Update on risk factors of surgical site infection in colorectal cancer: a systematic review and meta-analysis. Int J Colorectal Dis 2020;35:2147-2156.

[10] Holmer C, Winter H, Kroger M, et al. Bipolar radiofrequency-induced thermofusion of intestinal anastomoses--feasibility of a new anastomosis technique in porcine and rat colon. Langenbecks Arch Surg 2011;396:529-533.

[11] Hyman NH. Managing anastomotic leaks from intestinal anastomoses. Surgeon 2009;7:31-35.

[12] Wu Z, Vakalopoulos K, Kroese L, et al. Reducing anastomotic leakage by reinforcement of colorectal anastomosis with cyanoacrylate glue. Eur Surg Res 2013;50:255-261.

[13] Vakalopoulos KA, Daams F, Wu Z, et al. Tissue adhesives in gastrointestinal anastomosis: a systematic review. J Surg Res 2013;180:290-300.

[14] Giuratrabocchetta S, Rinaldi M, Cuccia F, et al. Protection of intestinal anastomosis with biological glues: an experimental randomized controlled trial. Tech Coloproctol 2011;15:153-158.

[15] Stylianopoulos T, Aksan A, Barocas VH. A structural, kinetic model of soft tissue thermomechanics. Biophys J 2008;94:717-725.

[16] Wright N, Humphrey J. Denaturation of collagen via heating: an irreversible rate process. Annu Rev Biomed Eng 2002;4:109-128.

[17] Kramer EA, Rentschler ME. Energy-based tissue fusion for sutureless closure: applications, mechanisms, and potential for functional recovery. Annu Rev Biomed Eng 2018;20:1-20.

[18] Smulders J, De Hingh I, Stavast J, et al. Exploring new technologies to facilitate laparoscopic surgery: creating intestinal anastomoses without sutures or staples, using a radio-frequency-energy-driven bipolar fusion device. Surg Endosc 2007;21:2105-2109.

[19] Lim CBB, Goldin RD, Elson DS, et al. In vivo thermography during small bowel fusion using radiofrequency energy. Surg Endosc 2010;24:2465-2474.

[20] Salameh JR, Schwartz JH, Hildebrandt DA. Can LigaSure seal and divide the small bowel? Am J Surg 2006;191:791-793.

[21] Zhou H, Han S, Chen J, et al. A feasibility study of closing the small bowel with high-frequency welding device. J Biomed Eng 2014;31:1332-1335.

[22] Winter H, Holmer C, Buhr HJ, et al. Pilot study of bipolar radiofrequency-induced anastomotic thermofusion–exploration of therapy parameters ex vivo. Int J Colorectal Dis 2010;25:129-133.

[23] Zhao L, Zhuo C, Song C, et al. Histological characteristics of collagen denaturation and injuries in bipolar radiofrequency-induced colonic anastomoses. Pathol Res Pract 2015;211:214-218.

[24] Zhao L, Song C, Wang Z, et al. Novel concave–convex electrode for colonic anastomoses by radiofrequency thermo-fusion. Surg Endosc 2015;29:1809-1816.

[25] Tu L, Zhou Y, Song C, et al. Preliminary study of a control algorithm for radio-frequency-induced intestinal tissue fusion. Int J Hyperthermia 2019;36:1296-1305.

[26] Xing XP, Song CL. A novel electrode to achieve balance between anastomotic strength and tissue thermal damage for radiofrequency-induced intestinal anastomosis (Advance online publication). Acta Bioeng Biomech 2023;25(3).

[27] Dodde R, Bull J, Shih A. Bioimpedance of soft tissue under compression. Physiol Meas 2012;33:1095.

[28] Dodde RE, Miller SF, Geiger JD, et al. Thermal-electric finite element analysis and experimental validation of bipolar electrosurgical cautery. J Manuf Sci Eng 2008;130:021015.

[29] Trujillo M, Berjano E. Review of the mathematical functions used to model the temperature dependence of electrical and thermal conductivities of biological tissue in radiofrequency ablation. Int J Hyperthermia 2013;29:590-597.

[30] Zhang C, Liu H, Tan R, et al. Interaction model between capsule robot and intestine based on nonlinear viscoelasticity. Proc Inst Mech Eng H 2014;228:287-296.

[31] Pennes HH. Analysis of tissue and arterial blood temperatures in the resting human forearm. J Appl Physiol 1948;1:93-122.

[32] Pearce JA. Comparative analysis of mathematical models of cell death and thermal damage processes. Int J Hyperthermia 2013;29:262-280.

[33] Rosendorf J, Klicova M, Herrmann I, et al. Intestinal anastomotic healing: what do we know about processes behind anastomotic complications. Front Surg 2022;9:904810.

[34] Richter S, Kollmar O, Schilling M, et al. Efficacy and quality of vessel sealing: comparison of a reusable with a disposable device and effects of clamp surface geometry and structure. Surg Endosc 2006;20:890-894.

Progress in Medical Devices
eISSN: 2957-5478

Research Article https://doi.org/10.61189/061485jysfwu

Impact of tissue-electrode contact force on irreversible electroporation for atrial fibrillation in potato models

Tiantian Hu, Yingfan Yuan, Mengying Zhan, Binyu Wang, Lin Mao, Yu Zhou

School of Health Science and Engineering, University of Shanghai for Science and Technology, Shanghai 200093, China.

Corresponding author: Yu Zhou.

Acknowledgements: This work was financially supported by National Natural Science Foundation of China (51901137).

Declaration of conflict of interest: None.

Received August 22, 2023; Accepted November 28, 2023; Published December 31, 2023

Highlights

- A strong positive correlation was identified in the investigation of the relationship between contact force and irreversible electroporation (IRE) efficacy for tissue ablation.
- This research conducted on potato models highlights the importance of optimizing electrode contact force in IRE for applications in atrial fibrillation treatment.
- Our findings provide insights into the design of advanced IRE ablation protocols and facilitate the clinical development and translation of this technology for effective atrial fibrillation treatment.

Abstract

Background: Irreversible electroporation (IRE) is an emerging tissue ablation technique that offers advantages over traditional catheter ablation, such as minimal thermal damage and reduced treatment time. However, as this technique also involves delivering energy through a catheter to target tissue, there are still challenges regarding the contact between the catheter and the targeted tissue, and there is a lack of relevant studies. In this study, we examined this issue using potato models with three groups of experiments. **Methods:** First, the relationship between the effect of biphasic and monophasic output modes and contact force (CF) was studied. Next, the effect of different voltages on biphasic output mode was examined. Finally, impedance analysis was conducted to test the contact impedance under different CFs. **Results:** The IRE ablation efficacy increased with the increase of CF in both monophasic and biphasic output modes, and there was a strong correlation between the ablation efficacy and the CF. In addition, at three voltage levels, the IRE ablation efficacy increased with increasing CF, and there was a strong correlation between the ablation efficacy and the CF. **Conclusion:** The results indicate that, under common IRE electrical parameter configuration, the effect of IRE on the tissue has a positive response to the CF of the electrode in the potato model. This finding has important implications for the design of electrodes used in IRE for the treatment of atrial fibrillation.

Keywords: Irreversible electroporation ablation, tissue-electrode contact force, atrial fibrillation, catheter ablation, potato

Introduction

Atrial fibrillation (AF) is a prevalent cardiac arrhythmia, affecting up to 4% of the global population. While the incidence of AF in individuals under 40 is very low (less than 1%), it drastically elevates with the increase of age, affecting 17% of individuals over 80 years old [1]. This escalating prevalence in older individuals poses a significant challenge to the extension of life expectancy globally. AF not only significantly impacts the body's functioning but also leads to emotional distress and reduced quality of life [2]. It is estimated that by 2050, there will be 6-12 million individuals with AF worldwide, with an estimated 17.9 million people in Europe alone affected by this disease by 2060 [3, 4].

The management of AF involves anticoagulation, rhythm control, and heart rate control

Address correspondence to: Yu Zhou, School of Health Science and Engineering, University of Shanghai for Science and Technology, NO.516 Jungong Road, Shanghai 200093, China. Tel: 18021042556, E-mail: zhouyu@usst.edu.cn.

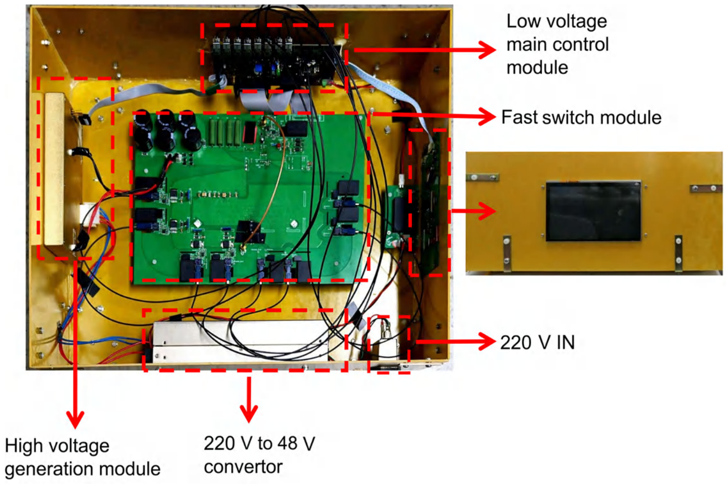

Figure 1. Laboratory prototype pulse generator and its components.

through various means. The most commonly used strategies include medical therapy and catheter ablation [5, 6]. Additionally, lifestyle modifications can also aid in AF management and reduce its incidence [7]. Radiofrequency ablation and Cryoballoon ablation are the main clinical catheter ablation methods for AF. However, both of these catheter ablation techniques rely on temperature transmission, leading to three practical problems. The first problem arises due to blood flow in the target area, causing a heat sink effect that can result in incomplete treatment. The second issue is non-selective killing of cells due to high or low temperature during treatment, which may cause unnecessary thermal damage to tissues adjacent to the target area [8, 9]. Lastly, the treatment efficacy depends on the contact force (CF) between electrode and tissue, leading to incomplete treatment due to the contact problem [9, 10]. Owing to these issues, there is an urgent need for a clinical novel therapeutic modality.

The irreversible electroporation (IRE) causes nanometer-sized irreversible micropores on the cell membrane under the influence of a high-voltage electric field. The presence of these micropores leads a loss of cell homeostasis resulting in cell death. This is the principle behind IRE tissue ablation. This technique was initially used in the industrial and food sectors [11-13], and was later introduced into tumor ablation therapy, where it proved its non-thermal properties and safety. It is now being applied in AF ablation therapy [14-16]. Compared to other catheter ablation techniques, IRE ablation has less thermal damage to surrounding tissues and selectively kills cardiomyocytes [17, 18].

Like radiofrequency ablation and Cryoballoon ablation, IRE ablation also delivers energy to the target tissue via a catheter. Therefore, achieving proper CF remains a challenge [19, 20]. However, the relationship between CF and IRE ablation efficacy is not explicit, and there are few relevant studies [21, 22]. Therefore, further in-depth research is warranted to understand the correlation.

The concept of CF in the field of robotic surgery is a significant and common topic, and the research methods employed in this area hold substantial reference value for this study [23-25]. The aim of this study is to investigate the relationship between CF and IRE ablation efficacy in a potato model and to provide insights into catheter design for IRE ablation of AF. Potato model is a commonly used plant model in IRE ablation experiments due to its capacity for visually representing the effects of IRE ablation. It also offers practical advantages, such as easy access to experimental materials and the absence of ethical concerns [26-28]. This study utilized potato model and initially examined the relationship between CF and the IRE ablation efficacy under both biphasic and monophasic pulse sequences, and then changed the amplitude to evaluate the response of efficacy and CF.

Material and methods

Laboratory prototype pulse generator and its output waveform

The high-voltage pulse generator used in this experiment is a laboratory prototype pulse generator (University of Shanghai for Science and Technology, China). The circuit design is based on the H-bridge biphasic pulse generator using MOSFETs (G3R30MT12J, GeneSiC Inc., USA) with the ability to withstand 1200 V. The generator can output monophasic and biphasic pulses up to 2000 V with a pulse repetition rate of up to 800 Hz. The duration of the output pulse is about 800 ns, providing a waveform output that meets the experimental requirements. The generator comprises a human-computer interface, a high-voltage generation module, an alternating current to direct current module, a fast-switch module, and a low-voltage control module, as illustrated in **Figure 1**.

In the first experiment, we delivered two IRE pulse sequences: a monophasic pulse sequence and a biphasic pulse sequence, as illustrated in **Figure 2**. The monophasic pulse

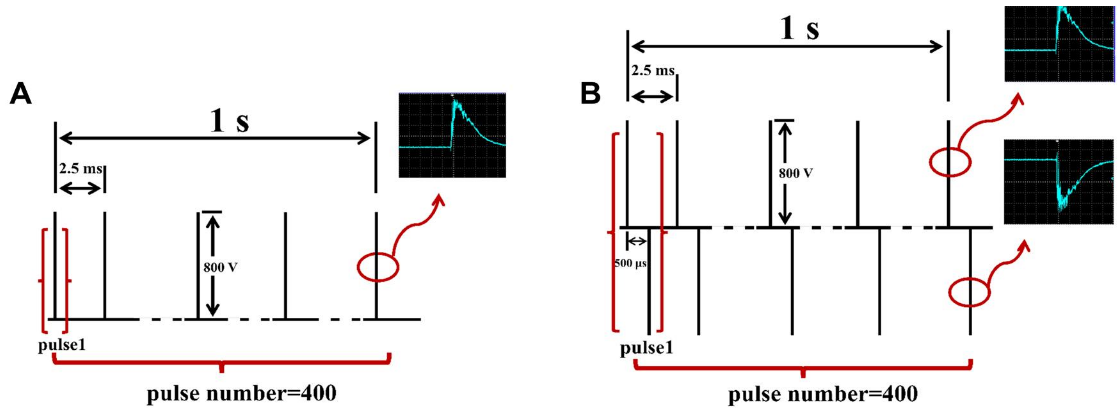

Figure 2. Two representative types of output waveform for the pulse generator. (A) Representative biphasic pulse; (B) Representative monophasic pulse.

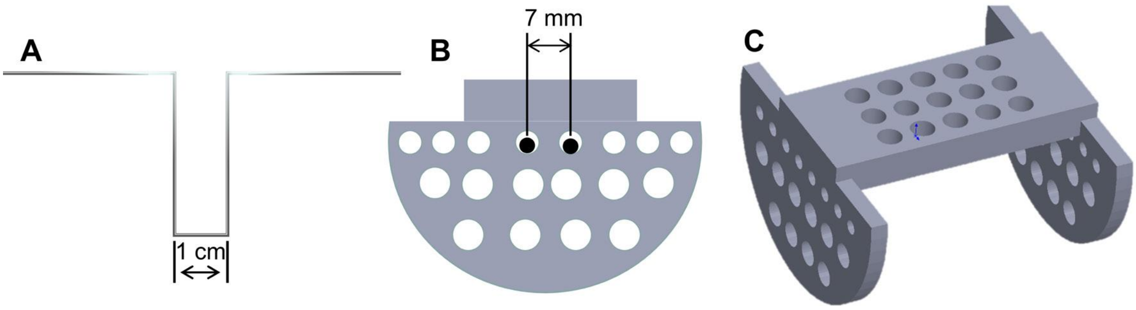

Figure 3. Design schematic of the electrode and its clamp. (A) Front view of the electrode; (B) Side view of the electrode clamp; (C) 3D design schematic of the electrode clamp.

sequence consisted of 3,000 monophasic pulses, with an amplitude of 800 V, a pulse width of 800 ns, and a repetition rate of 400 Hz (**Figure 2A**). The biphasic pulse sequence comprised 3000 biphasic pulses, with an amplitude of 800 V, a pulse width of 800 ns, a repetition rate of 400 Hz, and a biphasic interval of 500 μs (**Figure 2B**). To investigate the relationship between CF and IRE ablation at different voltages, we conducted experiments with 800 biphasic pulses, using amplitudes of 350 V, 500 V, and 800 V, a pulse duration of 800 ns, a repetition rate of 400 Hz, and a biphasic interval of 500 μs.

Electrode design and its clamp

Due to the presence of inherent variability in each potato model and the potential induction of artificial errors during processing, the resultant effect plane of the models cannot remain entirely parallel to the electrode plane, thereby causing an incongruity in the contact area between the electrode and the divergent model surfaces of multiple potatoes. To mitigate this inconsistency, we shortened the length of the contact part between the electrode and the potato model. This approach lessens the dependency of the experimental results on the parallel relationship between the potato models' action surface and the electrode plane.

The electrode, as shown in **Figure 3A**, is made of 304 stainless steel with a convex pattern that allows only partial of the electrode to contact with the potato model during pulse delivery. The diameter of the electrode is 0.7 mm. The length of the contact area between the electrode and the potato model was set to be 1 cm.

The electrode clamp used in this experiment was a white PLA 3D printed model. It is equipped with holes of different sizes on the side to accommodate fixed electrodes of varying sizes and allow for adjustment of the distance between two electrodes as required, which is set at 0.7 cm in this study, as presented in **Figures 3B and C**. The clamps are secured in place using screws and can be mounted onto a lifting platform.

Process of the potato models and assessment of the efficacy

Potatoes have been used as a common plant

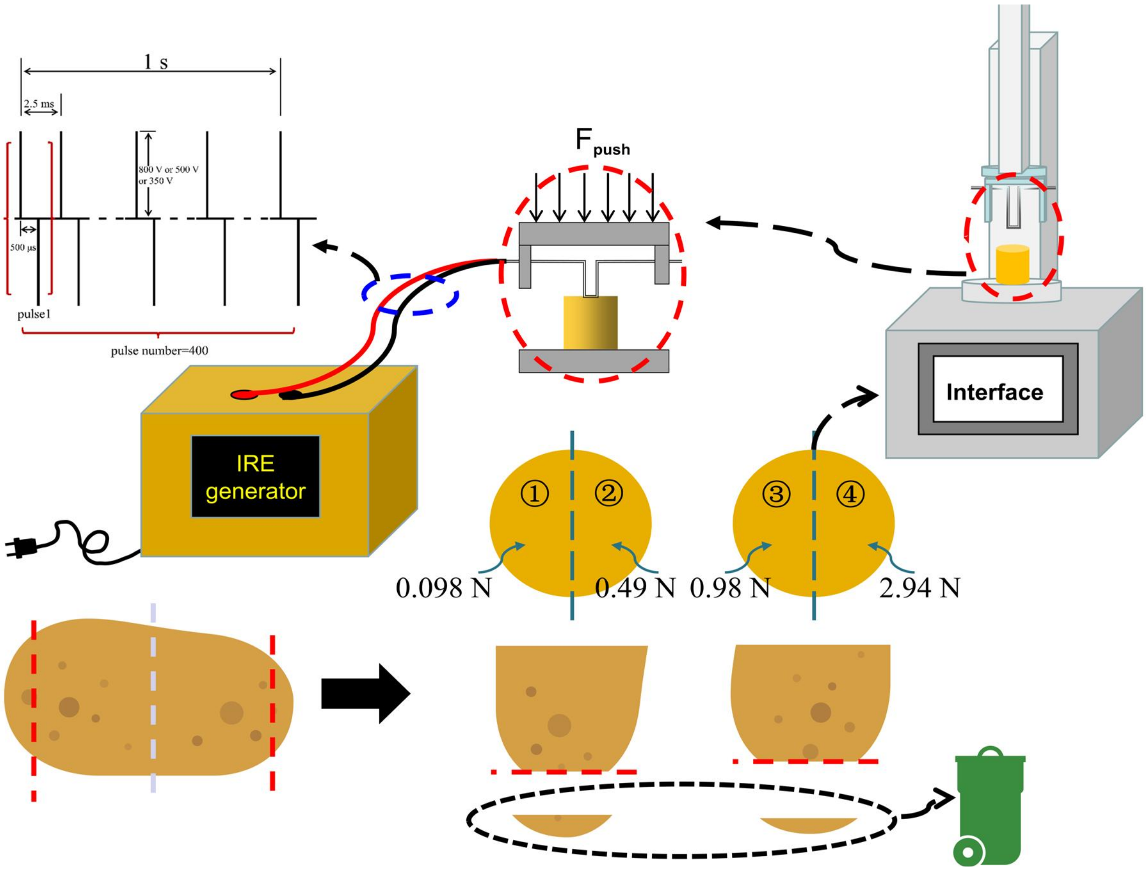

Figure 4. Schematic diagram of potato processing method and experimental steps. IRE, irreversible electroporation.

model in IRE experiments to verify the efficacy of pulses, evaluate the efficacy of novel electrodes, and measure the superiority of pulse sequences [26-28]. Due to the advantages of low cost, easy evaluation of results, and no ethical issues, it is widely used in IRE research [26-28]. Typically, black areas of melanin accumulation arising from intracellular polyphenol oxidation can only be observed in the potato model 12 to 48 h after the experiment is conducted. The results are evaluated using comparisons among the black metrics under various parameters, which is a convenient, fast, and economical method for hypotheses testing [26]. Other evaluation methods, such as MRI scan and TTC staining, are also available [26, 29].

In this experiment, we employed direct observation to assess the validity of the experimental results. To ensure the experiment's validity and eliminate the interference of factors such as individual variability and tissue uniformity, a potato model is cut into 2 pieces. Each piece is divided into 2 regions. And on each region, we applied different CF with the same pulse. The potato processing method and experimental procedure are presented in **Figure 4**. The potatoes used in this experiment were procured from a nearby supermarket (RT-Mart, China) and utilized within 4 h of procurement. To observe the output waveform, an oscilloscope (AFG3022B, Tektronix Inc., USA) was used in all experiments. Impedance was detected using an impedance analyzer (IM3570, Hioki Inc., Japan).

Pressure control lifting platform

To regulate the CF output, a pressure-controlled lifting platform, manufactured in our laboratory, was employed in this study. This platform comprises a motor-driven arm, a control module, and a human-computer interface, as illustrated in **Figure 5**. Using PID control outputs, the device could output various pressures up to 70 N, while pressure data were sampled using the AD5933 (Analog Inc., USA). In the experiment, we set the CF to 0.098 N (10 g), 0.49 N (50 g), 0.98 N (100 g), and 2.94 N (300 g), respectively, with G taking a value of 9.8 m/s^2.

Overview of experimental design

The study comprised three experiments, using a total of 55 potato models. The first experiment (20 potato models) examined the relationship between CF (0.098 N, 0.49 N, 0.98 N, and 2.94 N) and IRE ablation efficacy under

Table 1. ANOVA Test Results for one-way repeated measures under different output modes

Output mode	F	P-value	matching F	Matching P-value
Monophasic	23.75	2e-7***	2.993	2e-3**
Biphasic	22.94	2e-9***	13.05	1e-10***

Note: **P<0.01, ***P<0.001.

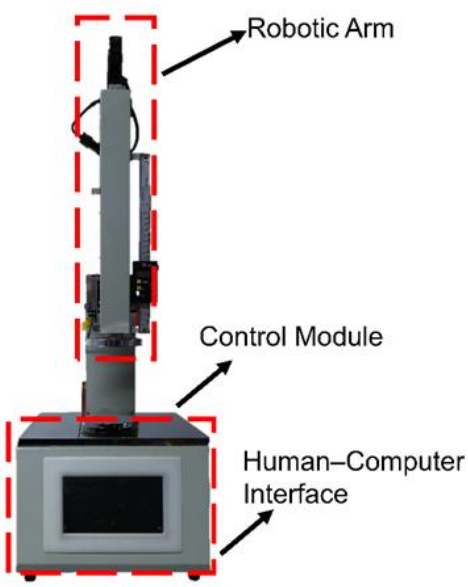

Figure 5. Pressure control lifting platform and its components.

both monophasic and biphasic pulse sequences at the same voltage amplitude. The second experiment (30 potato models) assessed the relationship between CF and IRE ablation efficacy with different output voltage amplitudes (350 V/500 V/800 V). A reference group was set, which was subjected only to CF without pulse (5 potato models). The inclusion of a reference group was intended to exclude mechanical damage caused by the electrode to the potato model and to prevent it from affecting the final experimental results. Prior to commencing with this experiment, a biphasic pulse output mode was confirmed with CF set at 0.098 N, 0.49 N, 0.98 N, and 2.94 N. Finally, 15 potato models were selected from the above experiments to determine the relationship between the impedance and different CF by gradually increasing the CF under the observation of the impedance analyzer.

Image processing

The potato model was photographed using a camera (Lumix S5, Panasonic Inc., Japan) fixed on a tripod, with a constant distance. The image data was processed using MATLAB 2020 (MathWorks Inc., USA). The processing method involved importing the color image into MATLAB and selecting the reference area (potato model's original color) as the benchmark. The RGB value of the color block of reference region was used to set a threshold value of 100. Pixels were considered to belong to the reference region (non-oxidized region) when the difference between the RGB value of the target region and the benchmark RGB value was within the threshold value. Otherwise, the area was categorized as the action region (oxidized region).

Data and Statistical Analysis

Statistical analysis was performed using SPSS software (IBM Inc., USA). Data were expressed as mean ± standard deviation (SD) unless otherwise stated. Oxidation areas of different regions within the single potato in the same experimental group were compared using one-way repeated measures ANOVA. Post hoc pairwise comparisons were conducted using Tukey test (*P<0.05, **P<0.01, ***P<0.001). Pearson's correlation analysis was used to determine the correlation between CF and ablated area within the same potato.

Results

Relationship between CF and IRE ablation ef-ficacy under monophasic pulse and biphasic pulse

In this experiment, 20 potato models were prepared according to the methodology illustrated in **Figure 4** and were subsequently divided into two groups. Each potato model was subjected to four IRE ablation experiments with varying CFs. While keeping the output electrical parameters constant, different pulse output modes (monophasic and biphasic) were employed in each experimental condition. Following the completion of the experiments, all potato models were left for 24 h under room temperature (20 °C), and their results were recorded by a camera. Moreover, all potato models underwent the same after-treatment procedure following the experiment.

The results of the ANOVA test under different output modes are presented in **Table 1**. It was evident that significant differences existed in the mean effects of various CFs for both output modes. Furthermore, there was a significant difference in matching effects under monopha-

Table 2. Turkey Post-hoc Test Results for every two CF under both output modes

	0.098 N & 0.49 N	0.098 N & 0.98 N	0.098 N & 2.94 N	0.49 N & 0.98 N	0.49 N & 2.94 N	0.98 N & 2.94 N
Monophasic	7e-4***	2e-5***	8e-6***	0.94	4.6e-2*	6e-3**
Biphasic	1.9e-3**	8e-6***	1e-9***	0.29	3e-3**	4.5e-2*

Note: *P<0.05, **P<0.01, ***P<0.001. CF, contact force.

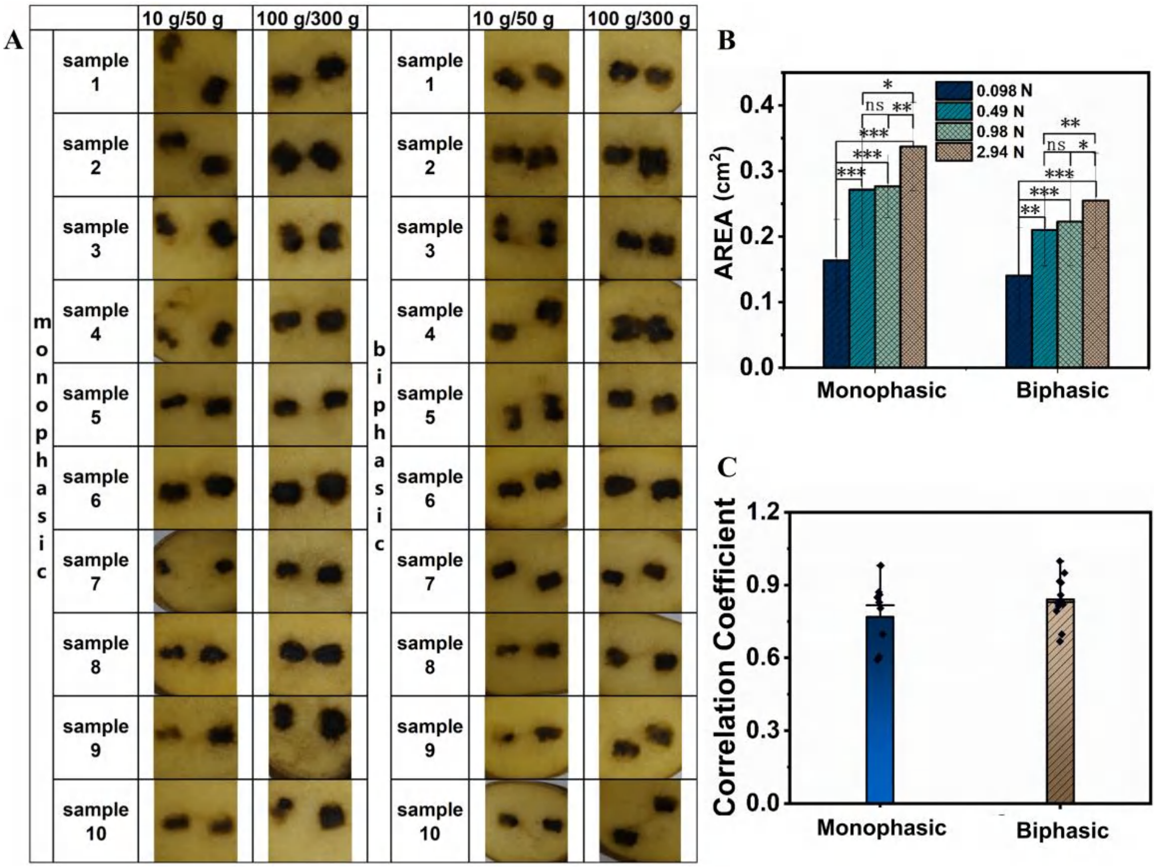

Figure 6. Experimental results and data evaluation in biphasic pulse output mode and monophasic pulse output mode. (A) Experimental results of biphasic and monophasic pulse on potato models; (B) Statistics data showing effect of different output mode on oxidation area under different CFs; (C) Correlation coefficient of CF and oxidation area under different output modes. CF, contact force. *P<0.05, **P<0.01, ***P<0.001; ns represents P>0.05.

sic output and a highly significant difference under biphasic output.

The experimental results of the potato model are shown in **Figure 6A**. After the experiments, surface oxidation areas caused by IRE could be observed on all potato models. **Figure 6B** depicts the relationship between the size of the IRE ablation areas and the CF within the same experimental group. The results of the Turkey post-hoc test are annotated in **Table 2**. It was evident that, regardless of whether monophasic or biphasic modes, there was a highly significant difference in the size of the ablation zone at 0.098 N compared to the other CFs. Under both output modes, there was no significant difference in the size of the ablation zone at 0.49 N and 0.98 N. However, for the 0.49 N and 2.94 N CFs, the size of the ablation zone exhibited an extremely significant difference in the monophasic output mode and a more noticeable difference in the biphasic output mode. Similarly, at the CF of 0.98 N and 2.94 N, there was a highly significant difference in the size of the ablation zone in the monophasic output mode and a significant difference in the biphasic output mode.

Figure 6C illustrates the correlation between CF and IRE ablation areas under both operating modes. The correlation coefficients under both operating modes were greater than 0.5, which implies a robust relationship between the electrode's CF and the ablation effect.

Relationship between CF and IRE ablation with different amplitudes under biphasic pulse

In this experiment, 30 potato models in three groups were ablated using three different

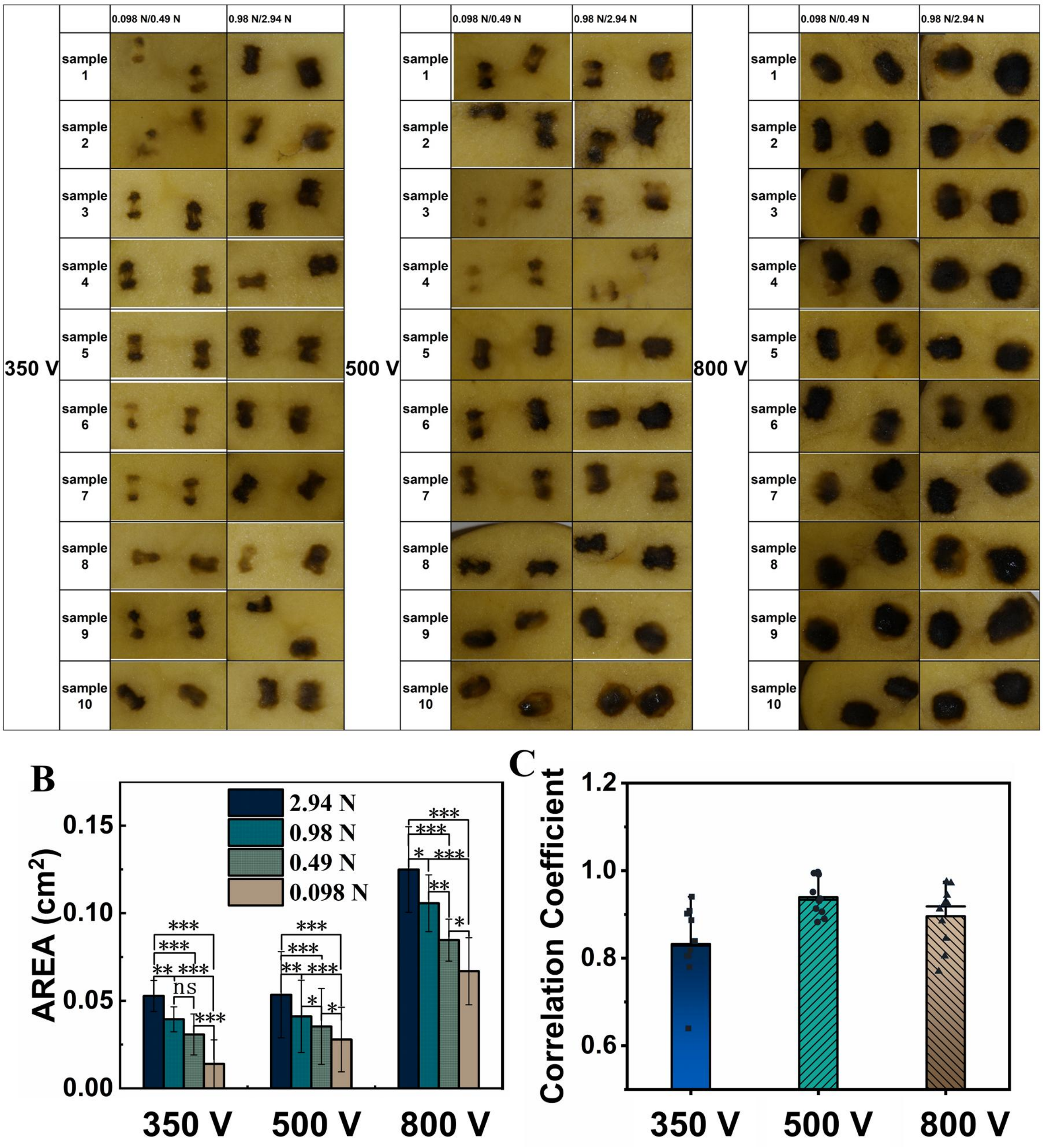

Figure 7. Experimental results and data evaluation in different output amplitudes. (A) Experimental results of the 300V,500V, and 800V groups; (B) Statistics data showing effect of different output amplitudes on oxidation area under different CFs; (C) Correlation coefficient of CF and oxidation area under different output amplitudes. CF, contact force. *P<0.05, **P<0.01, ***P<0.001; ns represents P>0.05.

amplitudes (350 V, 500 V, and 800 V) with the same pulse sequence. IRE ablation experiments were conducted on the cross-sections of each potato model under four different CFs. Subsequently, all potato models were kept at room temperature (20 °C) for 24 h and photographed with a camera. Following the experiment, uniform disposal was performed on all the potato models.

The results of the ANOVA test for different output voltage amplitudes are presented in **Table 3**. It could be observed that, irrespective of the output amplitude, significant differences existed among the various CFs. Furthermore, there was a significant difference in matching effects at a voltage amplitude of 350 V, and a highly significant difference at output voltages of 500 V and 800 V.

The experimental outcomes of the potato model are depicted in **Figure 7A**, which displays visible surface oxidation areas resulting from IRE ablation on all the potato models after the experiment. **Figure 7B** delineates the alteration in the size of IRE ablation areas with respect to CFs applied within the same output voltage. The results of the Turkey post-

Table 3. ANOVA Test Results for one-way Repeated Measures under different output voltages

Output Voltage	F	P-value	matching F	Matching P-value
350 V	35.37	2e-9***	3.074	1.1e-2*
500 V	41.70	3e-10***	54.45	5e-15***
800 V	36.05	1e-9***	4.773	<7e-4***

Note: *P<0.05, ***P<0.001

Table 4. Turkey Post-hoc Test Results for every two CF under three amplitudes

	0.098 N & 0.49 N	0.098 N & 0.98 N	0.098 N & 2.94 N	0.49 N & 0.98 N	0.49 N &2.94 N	0.98 N & 2.94 N
350V	9e-4***	3e-6***	1e-9***	0.138	3e-5***	9e-3**
500V	4.7e-2*	4e-5***	3e-10***	1.3e-2*	4e-8***	2e-4*
800V	2.7e-2*	3e-6***	1e-9***	7e-3**	2e-6***	1.5e-2*

Note: *P<0.05, **P<0.01, ***P<0.001.

hoc test are annotated in **Table 4**. It could be observed that, the oxidation area exhibited a growth trend with increasing CF at the same voltage. At the voltage of 350 V, there was a highly significant difference between 0.098 N and 0.49 N, and a significant difference was also observed at voltages of 500 V and 800 V. At 0.098 N and other two CFs (0.98 N, 2.94 N), all three output voltage amplitudes exhibited significant differences. For the CFs of 0.49 N and 0.98 N, there was no significant difference at 350 V, a significant difference at 500 V, and a more noticeable difference at 800 V. Under the CFs of 0.49 N and 2.94 N, highly significant differences existed for all three output voltage amplitudes. For 0.98 N and 2.94 N CFs, there were noticeable differences at 350 V and 500 V, and a significant difference at 800 V. Moreover, **Figure 7C** reveals the connection between CF and ablation efficacy under varied voltage output conditions. Intriguingly, the correlation coefficients between CF and ablation area were greater than 0.5, indicating a robust relationship between the two variables.

Impedance of potato model under different CFs

The experiment revealed that the contact impedance of various potato models differed under constant CF. An impedance analyzer was utilized to assess the contact impedance of the potato models, and **Figure 8** depicts the differences in contact impedance among the various models under different CFs. Despite the discrepancies observed in the contact impedance among different potato models, an identifiable pattern emerged and was consistent across all the models: an increase in CF corresponded with a decrease in contact impedance.

Discussion

We hypothesized that the CF between the electrode and tissue could potentially influence the effectiveness of IRE treatment. To examine this relationship, experiments were performed on potato models.

To ensure that the experimental outcomes were not influenced by temperature, a thermal imaging camera (323 pro, Fotric Inc., China) was utilized to monitor and record the temperature in real-time during the experiment. The thermal imaging outcomes are depicted in **Figure 9A**. Following the application of pulses, the temperature near the electrode increased maximally to 29.7 °C , which is insufficient to cause cell death. Hence, the impact of temperature on the findings can be disregarded. This finding aligns with previous investigations, indicating that prolonging the biphasic interval beyond 1 ms can drastically reduce thermal damage during the treatment process [30].

To prevent the mechanical damage caused by the CF between the electrode and potato from influencing the tissue, a control group was established. As shown in **Figure 9B**, the control group did not exhibit enzyme-catalyzed browning under varied CF (0.098 N, 0.49 N, 0.98 N, 2.94 N) in the absence of pulse output.

It is important to acknowledge that even though we ensured uniformity in the size and variety of the purchased potatoes, variations in the impedance response among different potato models at the same CF may still exist due to individual differences. The differences in impedance response could be attributed to various factors such as water content, cutting position, or uniformity of measurement position in the potato models. **Figure 8** depicts the variations in impedance among different potato models. Notably, we conducted the impedance detection at a frequency of 400 Hz as the repetition frequency of the output pulse was 400 Hz. Therefore, the output energy was primarily

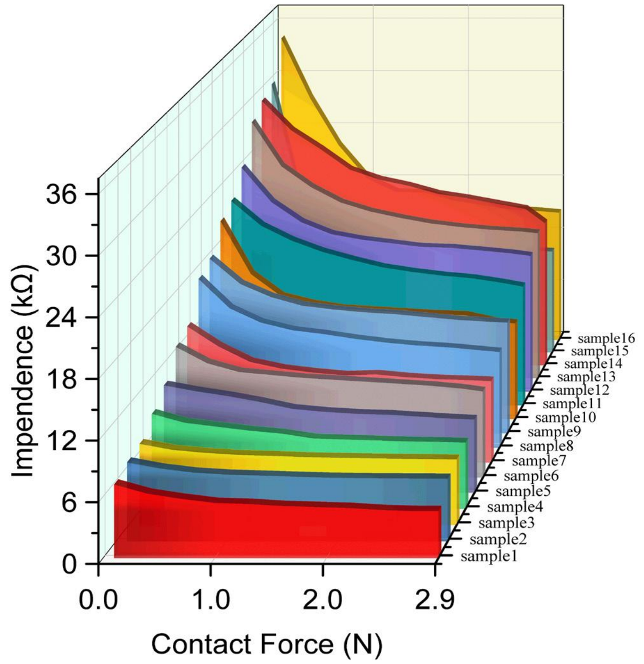

Figure 8. Contact impedance of different potato models under different contact forces.

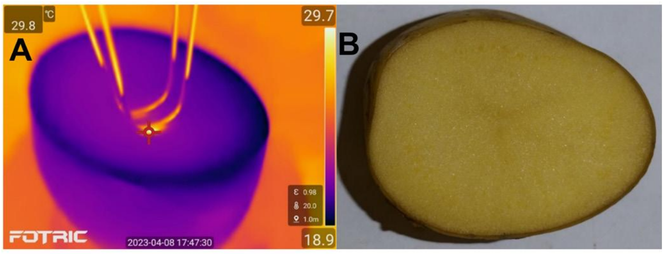

Figure 9. Thermal image and image of the control group. (A) Thermal image recorded during the experiment; (B) Control group with no pulse.

focused on the 400 Hz frequency in the spectrum.

In recent years, the IRE ablation technique has undergone rapid development in both clinical and basic research. The output pulse sequence in IRE has evolved from a monophasic pulse sequence to a biphasic pulse sequence. In current practice, monophasic and biphasic pulse sequences have become the most frequently used types of ablation pulse sequences [31-34]. Our study provides clear evidence that the efficacy of IRE is positively correlated with the CF between the electrode and potato tissue under both biphasic and monophasic output modes. Interestingly, while our results show no significant differences in the correlation for both monophasic and biphasic output modes, **Figure 6A** illustrates that the ablation area under monophasic output mode is greater than that under biphasic output mode at the same CF. The diminished efficacy of IRE ablation under the biphasic output mode could be attributed to the cancellation effect [35]. However, our potato model experiment conducted under current parameters did not reveal a significant difference in the efficacy of IRE ablation at CFs of 0.98 N and 0.49 N. This suggests that the present output electrical parameters may have saturated the IRE effect on the potato model. To mitigate the potential influence of the saturation trend in future experiments, we plan to reduce the pulses to 800 and use the biphasic output mode.

The output pulse amplitude is a critical electrical parameter for IRE, as it determines whether IRE can occur. Research has demonstrated that the electric field threshold for IRE in a potato model is approximately 475 V/cm, using a monophasic pulse sequence [36]. Literature suggests that reducing pulse width or using biphasic pulses results in an increased electric field threshold needed for tissue ablation, compared to monophasic or millisecond pulse width methods [30]. Therefore, in our experiment, we employed three voltage configurations: 350 V, 500 V, and 800 V, corresponding to electric field thresholds of 500 V/cm, 715 V/cm, and 1142 V/cm, respectively.

These voltage configurations are representative of three treatment scenarios in clinical and experimental settings: slightly above the IRE threshold, above the IRE threshold, and above twice the IRE threshold. Our study revealed that, in a fixed output mode (biphasic), the trend of increasing treatment efficacy along with increasing CF remains unchanged when only the output voltage is changed. Notably, we found no significant differences in this correlation across changes in amplitude. This suggests that during treatment, manipulation of the output voltage does not modify the dependence of treatment efficacy on CF.

Changes in the electrode-tissue coupling factor have a significant impact on the contact impedance between the electrode and the tissue. For instance, in a potato model, a loaded contact site will cause elastic deformation of the potato tissue within a specific load range [37, 38]. However, if the load surpasses that range, the potato tissue will undergo plastic deformation [37, 38]. Given that the rigidity of the electrode is substantially higher than that of the potato tissue, when the electrode firmly contacts the potato tissue, the contact area between them will increase due to the elastic deformation of the potato tissue at the point of contact. Consequently, the contact impedance will decrease as the contact area increases. This phenomenon reinforces the need for proper electrode-tissue coupling in electroporation procedures to achieve desired outcomes. As the load is further increased, the cells at the contact point of the potato tissue begin to rupture, and the cellular fluid begins to seep out gradually, leading to a further increase in the contact area between the electrode and the tissue, as well as a subsequent decrease in contact impedance. The direct impact of the decrease in contact impedance is an increase in the output current. As a result, the increase in current leads to an increase in the oxidation area on the surface of the potato model, and results in a positive response of the potato surface oxidation area to the CF.

Overall, in the commonly used output configurations of IRE ablation pulses, there is a positive response of the treatment efficacy to the electrode-potato model CF in IRE.

Limitations

It is important to recognize the limitations of this study, which include the following:

1. The experiment was conducted only on a potato model, which may not accurately reflect the properties of human tissues.

2. The image processing was performed using an algorithm which selects pixels based on the difference between the RGB values of the reference and target regions. Therefore, noise generated during recording the potato oxidation areas may result in missed or erroneous detections. However, all potato models were photographed under the same light source, so this error is considered a systematic error and does not affect the trend analysis of the final data.

3. During the experiment, only the effects of biphasic and monophasic output modes at different output voltages were considered, while other potential factors that might affect the results were ignored, such as interphase interval, pulse frequency, and pulse width. However, although these potential factors can affect the IRE effect, their influence is limited due to the ensured consistency of the parameters across all experiments.

4. The experiment was conducted only on biphasic electrode configurations, so our results only apply to these configurations.

Conclusion

IRE ablation is a promising technology for treating AF because it offers several advantages over traditional catheter surgeries, including reduced thermal damage and reduced nerve damage caused by off-target treatment. Despite these advantages, the widespread clinical adoption of IRE for AF ablation is still hindered by several challenges, such as complex anesthesia protocols and ambiguous treatment outcomes that are influenced by multiple factors. These challenges must be addressed to ensure the efficacy and safety of IRE as a viable alternative to traditional catheter surgeries for AF ablation. The findings of this study indicate that the efficacy of IRE ablation in a potato model is positively correlated with the CF, regardless of whether the output pulse is biphasic or monophasic. Furthermore, our results demonstrate a positive correlation between CF and treatment efficacy under different output voltage amplitudes of a fixed biphasic mode. These observations highlight the importance of optimizing electrode-tissue coupling to achieve optimal outcomes in IRE ablation procedures. Our experimental findings have confirmed the importance of optimizing electrode-tissue coupling and highlight the need to consider the issue of electrode-tissue contact in the design of electrodes for IRE ablation. Poor electrode-tissue contact could lead to insufficient ablation, resulting in postoperative AF, underscoring the significance of improving electrode-tissue coupling for successful IRE ablation procedures. In addition, our experiment highlights the importance of considering the impact of coupling factors when conducting verification experiments on plant models. To further investigate the relationship between CF and treatment efficacy in IRE ablation, our future research will focus on animal models. These studies will provide more insights into the design of advanced IRE ablation protocols and facilitate the clinical promotion and translation of this technology for effective AF treatment.

References

[1] Zoni-Berisso M, Lercari F, Carazza T, et al. Epidemiology of atrial fibrillation: European perspective. Clin Epidemiol 2014;213-220.

[2] Rohrer U, Manninger M, Zirlik A, et al. Impact of Catheter Ablation for Atrial Fibrillation on Quality of Life. J Clin Med 2022;11:4541.

[3] Krijthe BP, Kunst A, Benjamin EJ, et al. Projections on the number of individuals with

atrial fibrillation in the European Union, from 2000 to 2060. Eur Heart J 2013;34:2746-2751.
[4] Andrade J, Khairy P, Dobrev D, et al. The clinical profile and pathophysiology of atrial fibrillation: relationships among clinical features, epidemiology, and mechanisms. Circ Res 2014;114:1453-1468.
[5] Rottner L, Bellmann B, Lin T, et al. Catheter ablation of atrial fibrillation: state of the art and future perspectives. Cardiol Ther 2020;9:45-58.
[6] Mulder BA, Rienstra M, Van Gelder IC, et al. Update on management of atrial fibrillation in heart failure: a focus on ablation. Heart 2022;108:422-428.
[7] Sanchis-Gomar F, Perez-Quilis C, Lippi G, et al. Atrial fibrillation in highly trained endurance athletes—description of a syndrome. Int J Cardiol 2017;226:11-20.
[8] Cappato R, Calkins H, Chen SA, et al. Updated worldwide survey on the methods, efficacy, and safety of catheter ablation for human atrial fibrillation. Circ Arrhythm Electrophysiol 2010;3:32-38.
[9] Pappone C, Oral H, Santinelli V, et al. Atrio-esophageal fistula as a complication of percutaneous transcatheter ablation of atrial fibrillation. Circulation 2004;109:2724-2726.
[10] Sacher F, Monahan KH, Thomas SP, et al. Phrenic nerve injury after atrial fibrillation catheter ablation: characterization and outcome in a multicenter study. J Am Coll Cardiol 2006;47:2498-2503.
[11] Wu TF, Tseng SY, Hung JCJltops. Generation of pulsed electric fields for processing microbes. IEEE Trans Plasma Sci 2004;32:1551-1562.
[12] Martens SL, Klein S, Barnes RA, et al. 600-ns pulsed electric fields affect inactivation and antibiotic susceptibilities of Escherichia coli and Lactobacillus acidophilus. AMB Express 2020;10:1-11.
[13] Wan J, Coventry J, Swiergon P, et al. Advances in innovative processing technologies for microbial inactivation and enhancement of food safety–pulsed electric field and low-temperature plasma. Trends Food Sci. Technol 2009;20:414-424.
[14] Guenther E, Klein N, Zapf S, et al. Prostate cancer treatment with Irreversible Electroporation (IRE): Safety, efficacy and clinical experience in 471 treatments. PLoS One 2019;14:e0215093.
[15] Reddy VY, Koruth J, Jais P, et al. Ablation of atrial fibrillation with pulsed electric fields: an ultra-rapid, tissue-selective modality for cardiac ablation. JACC Clin Electrophysiol 2018;4:987-995.
[16] Varghese F, Philpott JM, Neuber JU, et al. Surgical Ablation of Cardiac Tissue with Nanosecond Pulsed Electric Fields in Swine. Cardiovasc Eng Technol 2023;14:52-59.
[17] Loh P, van Es R, Groen MH, et al. Pulmonary vein isolation with single pulse irreversible electroporation: a first in human study in 10 patients with atrial fibrillation. Circ Arrhythm Electrophysiol 2020;13:e008192.
[18] Sugrue A, Vaidya VR, Livia C, et al. Feasibility of selective cardiac ventricular electroporation. PLoS One 2020;15:e0229214.
[19] Masnok K, Watanabe NJCE, Technology. Relationship of catheter contact angle and contact force with contact area on the surface of heart muscle tissue in cardiac catheter ablation. Cardiovasc Eng Technol 2021;12:407-417.
[20] Han M, Chen L, Aras K, et al. Catheter-integrated soft multilayer electronic arrays for multiplexed sensing and actuation during cardiac surgery. Nat Biomed Eng 2020;4:997-1009.
[21] Howard B, Verma A, Tzou WS, et al. Effects of Electrode-Tissue Proximity on Cardiac Lesion Formation Using Pulsed Field Ablation. Circ Arrhythm Electrophysiol 2022;15:e011110.
[22] Nakagawa H, Castellvi Q, Neal R, et al. B-PO03-131 effects of contact force on lesion size during pulsed field ablation. Heart Rhythm 2021;18:S242-S243.
[23] Soltani Sharif Abadi A, Alinaghi Hosseinabadi P, Hameed A, et al. Fixed-time observer-based controller for the human–robot collaboration with interaction force estimation. Int J Robust Nonlinear Control 2023.
[24] Shimachi S, Hirunyanitiwatna S, Fujiwara Y, et al. Adapter for contact force sensing of the da Vinci® robot. Int J Med Robot 2008;4:121-130.
[25] Abadi ASS, Ordys A, Pierscionek B. Controlling a Teleoperated Robotic Eye Surgical System Under a Communication Channel's Unknown Time Delay. 2023 27th International Conference on Methods and Models in Automation and Robotics (MMAR) 2023;211-215.
[26] Jeong S, Kim H, Park J, et al. Evaluation of electroporated area using 2, 3, 5-triphenyltetrazolium chloride in a potato model. Sci Rep 2021;11:20431.
[27] Lindelauf KH, Thomas A, Baragona M, et al. Plant-based model for the visual evaluation of electroporated area after irreversible electroporation and its comparison to in-vivo animal data. Sci Prog 2023;106:00368504231156294.
[28] Lv Y, Yao C, Rubinsky BJAoBE. A conceivable mechanism responsible for the synergy of high and low voltage irreversible electroporation pulses. Ann Biomed Eng 2019;47:1552-1563.
[29] Suchanek M, Olejniczak Z. Low field MRI study

of the potato cell membrane electroporation by pulsed electric field. J Food Eng 2018;231:54-60.

[30] Aycock KN, Zhao Y, Lorenzo MF, et al. A theoretical argument for extended interpulse delays in therapeutic high-frequency irreversible electroporation treatments. IEEE Trans Biomed Eng 2021;68:1999-2010.

[31] Charpentier KP, Wolf F, Noble L, et al. Irreversible electroporation of the liver and liver hilum in swine. HPB (Oxford) 2011;13:168-173.

[32] Yao C, Dong S, Zhao Y, et al. Bipolar microsecond pulses and insulated needle electrodes for reducing muscle contractions during irreversible electroporation. IEEE Trans Biomed Eng 2017;64:2924-2937.

[33] Sano MB, Arena CB, DeWitt MR, et al. In-vitro bipolar nano-and microsecond electro-pulse bursts for irreversible electroporation therapies. Bioelectrochemistry 2014;100:69-79.

[34] Wandel A, Ben-David E, Ulusoy BS, et al. Optimizing irreversible electroporation ablation with a bipolar electrode. J Vasc Interv Radiol 2016;27:1441-1450. e1442.

[35] Polajžer T, Dermol–Černe J, Reberšek M, et al. Cancellation effect is present in high-frequency reversible and irreversible electroporation. Bioelectrochemistry 2020;132:107442.

[36] Menegazzo I, Mammi S, Sgarbossa P, et al. Time Domain Nuclear Magnetic Resonance (TD-NMR) to evaluate the effect of potato cell membrane electroporation. Innovative Food Sci Emerging Technol 2020;65:102456.

[37] Sun W, Wu JM, Shi LR, et al. Simulation and Experiment of Mechanical Properties of Potato Compression. Adv Mater Res 2013;850–851:1303–1306.

[38] Konstankiewicz K, Zdunek AJIa. Influence of turgor and cell size on the cracking of potato tissue. Int Agrophys 2001;15.

Progress in Medical Devices
eISSN: 2957-5478

Review Article https://doi.org/10.61189/578860ievbid

Progress of near-infrared spectroscopy in cerebral blood oxygenation detection: A mini review

Xinrui Gui, Tingting Shi, Ruoyu Song, Rongguo Yan

School of Health Science and Engineering, University of Shanghai for Science and Technology, Shanghai 200093, China.

Corresponding author: Rongguo Yan.

Declaration of conflict of interest: None.

Received October 19, 2023; Accepted November 28, 2023; Published December 31, 2023

Highlights

- Near-infrared spectroscopy (NIRS) technology transmits a beam of near-infrared light through a transmitter to the brain.
- The changes in hemoglobin concentration and cerebral blood oxygen levels can be estimated using near-infrared light, by comparing the changes in light attenuation over time.
- This paper introduces the basic concept of measuring blood oxygen levels in brain tissue using NIRS technology, and presents the potential applications of the most recent developments in this field of study.

Abstract

In contrast to conventional oximeters, near-infrared spectroscopy-based brain tissue oximetry monitoring devices are capable of non-invasive, continuous, and real-time quantitative monitoring of cerebral oximetry parameters. Initially, these devices were utilized for intensive care or surgical monitoring of oxygen saturation. Due to the rapid advancement of optoelectronic sensing and measurement technologies over the past decade, the derived functional near-infrared brain imaging devices have been widely used in a variety of fields. This paper first introduces the basic principles of near-infrared spectroscopy-based cerebral oxygenation parameter detection, then focuses on the most recent developments in this field of study. Finally, a prospect on their future application in practical settings is also provided.

Keywords: Near-infrared spectroscopy, cerebral oximetry, non-invasive measurement

Introduction

Brain, a very energy-intensive organ, has a much higher oxygen demand and consumption than its oxygen reserves. Even at rest, the brain consumes 25% of the body's total oxygen, making it particularly susceptible to ischemic and hypoxic conditions. Prolonged hypoxia may cause irreversible neurological damage [1]. According to previous literature, the hypoxia-related mortality rate can reach 90% in cases of fatal brain injury [2]. Numerous studies have demonstrated that regional cerebral oxygen saturation (rSO_2) is a valid indicator of severe cerebral hypoxia [3].

These years, patients with brain injuries are clinically diagnosed using cutting-edge imaging technologies like CT, MRI, and positron emission tomography-computed tomography (PET-CT). Yet, devices to accurately monitor blood oxygenation and hemodynamic changes in real time in brain tissue is urgently needed in clinical practice. Near-infrared spectroscopy (NIRS), a novel method for measuring oxygen saturation, enables non-invasive, continuous monitoring of rSO_2 in local brain tissue [4]. This technique can assess the balance of oxygen metabolism in brain tissues as well as early imbalances in blood flow and blood oxygen supply and demand. Through real-time monitoring of changes in the oxygen saturation of specific brain tissues, NIRS can quickly reveal pathological changes in patients with craniocerebral injuries [5]. For surgery, treatment, prognosis, and patient monitoring, this information is in-

Address correspondence to: Rongguo Yan, Department of Biomedical Engineering, School of Health Science and Engineering, University of Shanghai for Science and Technology, No. 516 Jungong Road, Yangpu District, Shanghai 200093, China. E-mail: yanrongguo@usst.edu.cn.

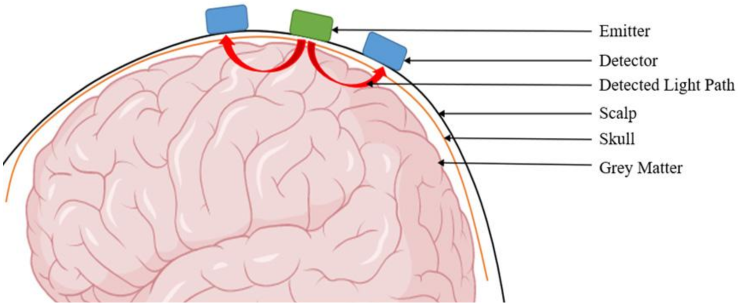

Figure 1. Diagrammatic representation of the light source and photodetectors mounted on the skull's median sagittal cross-section.

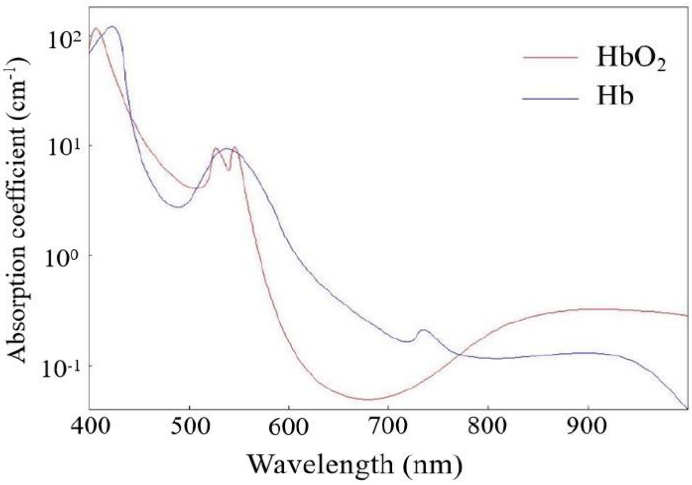

Figure 2. Spectrum of HbO_2 and Hb absorption.

structive. In recent years, NIRS has developed rapidly in fields of biomedical engineering like neonatology, cardiothoracic surgery, and neurosurgery. The goal of this study is to give a general overview of the monitoring principles, the current status of the research, and possible future directions for this technology.

Methods

Lambert-Beer Law

Lambert-Beer's law describes the relationship between incoming and outgoing light, the concentration of the light-absorbing material, and the distance a photon travels. The amount of absorption during photon propagation in a light-absorbing medium depends only on the photon's length and the concentration of the light-absorbing material; it is independent of the intensity of the incident light. During photon transmission, each layer of the light-absorbing medium absorbs photons at the same rate. The formula is OD = ε*C*L, where ε is the coefficient of light extinction, C is the concentration of light-absorbing material, L is the linear separation between the light source and the detector, and OD, optical density, is the amount of light attenuation. It only works when the medium's absorbing substance is constant, and the path taken by the light is straight.

However, due to the fact that the actual path of photons passing through the brain is more complex and there exists other substances absorbing minute amounts of photons, the original law is updated. The modified formula is OD = ε*C*DPF*L+G, which expresses the actual optical path in terms of the product of the distance L and the path-length correction factor DPF (i.e., the path length amplification factor), and G is the total attenuation of the light intensity caused by all other variables aside from oxyhemoglobin (HbO_2) and hemoglobin (Hb).

Principle of NIRS

In the NIRS measurement process, a brain scalp surface positioned light source emits near-infrared light, which is absorbed and scattered as it passes through brain tissue. Two photodetectors are then symmetrically positioned on the scalp near the light source emitter to collect the light scattered in all directions. The entire optical path distribution is shown in **Figure 1**. The human brain's outer tissues are made up of the scalp, skull, cerebrospinal fluid, cerebral gray matter, and cerebral white matter in the order from the outside to the inside, and the near-infrared light has to penetrate all these layers to detect brain tissue effectively [6].

The American Society for Testing and Materials designated the range of 780 nm to 2,526 nm as the near-infrared spectral region after it was found by British astronomer Herschel in 1800 during energy measurements in the infrared portion of the visible region of the solar spectrum. Since first being introduced by Frans Jöbsis in 1977, NIRS has grown into a highly effective and popular technique for optical diagnosis [7]. The technique is based on the optical properties of biological tissues, specifically the ability of near-infrared light to extract biochemical data from the tissues by penetrating skulls and other biological tissues to a particular depth. By observing the series of near-infrared light absorption and scattering processes that take place in biological tissues, this method can be used to estimate the oxygen saturation in brain

Table 1. Absorption coefficient and scattering coefficient of near-infrared light of different wavelength in different tissues (Absorption coefficient/Scattering coefficient, Unit: cm^{-1})

Tissue	690 nm	760 nm	780 nm	830 nm
Scalp	0.159/8.0	0.177/7.3	0.164/7.1	0.191/6.6
Skull	0.101/10.0	0.125/9.3	0.115/9.1	0.136/8.6
Cerebrospinal fluid	0.004/0.1	0.021/0.1	0.017/0.1	0.026/0.1
Gray matter	0.178/12.5	0.198/11.8	0.170/11.6	0.186/11.1

tissue.

The 'spectral window' in tissue optics, in the range of 650-1,000 nm, exhibits notable near-infrared light penetration ability into human tissue. HbO_2 and Hb, which can be distinguished optically due to their different near-infrared absorption coefficients, are the main light absorbers in this region, as shown in **Figure 2**. **Table 1** displays the near-infrared light absorption and scattering characteristics of various tissues. It is possible to choose proper light sources and related detectors referring this table to implement spectral analysis, and the oxygen saturation of brain tissue can be calculated by applying the modified Lambert-Beer law to the measurements of incident and reflected light intensity [8].

NIRS has become a potential method for detecting intracranial injuries as a result of improvements in optical fiber and sensor technology, as well as their integration with computer network technology. This method has important clinical applications because it can be used for noninvasive and real-time monitoring of blood oxygenation parameters in specific localized brain tissues [9].

Functional near-infrared spectroscopy (fNIRS)

The capacity of near-infrared light to reach deeply into biological tissues and the neurovascular coupling mechanism are prerequisites for fNIRS. Functional brain imaging works on the same principle as functional magnetic resonance imaging (fMRI): local hemodynamic changes are caused by neural activity in the brain. It primarily uses the variation in the rates at which Hb and HbO_2 in brain tissue absorb various near-infrared light wavelengths to directly measure the hemodynamic activity of the cerebral cortex in real-time. Such hemodynamic alterations allow for the inverse inference of brain activity.

The primary distinction between NIRS and fNIRS lies in their fields of application and goals. The similarity is that they both use NIRS to measure light absorption, but the difference is the application or focus.

NIRS was first applied to measure physiological parameters like tissue blood flow and oxygen saturation. The medical and biological sciences make extensive use of it, particularly when it comes to blood oxygen level monitoring in the brain and muscle tissues. A specific type of NIRS called fNIRS measures the concentrations of Hb and HbO_2 in the brain to investigate cerebral blood flow, neural activity, and cognitive function. The physiological parameters that NIRS focuses on include blood oxygen saturation, blood flow, and the total Hb concentration in tissues. Understanding changes in tissue oxygen metabolism and hemodynamics can be aided by this. fNIRS is primarily used to measure variations in brain blood oxygen levels brought on by neural activity. It can offer functional details about particular brain areas for research on neurological and cognitive functions.

The benefits of fNIRS include its non-invasiveness, relative portability, and increased tolerance for small head movements. These attributes make fNIRS applicable for young children and infants, as well as individuals with difficulty in remaining motionless when using traditional fMRI equipment. In contrast to fMRI, fNIRS has lower spatial resolution and penetration depth and measures activity primarily at the cortical surface.

fNIRS, which focuses more on the study of brain function, can be considered as a specific application of NIRS overall. Despite the fact that they both employ NIRS techniques, in actuality, they differ slightly due to their areas of focus and application.

Research progress in NIRS

Current Research Status of NIRS

The ability of near infrared to penetrate biological tissues, particularly animal skulls, was first made known by Jöbsis in 1977 [7]. This ground-breaking discovery offered a strong foundation for further research into the dynamics of Hb concentration in the cortex of the human brain. This study pioneered a novel non-invasive measurement of changes in tissue blood oxygenation in addition to confirming the viability of NIRS in monitoring brain activity. Since then, the majority of healthcare professionals have expressed great concern about the interaction of NIRS technology with cerebral blood oxygen monitoring and brain function imaging.

A research team from Hokkaido University in Japan discovered the underlying mechanism of neurovascular coupling in 1994 [10]. They found that neural activity in the brain increases oxygen consumption, which in turn results in increased blood flow in the cerebral white matter. This finding led to the development of useful near-infrared brain imaging tools and the recent emergence of a research hotspot of using NIRS to study neural activity in the brain [11].

From their distinct vantage points, various research groups have offered insights into the use of near-infrared in tissue testing. Their perspectives range from measuring muscle blood oxygenation parameters to monitoring brain activity. Farrel and Binzoni used it to measure the parameters of muscle oxygenation [12]. Esnault compared the cerebral blood oxygenation parameters measured by NIRS with measurements of brain tissue oxygen pressure and came to the conclusion that the two measurements cannot be used interchangeably as a test for people who have suffered craniocerebral trauma [13]. In patients with craniocerebral trauma, Leal-Noval also investigated the relationship between cerebral oxygen parameters and brain tissue oxygen pressure and discovered a weak correlation between these two measurements [14]. Additionally, Esnault's observations were supported by the low accuracy of cerebral oxygen parameter values in detecting moderate cerebral hypoxia.

The high sensitivity of NIRS for monitoring brain oxygenation has been demonstrated in the treatment of cerebrovascular disease. Zweifel's observation using arterial imaging suggested that NIRS could synchronize the detection of decreased cerebral oxygen secondary to vasospasm with high sensitivity [15]. Arterial spasm was significantly correlated with ipsilateral decreases in rSO_2, and as the degree of spasm increased, ipsilateral rSO_2 decreased dramatically. Taussky found a strong correlation between cerebral oxygen saturation and local cerebral blood flow in 1,287 patients using both NIRS and CT perfusion imaging techniques [16]. These suggest the potential of NIRS as a real-time, reliable, non-invasive cerebral oxygen monitoring tool that could be used at the bedside in intensive care units.

Internationally, non-invasive cerebral oximetry monitoring technology has made some early strides, and several companies and academic organizations have already launched their own monitoring programs. China, on the other hand, began its investigation into this topic somewhat later. But in recent years, a number of Chinese institutions, including academic institutions and research facilities, have begun to carry out in-depth investigations on cerebral oximetry monitoring devices using this technology.

In 2005, Prof. Haisu Ding of Tsinghua University successfully developed the TASH-100 non-invasive cerebral oximetry monitoring device, a brain tissue oximetry detector with independent intellectual property rights, and China became the third country after the United States and Japan to do so [17]. Additional Chinese academics and researchers have been inspired by this innovation and stepped up their research on near-infrared cerebral oximetry monitoring. According to trial data from more than 900 clinical cases, the device provides relative and absolute values of brain tissue oxygen saturation and its trend. However, there are still limitations in data sampling frequency and data storage capacity of this device.

Universities like Huazhong University of Science and Technology and Nanjing University of Aeronautics and Astronautics have since conducted studies on cerebral oximetry monitoring devices based on NIRS. While researching near-infrared brain functional imaging, Luo's team at Huazhong University of Science and Technology concentrated on applications like cerebral blood flow momentum detection and brain-computer interface [18]. Using NIRS, they were able to identify the relative alterations in HbO_2 and Hb concentrations separately. The changes in HbO_2 and Hb concentrations responded to stimulation in very different ways, with more increased HbO_2 concentration than Hb concentration. In contrast, as the brain tissue continued to use oxygen, the concentration of Hb increased, while the concentration of HbO_2 decreased. This finding not only adds to previous physiology findings, but also opens up the possibility of further research into the functional processes that lead to the oxygen depletion in brain tissues.

A non-invasive near-infrared cerebral oximetry monitoring system was successfully developed by Qian's research team at Nanjing University of Aeronautics and Astronautics, and its effectiveness was first demonstrated through prospective blocking experiments and oximeter comparison experiments [19]. They discovered that when pressure was applied to the upper

Table 2. Comparison of three near-infrared imaging methods

	CWS	FDS	TRS
Distinction between scattering and absorption	Minimum	Moderate	Maximum
Reference measurement	Relative changes	Absolute changes	Absolute changes
Sampling rate (Hz)	<100	<50	Around 1
Signal-to-noise ratio	Maximum	Moderate	Minimum
Depth resolution	Minimum	Moderate	Maximum
Equipment cost	Both high and low	Relatively high	Relatively high
Equipment volume	Varying sizes	Moderate	Relatively large
Application scenario	Oximetry and Imaging	Oximetry and Imaging	Oximetry

Note: CWS, continuous wave spectroscopy; FDS, frequency domain spectroscopy; TRS, time resolved spectroscopy.

arm, the blood oxygen concentration changed over time. After the value of the blood oxygen concentration was collected and stabilized, it decreased gradually with an instantaneous pressurization to 130 mmHg in 75 seconds. Then, after an instantaneous decompression to 0 after pressurization for 180 seconds, it significantly increased due to the inflow of oxygenated blood and then slowly recovered to its initial value over time. Under a pressurized situation, they found that this device reacted well to changes in the forearm blood oxygen concentration in the upper arm.

NIRS technology has been extensively applied in numerous clinical scenarios, including functional brain imaging, brain tumor imaging, cerebral blood flow detection, and cerebral hematoma detection [20-23]. Currently, the three imaging techniques that are most commonly used by mainstream NIRS cerebral oximetry monitoring devices are continuous wave spectroscopy (CWS), frequency domain spectroscopy, and time resolved spectroscopy detection techniques [24]. **Table 2** provides a detailed comparison of the performance characteristics of these three near-infrared detection systems.

CWS employs a direct method that compares the difference in light intensity before and after the projection of near-infrared light into the brain tissues in order to calculate and assess the degree of oxygen saturation in the brain [24]. It also incorporates a modified version of the Lambert-Beer law.

Frequency domain spectroscopy is more complex as it involves superimposing high-frequency sinusoids from 50 MHz to 1 GHz on the incident light first [25]. Then, it uses phase-modulation spectroscopy to measure the phase shift and intensity of the light, which allows it to calculate precise blood oxygen parameters.

On the other hand, time resolved spectroscopy uses picosecond ultrashort pulse excitation and sends these pulses into the brain [26]. Then, by measuring the light intensity at various time intervals to compute the time dilation function and obtain the optical parameters of the tissue, the absolute amount of blood oxygen within the brain tissue can be precisely determined.

Compared to the latter two, CWS provides clearer and more accurate information about changes in the relative concentrations of HbO_2 and Hb. This feature makes it an excellent choice for continuous monitoring scenarios, particularly when equipment cost is an issue. Therefore, both in commercial product design and in research settings, continuous wave measurements are currently the most popular technique for measuring cerebral oximetry [24].

NIRS has a wide range of intricate applications in biomedical engineering and medical testing, particularly in the non-invasive monitoring and evaluation of blood oxygen levels in the brain and other biological tissues. In addition to providing new insights into fundamental biological processes, this technology encourages innovation in medical diagnostics and therapeutics.

Factors affecting NIRS

The importance of NIRS in clinical diagnosis and treatment is gradually increasing as its application in a variety of fields deepens. However, due to a dearth of prospective studies and high-caliber scientific evidence, the technology still needs to be improved, given its status as a relatively new method of monitoring.

NIRS is affected by a variety of factors in real-world applications, such as extracerebral blood flow, cerebrospinal fluid, skull thickness, and myelin sheaths. The fact that individual differences in rSO_2 measurements might result from the light-absorbing qualities of skin pigments was further supported by a retrospective study by Sun using a large number of samples [27]. Individual variations in rSO_2 measurements might be caused by light-absorbing properties, as shown by lower rSO_2 values for deeper pigmentation and higher rSO_2 values for

Table 3. Type and number of light sources and detectors

References	Light source type	Wavelength number	Wavelength /nm	Number of light sources /pcs	Detector type	Number of detectors /pcs	Number of channels /pcs	Light source - Detector distance /mm
Cheng [29]	LED	Dual- Wavelength	735/850	4	PD	12	30	26
Francis [30]	LED	Dual- Wavelength	740/850	1	SiPD	4	4	5/10/23/28
Maira [31]	LED	Dual- Wavelength	700/830	12	SiPM	13	156	20
Yaqub [28]	LED	Dual- Wavelength	735/850	128	SiPD	1	128	5/20/25/30/35
Tsukasa [32]	LED	Dual- Wavelength	730/855	2	SiAPD	2	4	30
Danial [33]	LED	Octa- Wavelength	750-900	1	PD	4	4	36/42
Wathen [34]	LD	Dual- Wavelength	690/852	32	SiPM	32	32	13

Note: LED, light emitting diode; LD, laser diode; PD, photo diode; SiPD, silicon photo diode; SiPM, silicon photo multiplier; SiAPD, silicon avalanche diode.

Table 4. Technical comparison of NIRS and fMRI, EEG, MEG, PET

	NIRS	fMRI	EEG	MEG	PET
Measurement method	Indirect	Indirect	Direct	Direct	Indirect
Measured signal	Hemodynamic response	Hemodynamic response	Scalp potential	Brain magnetic field	Cerebral metabolism
Spatial resolution	~1 cm	≥0.5 mm voxel	5~9 cm	~1 cm	3~4 mm
Penetration depth	Cerebral cortex	Whole head	Cerebral cortex	Deep structure	Whole head
Sampling rate	≤25 Hz	≤3 Hz	＞1,000 Hz	＞1,000 Hz	＜0.1 Hz
Subject population	No limit	Have limits	No limit	Have limits	Have limits
Outdoor condition	Suitable	Unsuitable	Suitable	Unsuitable	Unsuitable
Wearability	Suitable	Unsuitable	Suitable	Unsuitable	Unsuitable
Long-term detection	Suitable	Unsuitable	Suitable	Unsuitable	Unsuitable
Cost	Low	High	Low	High	High

Note: NIRS, near-infrared spectroscopy; fMRI, functional magnetic resonance imaging; EEG, electrical encephalogram; MEG, magnetoencephalography; PET, positron emission tomography.

lighter pigmentation. Although rSO_2 has made significant progress in the neonatal population, its use in adults has been somewhat constrained by adults' relatively thicker skulls and more pronounced attenuation of near-infrared light.

In addition to the aforementioned variables, different NIRS devices have different detector modules with varying degrees of sensitivity. **Table 3** lists different light sources and detectors that have been used in various NIRS systems over the last few years. Among them, Yaqub created a cutting-edge system with a 12-bit successive-approximation analog-to-digital converter and used a silicon photodiode set up in the photoconductive mode to achieve a high sampling rate when processing significant amounts of NIRS data [28]. Additionally, a filter circuit was specifically included in this design to efficiently reduce high-frequency noise brought on by the high-voltage power supply. In conclusion, choosing the right photodetectors not only significantly improves the detection sensitivity of NIRS system, but also improves the overall performance of the system. This establishes a strong foundation for the use and advancement of NIRS technology.

Future outlook for NIRS

Even after over 20 years of research, NIRS still has some problems in diagnosing and treating patients with craniocerebral injuries. The relationship between rSO_2 and other crucial markers of brain function, such as intracranial pressure, cerebral perfusion pressure, internal jugular venous oxygen saturation ($SjvO_2$), and partial pressure of oxygen in brain tissue ($PbtO_2$), should be further explored in future studies. Through the combined use of transcranial Doppler ultrasound, evoked potentials, and other multimodal monitoring techniques, a comprehensive assessment of the cerebral blood oxygen metabolism and other conditions can be realized, providing more thorough and accurate diagnosis and treatment plan for critically ill patients. These comprehensive analyses will help to accurately define the rSO_2 threshold at the onset of craniocerebral injury.

Clinical staff can more intuitively evaluate the balance of cerebral blood flow and cerebral oxygen supply and demand thanks to real-time rSO_2 monitoring by NIRS. Although this technology has been widely used in Europe and the United States in some clinical areas (such as cerebral oximetry monitoring in cardiothoracic surgery), its potential in clinical settings remains significant. Despite having numerous applications, it is important to note that there is limited data to support the use of NIRS for clinical decision-making and intervention. More clinical trials are therefore required in the future, particularly to assess the application of NIRS in hemorrhage screening in patients with craniocerebral injuries. Verifying whether the advantages of NIRS technology actually translate into better clinical outcomes and facilitating further optimization of medical decision-making and therapeutic approaches should be part of the main research objectives.

Conclusion

Even though modern NIRS is not yet a stand-alone diagnostic tool, it has clear benefits when used in conjunction with noninvasive, portable, and reasonably priced imaging methods like CT. Especially in the field of cranial brain injury detection, the importance of NIRS is unquestionable.

In functional brain imaging, NIRS has different advantages and limitations compared with other techniques, such as fMRI, electrical encephalogram, magnetoencephalography, and PET, and their technological comparisons are shown in **Table 4**. For example, NIRS outperforms fMRI in temporal resolution, outperforms electrical encephalogram in spatial resolution, and, more importantly, is portable and less disturbed by artifacts.

More patients are anticipated to benefit from NIRS as it improves. The technique is not only being utilized more frequently in the rehabilitation of patients with traumatic brain injuries, but also allows for continuous and noninvasive tracking of changes in the parameters governing cerebral blood oxygenation. NIRS data can be a potent addition to existing monitoring measures, providing more thorough information on cerebral pathology, even though there are still certain technical restrictions. The comprehensive performance of NIRS is anticipated to be considerably enhanced with the further development in detection methods and systems, which implies that it is anticipated to be employed for quick screening of casualties in combat or field settings, freeing up crucial time for treatment.

References

[1] Bennett SR, Smith N, Bennett MR. Cerebral oximetry in adult cardiac surgery to reduce the incidence of neurological impairment and hospital length-of-stay: A prospective, randomized, controlled trial. J Intensive Care Soc 2022;23:109-116.

[2] Watson X, Thomas T, Puntis M. Traumatic brain injury: initial resuscitation and transfer. Anaesth Intensive Care 2020;21:282-284.

[3] Stocker RA. Intensive care in traumatic brain injury including multi-modal monitoring and neuroprotection. Med Sci (Basel) 2019;7:37.

[4] Zhong WT. Research on cerebral blood oxygen monitoring method based on NIRS and preliminary implementation of the system. Chongqin University 2021.

[5] Ma XL. Clinical study on perioperative application of local cerebral oxygen saturation monitoring in patients with high risk of stroke. Wannan Medical College 2022.

[6] Kümmel T, van Marwick B, Rittel M, et al. Rapid brain structure and tumour margin detection on whole frozen tissue sections by fast multiphotometric mid-infrared scanning. Sci Rep 2021;11:13.

[7] Jöbsis FF. Noninvasive, infrared monitoring of cerebral and myocardial oxygen sufficiency and circulatory parameters. Science 1977;198:1264-1267.

[8] Barud M, Dabrowski W, Siwicka-Gieroba D, et al. Usefulness of cerebral oximetry in TBI by NIRS. J Clin Med 2021;10:9.

[9] Yuksen C, Sricharoen P, Puengsamran N, et al. Diagnostic properties of a portable near-infrared spectroscopy to detect intracranial hematoma in traumatic brain injury patients. Eur J Radiol Open 2020;7:4.

[10] Okada F, Tokumitsu Y, Hoshi Y, et al. Impaired interhemispheric integration in brain oxygenation and hemodynamics in schizophrenia. Eur Arch Psychiatry Clin Neurosci 1994;244:17-25.

[11] Wang H, Mu XY, Yang J, et al. Brain imaging with near-infrared fluorophores. Coord Chem Rev 2019;380:550-571.

[12] Binzoni T, Spinelli L. Near-infrared photons: a non-invasive probe for studying bone blood flow regulation in humans. J Physiol Anthropol 2015;34:6.

[13] Esnault P, Boret H, Montcriol A, et al. Assessment of cerebral oxygenation in neurocritical care patients: comparison of a new four wavelengths forehead regional saturation in oxygen sensor (EQUANOX®) with brain tissue oxygenation. A prospective observational study. Minerva Anestesiol 2015;81:876-884.

[14] Leal-Noval SR, Cayuela A, Arellano-Orden V, et al. Invasive and noninvasive assessment of cerebral oxygenation in patients with severe traumatic brain injury. Intensive Care Med 2010;36:1309-1317.

[15] Zweifel C, Castellani G, Czosnyka M, et al. Noninvasive Monitoring of Cerebrovascular Reactivity with Near Infrared Spectroscopy in Head-Injured Patients. J Neurotrauma 2010;27:1951-1958.

[16] Taussky P, O'Neal B, Daugherty WP, et al. Validation of frontal near-infrared spectroscopy as noninvasive bedside monitoring for regional cerebral blood flow in brain-injured patients. Neurosurg Focus 2012;32:6.

[17] Ding HS, Teng YC. Non-invasively monitoring human tissue oxygenation using near infrared spectroscopy: independent innovations. Adv Laser OptoElectron 2007;44;14-31.

[18] Zheng Y, Luo QM, Liu Q, et al. A portable instrument for brain activity detection based on near-infrared spectroscopy. Chin J Biomed Eng 2007;898-902.

[19] Liu YK, Li WT, Qian ZY, et al. STM32-based cerebral oxygenation monitoring system using near-infrared spectroscopy. J Data Acquisi Process 2013;28(5):691-696.

[20] Yuan J, Zheng Z, Cao Y, et al. Low-frequency magnetic stimulation of shenmen acupoint reduces blood oxygen levels in the prefrontal cortex of healthy subjects: a near-infrared brain functional imaging study. Chin J Integr Med 2021;27:1-4.

[21] Jordan JT, Gerstner ER. Imaging of Brain Tumors. Continuum (Minneap Minn) 2023;29(1):171-193.

[22] Wu KC, Martin A, Renna M, et al. Enhancing diffuse correlation spectroscopy pulsatile cerebral blood flow signal with near-infrared spectroscopy photoplethysmography. Neurophotonics 2023;10:035008-035008.

[23] Li YY, Luo HJ, Fan XY, et al. Open craniocerebral hematoma imaging based on near-infrared spectroscopy. Laser Phys Lett 2022;19: 045601.

[24] Eleveld N, Esquivel-Franco DC, Drost G, et al. The influence of extracerebral tissue on continuous wave near-infrared spectroscopy in adults: a systematic review of in vivo studies. J Clin Med 2023;12:2776.

[25] Sergio F, Angelo S. Frequency-domain techniques for cerebral and functional near-infrared spectroscopy. Front Neurosci 2020;14:300.

[26] Aleh S, Stanislaw W, Frédéric L, et al. Depth-resolved assessment of changes in concentration of chromophores using time-resolved near-infrared spectroscopy: estimation of cytochrome-c-oxidase uncertainty by monte carol simulations. Biomed Opt Express 2019;10:4621-4635.

[27] Sun X, Ellis J, Corso PJ, et al. Skin pigmentation interferes with the clinical measurement of regional cerebral oxygen saturation. Br J Anaesth 2015;114:276-280.

[28] Yaqub MA, Woo SW, Hong KS. Compact, portable, high-density functional near-infrared spectroscopy system for brain imaging. IEEE Access 2020;8:128224-128238.

[29] Chen C, Ma Z, Liu Z, et al. An Energy-efficient wearable functional near-infrared spectroscopy system employing dual-level adaptive sampling technique. IEEE Trans Biomed Circuits Syst 2022;16:119-128.

[30] Tsow F, Kumar A, Hosseini SH, et al. A low-cost, wearable, do-it-yourself functional near-infrared spectroscopy (DIY-fNIRS) headband. HardwareX 2021;10:e00204.

[31] Maira G, Chiarelli AM, Brafa S, et al. Imaging system based on silicon photomultipliers and light emitting diodes for functional near-infrared spectroscopy. Appl Sci 2020;10:1068.

[32] Tsukasa F, Takashi N, Hiroki S, et al. Rearrangeable and exchangeable optical module with system-on-chip for wearable functional near-infrared spectroscopy system. Neurophotonics 2017;5:011007.

[33] Chitnis D, Airantzis D, Highton D, et al. Towards a wearable near infrared spectroscopic probe for monitoring concentrations of multiple chromophores in biological tissue in vivo. Rev Sci Instrum 2016;87:065112.

[34] Wathen J, Fitch M, Pagán V, et al. A 32-channel frequency-domain fNIRS system based on silicon photomultiplier receivers. Proceedings of SPIE (11629): Optical Techniques in Neurosurgery, Neurophotonics, and Optogenetics. SPIE BiOS 2021;116291P.